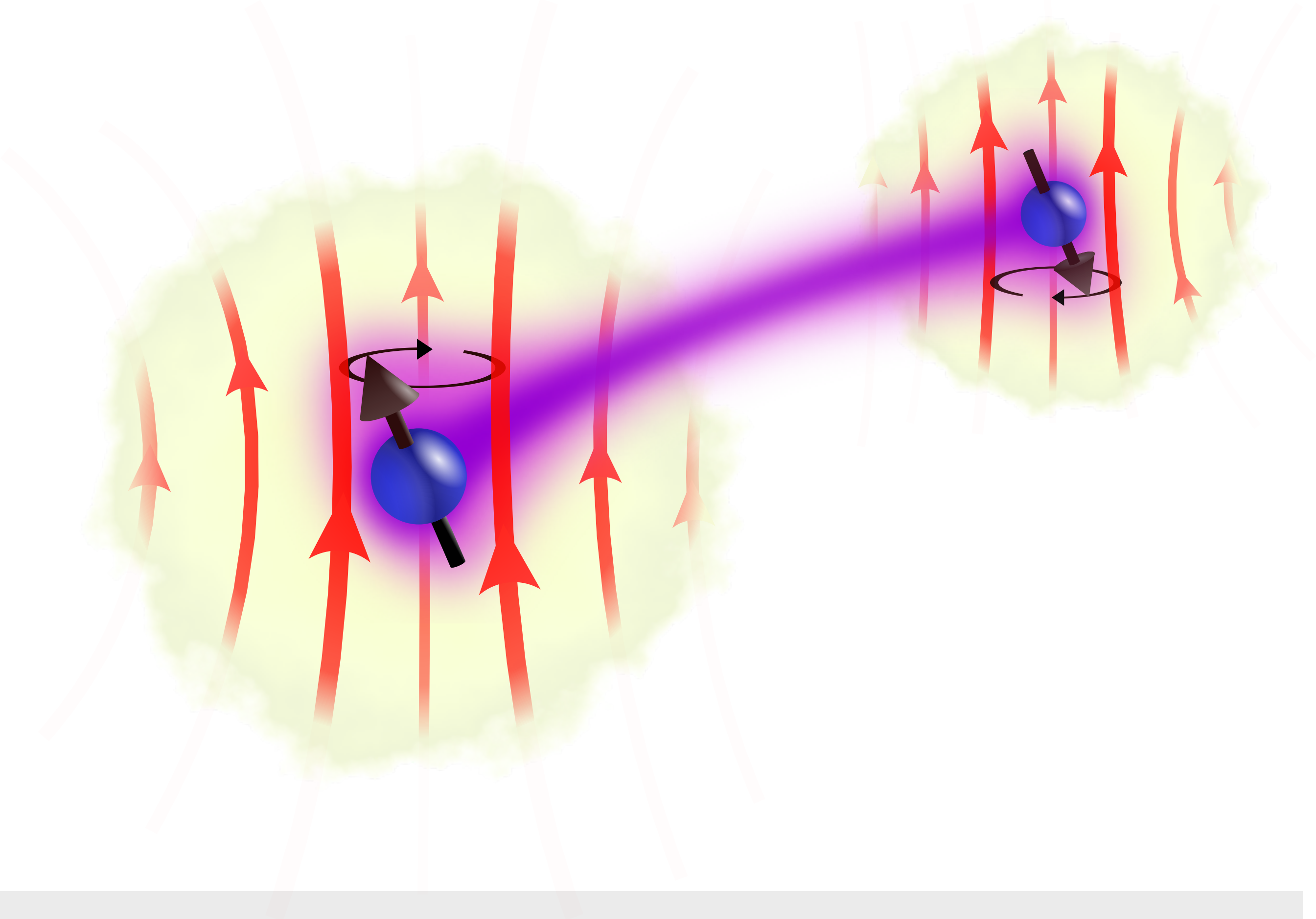

Entanglement-based magnetometry in a scalable ion-trap quantum processor

Thomas Ruster
geboren in Mainz

Dissertation

zur Erlangung des Grades

Doktor der Naturwissenschaften

am Fachbereich Physik, Mathematik und Informatik
der Johannes Gutenberg-Universität in Mainz

Mainz, den 13.12.2017

Zusammenfassung

Die „zweite Quantenrevolution“ hat begonnen: Neue Technologien, die auf grundlegenden Prinzipien der Quantenmechanik basieren, stehen kurz vor dem kommerziellen Einsatz. Vor allem das Phänomen der Verschränkung ermöglicht neuartige Quantensensoren und Quantencomputer. Experimente mit Ionenfallen nehmen eine Vorreiterrolle bei der Entwicklung von Quantentechnologien ein, da in ihnen einzelne Teilchen gezielt manipuliert und miteinander verschränkt werden können.

Grundlage der Experimente dieser Arbeit ist eine segmentierte lineare Paulfalle, in der Kalzium-Ionen gespeichert und als Quantenbits genutzt werden. Laser werden eingesetzt, um Einzelqubit- und Verschränkungsoperationen auszuführen. Zur Realisierung eines skalierbaren Quantencomputers können aus Ionen bestehende Ketten innerhalb der segmentierten Paulfalle bewegt und rekonfiguriert werden.

Eine Basisoperation zur beliebigen Rekonfiguration von Ionenketten ist das Trennen eines Zwei-Ionen-Kristalls in zwei einzelne Ionen. In dieser Arbeit wird gezeigt, wie dieser Prozess innerhalb von 80 µs mit einer mittleren Anregung des Bewegungszustandes von lediglich $\overline{n} = 4.16(0.16)$ Phononen pro Ion gelingt. Die dafür entscheidenden Kontrollparameter und Kalibrationsverfahren werden im Detail vorgestellt.

In einem Quantencomputer muss die Qubit-Kohärenzzeit die Dauer von Gatteroperationen und Ionentransporten deutlich überschreiten. Bei dem in dieser Arbeit verwendeten $^{40}\mathrm{Ca}^{+}$-Spin-Qubit sind zeitliche Fluktuationen des Magnetfeldes der bei weitem dominante Grund für Dekohärenz. Deshalb ist der Ionenfallen-Aufbau von einer Magnetfeldabschirmung umgeben, und Spulen zur Erzeugung eines Quantisierungsfeldes wurden durch $\mathrm{Sm_2Co_{17}}$-Permanentmagnete ersetzt. Diese Maßnahmen haben die zeitliche Variation des Magnetfeldes erheblich reduziert, sodass eine $1/\sqrt{\mathrm{e}}$ Ramsey-Kohärenzzeit von 370(40) ms und eine Spin-Echo-Kohärenzzeit von 2.12(7) s erreicht wurde. Das ist deutlich länger als die typische Dauer von $10-80$ µs für verschränkende Quantengatter.

Da Ionen im Laufe eines Quantenalgorithmus innerhalb der Paulfalle bewegt werden, muss die räumliche Variation des Magnetfeldes ebenfalls berücksichtigt werden. Daher wurde ein neuartiges Messverfahren für inhomogene DC-Magnetfelder entwickelt, das eine bisher unerreichte Kombination aus räumlicher Auflösung und Sensitivität ermöglicht. Hierfür werden zwei verschränkte Ionen an verschiedene Positionen innerhalb der Ionenfalle transportiert. Die durch den Zeeman-Effekt aufgesammelte Phase φ eines Bellzustandes $\left(|\uparrow\downarrow\rangle + \mathrm{e}^{\mathrm{i}\varphi}\,|\downarrow\uparrow\rangle\right)/\sqrt{2}$ erlaubt es, Magnetfelddifferenzen ΔB zwischen den Ionenpositionen zu bestimmen, während zeitliche Fluktuationen auf beiden Ionen durch die antiparallele Spinausrichtung unterdrückt werden. Magnetfelddifferenzen wurden über eine maximale Distanz von 6.2 mm, mit einer Präzision von bis zu 310 fT und einer Sensitivität von bis zu $S = \Delta B_{\mathrm{err}}\sqrt{T_{\mathrm{meas}}} = 12\ \mathrm{pT}/\sqrt{\mathrm{Hz}}$ gemessen. Die räumliche Auflösung des Verfahrens beträgt etwa 20 nm. Ein Bayesscher Algorithmus zur Frequenzbestimmung sorgt für einen maximalen Informationsgewinn pro Messung bei gleichzeitig hohem Dynamikbereich.

Abstract

The "second quantum revolution" is coming: New fields of research, such as quantum computing and quantum metrology, are aiming at commercial applications harnessing the fundamental principles of quantum mechanics. Ion-trap experiments are at the frontier of this research because they not only enable outstanding control over single particles, but also allow for creating multi-particle entanglement.

The experiments presented in this work rely on a segmented linear Paul trap, where calcium ions are stored and employed as quantum bits. Lasers are used to carry out operations on individual qubits and to entangle multiple ions. To realize a scalable quantum computer, chains of ions can be moved and rearranged within the segmented Paul trap.

A key operation for rearranging ion chains is to separate two-ion crystals into single ions. This process is demonstrated with a minimum mean excitation of $\overline{n} = 4.16(0.16)$ vibrational quanta per ion at a duration of 80 µs. The most important control parameters and calibration procedures are presented in detail.

In a quantum computer, the qubit coherence time must significantly surpass the duration of gate and shuttling operations. For the $^{40}\mathrm{Ca}^+$ spin qubit employed in this thesis, temporal fluctuations of the magnetic field are the main reason for decoherence. The ion-trap apparatus is therefore enclosed in a μ-metal magnetic shield, and coils for generating the quantizing magnetic field have been replaced by $\mathrm{Sm_2Co_{17}}$ permanent magnets. These measures have substantially reduced magnetic-field fluctuations, leading to a $1/\sqrt{\mathrm{e}}$ Ramsey coherence time of 370(40) ms and a spin-echo coherence time of 2.12(7) s. This is considerably longer than the typical duration of entangling gates in the $10 - 80$ µs range.

Since ions are shuttled to different locations in the course of a quantum algorithm, the spatial variation of the magnetic field has to be taken into account as well. For this purpose, a novel measurement scheme for inhomogeneous DC magnetic fields has been developed, which operates in a previously inaccessible parameter regime in terms of spatial resolution and sensitivity. Entangled Bell states of the type $\left(|\uparrow\downarrow\rangle + \mathrm{e}^{\mathrm{i}\varphi}\,|\downarrow\uparrow\rangle\right)/\sqrt{2}$, encoded in two ions stored at different locations, are used as *sensor states*. The linear Zeeman effect imprints a relative phase φ, which serves for measuring the magnetic-field difference ΔB between the constituent locations. Temporal magnetic-field fluctuations on both ions are rejected because of the anti-parallel spin alignment of the sensor state. Measurements of magnetic-field differences have been carried out over distances of up to 6.2 mm, with accuracies down to 310 fT, and sensitivities down to $S = \Delta B_{\mathrm{err}}\sqrt{T_{\mathrm{meas}}} = 12\ \mathrm{pT}/\sqrt{\mathrm{Hz}}$. The sensing scheme features spatial resolutions of about 20 nm. A Bayesian algorithm for frequency estimation optimizes the information gain of the magnetic-field measurements while maintaining a high dynamic range.

Contents

1 Introduction

Quantum mechanics is the fundamental theory for understanding nature at small scales. After the field had emerged in the first half of the 20th century, a variety of devices that rely on quantum theory have been invented. These include lasers, semiconductors, and atomic clocks. Often referred to as belonging to *the first quantum revolution*, these devices depend on quantum effects that involve ensembles of particles. Especially the invention of the transistor and its miniaturization initiated the *digital revolution* and has thus dramatically influenced our day-to-day life.

1.1. The rise of information technology

Since the invention of integrated circuits in the 1950s, an entire industry has evolved from the efforts to squeeze as many transistors as possible into silicon-based microchips. Over the years, these chips have become increasingly powerful while at the same time shrinking in size and consuming less power. Gordon Moore, co-founder of Intel, predicted in 1975 that the number of components per integrated circuit would double every two years [Moo65, Moo75]. This prediction, known as *Moore's law*, has been quickly accepted as a goal for the semiconductor industry, and has proved true for over 40 years. A growing industry and mass production of increasingly powerful microchips have led to the development of electronic devices such as personal computers, digital cameras, and highly capable mobile phones. The interconnection of these devices to global networks has revolutionized our everyday life by enabling fast worldwide information transfer.

Today's commonly available microchips consist of billions of transistors, while only being as big as a coin. As industry is working hard to shrink transistors even further, the technical challenges to overcome are becoming more and more difficult. Consequently, progress has slowed down in recent years. The time between new generations of chips has increased, and the cost per transistor has stagnated [Mar15].

One of the main challenges is fabrication. Microchips are made of *wavers*, thin slices of crystalline silicon, which undergo various processing steps. One of these steps is *photolithography*, where UV light and chemical treatment is used to transfer a geometric pattern from a photomask to the waver. Today's most advanced microchips feature structures in the few-nanometer regime - well below the wavelength of typical UV light sources. In order to fabricate structures significantly below this wavelength, a variety of sophisticated techniques are being used, such as *multi-patterning*, where multiple separate exposure steps are carried out to improve resolution. Already since 1988, there is an ongoing work to develop lithography techniques using extreme ultraviolet (EUV) radiation at a wavelength of 13.5 nm [Kem06, Wag10]. However, due to a vast amount of technical issues and tremendous cost, manufacturers have not yet used EUV lithography for commercial products.

Fabrication is not the only challenge to be overcome. As structure size approaches the regime of only a few molecules, additional quantum mechanical effects become relevant. Already today, nanoscale transistors have to be carefully designed to avoid quantum tunneling and energy quantization effects [Wan06]. To further continue miniaturization, alternative materials and transistor geometries are being investigated [Xia06, Bjö07]. But rather than suppressing these quantum effects, the question arises whether it is feasible to design electronics that *take advantage* of them. It has turned out that not only new types of transistors [Sea10], but entirely new devices and technologies can be created based on the concepts of quantum mechanics.

1.2. Towards quantum technologies

In the course of the first quantum revolution, quantum physics has mainly been utilized to understand and modify the behavior of large-scale devices. Driven by ongoing theoretical work and recent technological advances, new fields of research have emerged to bring fundamental quantum principles into practical applications. This is referred to as the *second quantum revolution.* These new research fields include quantum metrology, quantum communication, quantum information and quantum simulation.

A key topic of this work is quantum information processing, which aims at extending classical information technology by carrying out calculations with quantum systems [Fey86]. For this purpose, bits, the basic units of information in computing, are replaced by quantum bits, or *qubits.* While a bit is represented as either 0 or 1, the state of a qubit is described by a wave function, given by a linear combination of the basis states $|0\rangle$ and $|1\rangle$:

$$|\Psi\rangle_1 = a\,|0\rangle + b\,|1\rangle \tag{1.1}$$

This is known as the superposition principle: A qubit can simultaneously exist in *both* $|0\rangle$ and $|1\rangle$. For multiple qubits, the state is also described by a single wave function, but the number of available basis states grows exponentially with the number of qubits. For example, the wave function for two qubits is

$$|\Psi\rangle_2 = c\,|00\rangle + d\,|01\rangle + e\,|10\rangle + f\,|11\rangle\,. \tag{1.2}$$

The stored information in the wave function is described by complex coefficients a, b or, respectively, c, d, e, f. These take into account that quantum systems can exhibit interference effects, just like classical waves.

The most striking consequence of the superposition principle is *entanglement.* For certain choices of the coefficients in Eq. 1.2, the qubits no longer behave as individual particles. For instance, the wave function $\left(|00\rangle + |11\rangle\right)/\sqrt{2}$ describes two qubits in the same state, but the state of each individual qubit is completely undetermined - they are entangled. Entanglement is a genuine quantum-mechanical effect and plays a key role in many applications of quantum information, such as teleportation [Bou97]. In the process of teleportation, a quantum state can be transmitted over arbitrary distances if an entangled state is shared between two locations.

In analogy to logic gates in conventional computers, *quantum gates* are basic operations that modify the wave function of one or multiple qubits. If multiple input states are encoded in a wave function, quantum gates act on all these states at once. This phenomenon, also called *quantum parallelism*, enables quantum computers to solve problems that are believed to be intractable on classical computers.

One of the most famous quantum algorithms that makes use quantum parallelism is Shor's algorithm [Sho97]. It solves the problem to find the prime factors of a given integer number substantially faster than the most efficient known classical algorithm. Shor's algorithm has drawn incredible attention towards the field of quantum information, because its implementation on a large-scale quantum computer would allow breaking common cryptography schemes that secure internet data transfer today. Other promising uses of quantum computers include database search [Gro97], image processing [Yao17], and machine learning [Cai15].

While the theoretical concept of quantum computing has been existing for more than two decades, the practical realization of a large-scale quantum computer still represents a formidable challenge. Even though quantum computers rely on quantum bits, the coefficients of the wave function are in fact *analog* numbers. Operations on the quantum bits therefore have to be performed with high accuracy. Additionally, the wave function of a quantum system in general loses its phase information in the presence of ambient noise, it experiences *decoherence*. It is therefore important to isolate qubits as much as possible from the environment in order to preserve the quantum state, while at the same time retaining the ability to perform gate operations.

Once operations on quantum bits reach a certain level of quality, *quantum error correction* [Ter15] allows for further protecting quantum states from errors such as decoherence. Quantum error correction is fundamentally different from error-correction schemes in classical computers, where information can be copied and stored multiple times. Quantum states, however, cannot be copied due to the no-cloning theorem [Woo82]. The key to quantum error correction is entanglement: By storing the information of one *logical qubit* in an entangled state of multiple physical qubits, certain errors can be detected and corrected without affecting the information stored in the logical qubit.

Many different architectures for realizing quantum computers are currently under investigation. These include superconducting qubits, color centers in diamond crystals, trapped ions, photons, and many others (a detailed overview is given by Ladd et al. [Lad10]). As each approach features distinct advantages and disadvantages, a scientific consensus on a preferred architecture has not yet been established. Following the proposal by Cirac and Zoller [Cir95], this work focuses on *Paul traps* in combination with laser-ion interactions to realize a platform suitable for quantum information processing.

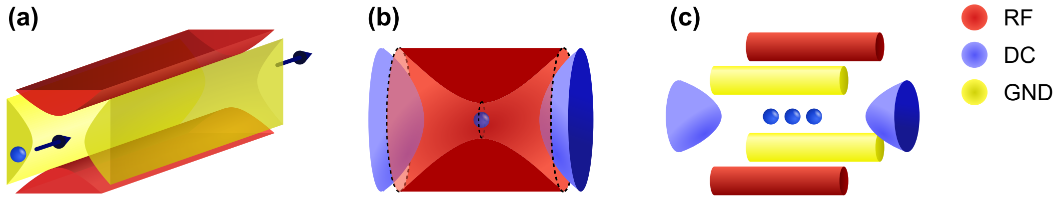

Figure 1.1.: Evolution of Paul traps: **(a)** Initial proposal of the quadrupole mass filter, in which ions within a certain mass range are confined in two dimensions. Arrows indicate the direction of travel for confined ions. **(b)** A combination of static (DC) and oscillating electric fields in the radio-frequency regime (RF) is used to achieve a three-dimensional confinement. Hyperbolical electrodes resemble a quadrupolar field configuration, but limit optical access. **(c)** The linear Paul trap enables improved optical access and alignment of ions in a linear crystal.

1.3. Quantum information processing in Paul traps

A Paul trap is an ion trap that combines static and alternating electric fields in order to confine charged particles within a small region in space, and therefore isolates them from the environment. The basic idea of Paul traps is that charged particles experience *ponderomotive forces* in rapidly oscillating electric fields, i.e., they are accelerated by a time-averaged force towards the weak-field direction. Since these ponderomotive forces depend on the mass-to-charge ratio of the particle, the underlying concept has been initially conceived and employed as mass spectrometers [Pau53].

Depending on the application, a wide range of electrode geometries have been designed and used in experiments (Fig. 1.1). Initial designs featured hyperbolic-shaped electrodes that resemble an electric quadrupole field (Fig. 1.1(a),(b)). Since then, simpler electrode designs have been adopted that facilitate optical access to the trapped ions. Linear Paul traps (Fig. 1.1(c)) in particular feature excellent optical access and the ability to arrange ions in linear crystals along the axial symmetry axis, and are therefore commonly used today. Even for simple electrode geometries, the electric field near the center of the trap closely resembles a quadrupolar configuration.

Laser cooling ensures that trapped ions always reside close to the trap center. Lasers are also an ideal tool to initialize, manipulate, and read-out the internal electronic state of ions. Thus, qubits can be represented by two (meta)stable energy levels of an atomic species that are accessible via laser interactions. Quantum gates on single qubits are implemented by tightly focusing laser beams onto individual ions in a multi-ion crystal. In order to realize gates acting on a set of qubits, the Coulomb interaction between the ions is utilized: The motion of the ions is described by coupled harmonic oscillators, and lasers can be used to transfer quantum information from individual qubits to the collective vibrational modes of the ion crystal and vice versa. A more detailed theoretical description of how trapped ions are affected and controlled by external fields is given in chapter 2 of this thesis, and the operation principle of qubits encoded in $^{40}\mathrm{Ca}^+$ is discussed in chapter 3.

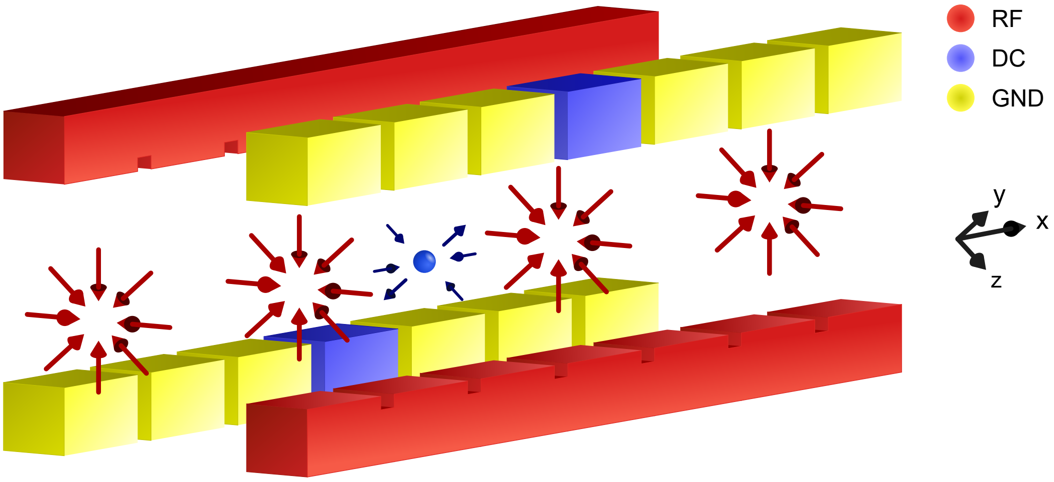

Figure 1.2.: The segmented linear Paul trap: The DC electrodes are separated into multiple segments, controllable by individual voltages. Red arrows indicate the time-averaged force field on a charged particle due to the applied RF voltage, and blue arrows indicate the force caused by DC voltages on the two blue-colored electrodes. The combined force of the DC and RF electrodes confines charged particles in three dimensions.

By applying these principles in linear Paul traps, small-scale quantum computers have already been realized in the laboratory: Deterministic entanglement of up to 14 ions [Mon11b] and algorithms on a few qubits such as the quantum fourier transform [Sch13, Deb16] and a scalable Shor algorithm [Mon16] have been demonstrated. However, adding more and more qubits to a single ion trap is infeasible: The typical inter-ion distances of a few micrometers are more and more reduced, and eventually shrink below the diffraction limit of the laser beams. Furthermore, the number of vibrational modes of an ion crystal increases, leading to spectral crowding in frequency space.

1.4. Segmented linear Paul traps

In 2002, Kielpinski, Monroe, and Wineland proposed a *quantum charge-coupled device* architecture to achieve scalability with trapped ions [Kie02]. This device consists of an array of interconnected ion traps, in which only a few ions are contained each. Ions can be shuttled between these traps by applying time-dependent voltages to the electrodes. This architecture is experimentally realized with *segmented* linear traps. In this work, a segmented trap similar to Fig. 1.2 is used, wherein ions are shuttled along the axial (x) direction of the trap. Lasers are focused to a specific *laser interaction zone*, and ions are moved back and forth between this laser interaction zone and numerous storage segments. Addressing of specific ions with laser beams is technically less demanding than in a single linear Paul trap, since the inter-ion distance can be increased to hundreds of micrometers or even millimeters. By employing multiple potential wells with only a limited number of ions each, the number of vibrational modes per ion crystal is also

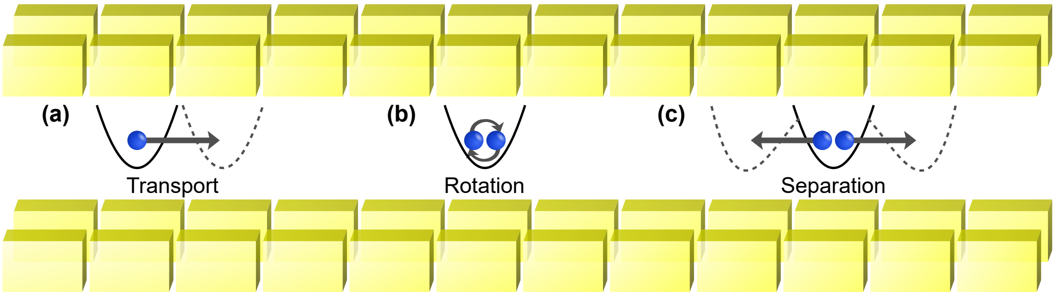

Figure 1.3.: Three basic operations for arbitrary ion movement and reconfiguration. In **(a)**, a harmonic potential well is moved in order to transport ions along the trap axis. In **(b)**, a two-ion crystal is rotated, effectively swapping the ion positions. In **(c)**, a harmonic potential is transformed into a double-well potential to separate a two-ion crystal.

reduced, and parallel operation is facilitated by the ability to set up multiple laser interaction zones.

However, the usage of segmented traps gives rise to a number of additional technological challenges. More electrodes have to be fabricated on a smaller scale, requiring small-scale fabrication methods such as laser-cutting or photolithography [Kau17a, Sch09]. Compared to conventional linear traps, the ion-electrode distance is typically smaller in segmented traps and thus enhances the effect of electrical noise on the ions, leading to excitation of the motional state [Bro15]. Hence, the experiments presented in this thesis have been carried out in a microfabricated segmented trap that had been optimized towards low electrical noise [Kau17a], and the trap electrodes are supplied by a low-noise multi-channel voltage generator. Chapter 4 gives a more detailed overview over the experimental apparatus.

The implementation of ion movement and ion-chain reconfiguration also represents a major experimental challenge. These tasks are tackled by combining three basic operations: Transport, separation, and rotation (Fig. 1.3). Each operation contributes to the run-time required by quantum algorithms, and excites the motional state of ions. Excitation of the motional state is generally undesired, as quantum gates on multiple qubits require the motion to be cooled close to the ground state [Lee05, Lei03b]. Consequently, an implementation of these processes is needed that executes them as fast as possible, while keeping motional excitation at a minimum. Ion transport and ion-crystal rotation have already been realized on a timescale comparable to gate operation, at negligible energy increase [Bow12, Wal12b, Kau17b].

This thesis focuses on the experimental implementation of ion-crystal separation, following the guidelines presented by Kaufmann et al. [Kau14]. During the separation process, the common potential well at the initial electrode is lifted, while two separate wells are created at the two neighboring electrodes. Separation represents a major experimental challenge, because it shows a strong sensitivity to imperfect control settings. The underlying reason is that a *critical point* is transiently reached, where the harmonic confinement vanishes. This makes the ions susceptible to energy increase mechanisms. First experimental realizations thus showed large amounts of excess energy transfer [Row02]. Since then, experimental techniques have been improved and fast separation of a two-ion crystal that maintains a low energy increase at a duration as low as 55 µs has been reported [Bow12].

Reliable optimization procedures are needed to prevent the separation operation from posing a major limitation. In chapter 5, a universal procedure for optimizing the important parameters controlling the process is presented. The separation procedure can be controlled by three parameters: a static potential tilt, a voltage offset at the critical point, and the total duration of the process. Measurements of ion distances, trap frequencies, and the final motional excitation are used to optimize these control parameters.

By combining single and two-qubit gates, ion transport, and separation of ion crystals, small-scale quantum information experiments on multiple qubits have already been demonstrated. These include deterministic quantum teleportation [Bar04], entanglement purification [Rei06], a programmable two-qubit processor [Han10], and scalable creation of long-lived multipartite entanglement [Kau17c].

1.5. Trapped-ion qubit coherence times

A crucial prerequisite for carrying out increasingly complex quantum algorithms is a sufficiently slow decay of qubit coherence. This decay is characterized by the *coherence time*, the timescale during which the relative phase φ of a quantum superposition is well defined. Over a duration T, a superposition of two states $|0\rangle$ and $|1\rangle$ accumulates a relative phase that depends on their energy difference ΔE:

$$|\Psi\rangle = \left(|0\rangle + \mathrm{e}^{\mathrm{i}\varphi}\,|1\rangle\right)/\sqrt{2} \quad , \qquad \varphi = \frac{\Delta E}{\hbar} T. \tag{1.3}$$

Due to the Zeeman effect, the energy levels of widely employed qubits based e.g. on $^{40}\mathrm{Ca}^{+}$ or $^{88}\mathrm{Sr}^{+}$ are linearly dependent on the ambient magnetic field. Thus, magnetic-field fluctuations lead to phase fluctuations, and therefore decoherence. As a result, high stability of the magnetic field is a crucial requirement for long coherence times. Moreover, it has been shown that entangled states may exhibit an increased sensitivity to magnetic-field fluctuations, scaling with the squared number of constituent qubits in the worst case [Mon11b]. Various technical measures such as μ-metal shielding, active magnetic-field stabilization, synchronization to the AC mains and improved current drivers for supply of coils for generation of a quantizing magnetic field lead to typical coherence times of 10-40 ms [Haz11, Sch13].

By contrast, ion species with hyperfine structure such as $^{9}\mathrm{Be}^{+}$ [Bol85], $^{43}\mathrm{Ca}^{+}$ [Ben08, Har14] or $^{171}\mathrm{Yb}^{+}$ [Olm07, Tim11] allow for encoding quantum information in magnetic-field-insensitive transitions that feature a vanishing first-order Zeeman shift. Utilizing these species can, however, lead to additional challenges: A more complex level structure can lead to increased sophistication of qubit operation. Furthermore, such transitions require operation at a specific *magic* magnetic field, which can restrict the range of possible applications. Some species require large magnetic fields, yielding Zeeman splittings larger than the natural linewidths of cycling or repump transitions. This in turn leads to increased complexity of e.g. Doppler cooling, qubit-state preparation, and readout. Moreover, some hyperfine species require laser fields at wavelengths in the UV range, which are less convenient to generate and manipulate. While all these challenges have been successfully addressed, operating hyperfine qubits still leads to a resource overhead and increased complexity.

A second option for avoiding magnetic-field-induced decoherence is to employ qubits that are encoded in *decoherence-free subspaces* of several physical qubits. For example, entangled Bell states of the type $\left(|01\rangle \pm |10\rangle\right)/\sqrt{2}$ can be used as basis states for a single qubit, but are encoded in two physical qubits. Under ideal conditions, the energy of both states $|01\rangle$ and $|10\rangle$ is identical, and the accumulated phase is hence unaffected by energy fluctuations in both states. By using this effect, persisting coherence at wait times of more than 20 s has been demonstrated [Kie01, Roo04, Häf05, Lan05], but the number of required ions is doubled, as well as the complexity of computational gates [Mon09, Iva10].

Another technique for prolonging qubit coherence is *dynamical decoupling* [Bie09, Bie11, Bar13], where phase fluctuations are averaged out by the application of laser pulses. For example, a π laser pulse on the quantum state in Eq. 1.3 transforms $|0\rangle$ to $|1\rangle$ and vice versa, and thus reverses the sign of ΔE and the accumulated phase. By applying suitable pulse sequences, the accumulated phase can be effectively controlled in order to cancel undesired fluctuations. However, this comes at the cost of increased control overhead, particularly for scalable architectures.

In this work, long qubit coherence times are attained via suppression of ambient magnetic-field fluctuations. A μ-metal magnetic-shielding enclosure is combined with Sm_2Co_{17} permanent magnets for magnetic-field generation. A detailed characterization of the qubit coherence is presented in chapter 6.

1.6. Quantum magnetometers

The outstanding control of the internal and motional state of trapped ions is not only applicable to quantum computers, but also to a wider range of quantum devices. This work aims at adopting techniques initially developed in the context of quantum information for high-precision magnetometry.

Magnetic-field sensors are ubiquitous in modern technology and applied and fundamental research. Depending on the desired application, various sensing technologies are available, covering different parameter regimes in terms of sensitivity, spatial resolution, bandwidth, and other parameters.

The sensitivity of a sensor is often described by the minimum detectable magnetic field within a given data acquisition time:

$$S := B_{\mathrm{err}}\sqrt{T_{\mathrm{tot}}}, \tag{1.4}$$

with the standard error of a magnetic field measurement B_{err} that has been achieved during a total experimental time of T_{tot} [Tay08]. This definition implies that a lower

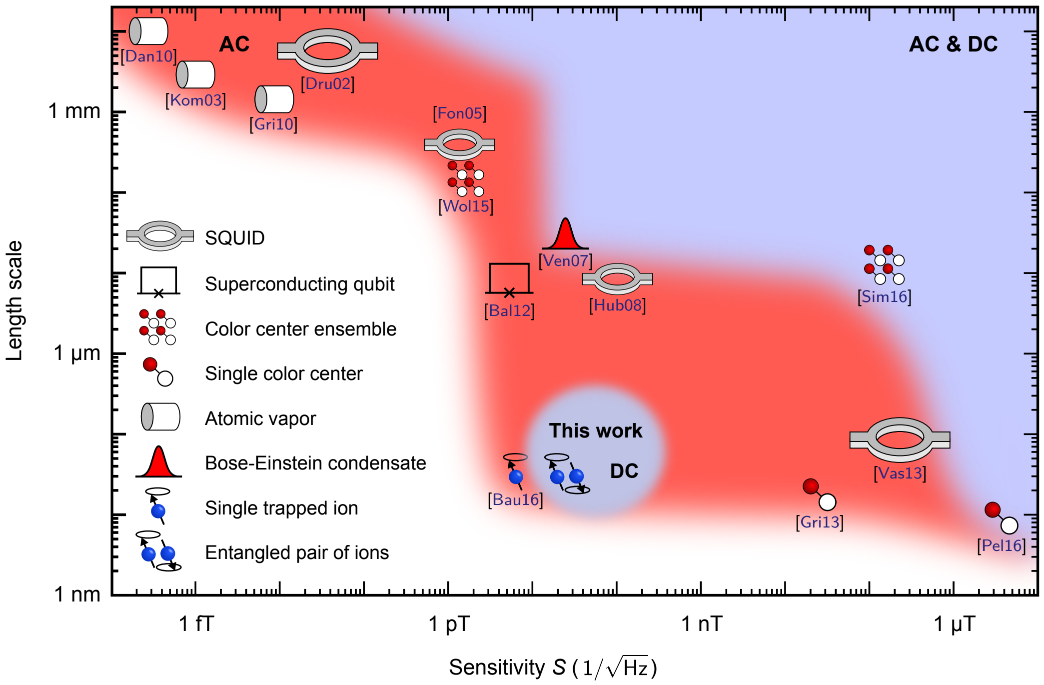

Figure 1.4.: Overview of recently developed magnetic-field sensors in a size-sensitivity diagram. A lower value of the sensitivity S corresponds to a better sensor performance, and a smaller length scale corresponds to a better spatial resolution. The red-shaded area represents the accessible regime for alternating (AC) fields, while the blue-shaded area depicts the accessible regime for both quasistatic < 1 Hz (DC) and alternating fields. This work substantially extends the regime for DC sensing.

value corresponds to a better sensor performance. The normalization factor $\sqrt{T_{\text{tot}}}$ takes into account that measurement errors typically scale as $1/\sqrt{T_{\text{tot}}}$.

Among the most widespread magnetic-field sensors are *Hall probes* and *fluxgate sensors*. While these are easy to use, better sensitivities are achieved with *superconducting quantum-interferometer devices* (SQUIDs) at cryogenic temperatures [Jak64]. SQUIDs exist in various dimensions, ranging from a few mm to the tens of nm regime.

In the last decade, SQUIDs have been increasingly challenged by *atomic magnetometers*, in which the dependence of atomic energy levels on magnetic fields is utilized. The energy difference between two atomic states can be determined with high accuracy by creating a superposition and measuring the accumulated phase during an interrogation time T. Contrary to quantum computation experiments, a strong coupling to magnetic fields is *desired* in magnetic-field sensors.

Typically, the choice of a sensing platform requires trading sensitivity versus spatial resolution (Fig. 1.4). SQUIDs measure the magnetic flux inside a superconducting loop, given by the magnetic field integrated over the surface area of the loop. Thus, larger SQUIDs typically offer a better sensitivity for magnetic fields. Atomic magnetometers are based on either single well-isolated atoms, or ensembles of atoms. Ensembles are more accurate than a single particle, but also have larger dimensions.

Suitable ensemble systems include atomic vapors [Bud07], ultracold atomic gases [Kos11], and color centers in diamonds [Ron14]. Atomic vapors offer record sensitivities below the 1 $\mathrm{fT}/\sqrt{\mathrm{Hz}}$ level, but have typical dimensions above 1 mm^3. By contrast, single vacancy centers [Ang15, Bal08, Gri13, Pel16] have been used for high-resolution imaging of magnetic fields in the nm regime. Single trapped ions are also well-suited for magnetic-field imaging [War13], with spatial resolutions of about 20 nm.

A key parameter of atomic magnetometers is the interrogation time T. For longer interrogation times, less experimental cycles can be performed within a given data acquisition time, but more phase is accumulated during each cycle. In total, this leads to an improved sensitivity, scaling as $1/\sqrt{T}$. However, magnetometers do not only measure the desired signal, but also undesired noise sources such as fluctuations in the geomagnetic field and the fields emanated by nearby electrical devices. This leads to decoherence during the interrogation time and reduces the attainable sensitivity.

Quantum entanglement can be harnessed to extend sensing capabilities [Roo06, Und16]. Entangled Greenberger-Horne-Zeilinger states of the type $\left(|00\ldots0\rangle + \mathrm{e}^{\mathrm{i}\varphi}\,|11\ldots1\rangle\right)/\sqrt{2}$ or N00N states of the type $\left(|N0\rangle + \mathrm{e}^{\mathrm{i}\varphi}\,|0N\rangle\right)/\sqrt{2}$ offer enhanced sensitivities [Hue97, Lei04, Jon09], but also suffer from increased noise-induced decoherence [Mon11b]. Thus, it is crucial to find sensing schemes that reject noise while still being sensitive to the desired signal.

A well-established method for achieving long coherence times is dynamical decoupling, where the desired signal is spectrally separated from noise. However, this technique is restricted to measurements of alternating (AC) magnetic fields. Recently, dynamical decoupling with a single trapped ion has been used to demonstrate magnetometry in the radio-frequency range, attaining a few-$\mathrm{pT}/\sqrt{\mathrm{Hz}}$ level of sensitivity [Bau16, Kot11]. A second option for canceling undesired noise sources are gradiometers, where two identical sensors are used to measure differential magnetic fields while rejecting common-mode fluctuations [She17, Gra09, Bla15].

Entangled states can also be tailored to reject noise in favor of the desired signal. With trapped ions, decoherence-free subspace qubits of the type $\left(|{\uparrow\downarrow}\rangle + \mathrm{e}^{\mathrm{i}\varphi}\,|{\downarrow\uparrow}\rangle\right)/\sqrt{2}$ have been employed as *sensor states* to measure local magnetic-field gradients [Roo04, Lan05] as well as the magnetic dipole interaction between the constituents' valence electrons [Kot14].

In chapter 7 of this thesis, a magnetic gradiometer using these sensor states is presented. The constituent ions are freely moved to different locations x_1 and x_2 along the trap axis of a segmented linear Paul trap, and the DC magnetic-field difference $\Delta B(x_1, x_2)$ between the ion locations is inferred from the phase accumulation rate of the sensor state

$$\Delta\omega(x_1, x_2)_{\mathrm{DC}} \equiv \dot{\varphi}_{\mathrm{DC}} = \frac{g\mu_{\mathrm{B}}}{\hbar}\Delta B(x_1, x_2). \tag{1.5}$$

The long coherence times of the sensor state and the fine-positioning capabilities offered by trapped ions enable magnetic-field sensing in a parameter regime that could previously not be accessed: *DC* field differences are sensed at precisions of around 300 fT and

12 pT$\sqrt{\text{Hz}}$ sensitivity, and the spatial resolution is limited by the size of the ion's ground state wave function of about 13 nm.

The presented sensing scheme is applied to measure the spatial dependence of the magnetic field within the segmented Paul trap. This knowledge is crucial for carrying out quantum algorithms where multiple ions are stored at different trap segments. Any inhomogeneous magnetic field leads to the accumulation of undesired position-dependent phases, which have to be accounted for in computational sequences.

2 Interaction of ions with external fields

The foundation of using trapped ions for quantum technologies is the ability to accurately control them with external fields. Static and off-resonant oscillating magnetic fields shift the energy levels of the trapped particles (Sec. 2.1). Sec. 2.2 summarizes the behavior of the trapped ions' motion in the electric field of the Paul trap, and describes how the motion and the internal electronic state of the ions can be manipulated with lasers. Light-ion interactions are also suitable tool for measuring the motional state (Sec. 2.3).

2.1. Interaction of atoms with magnetic fields

Static magnetic fields

The energy-level shift of trapped ions (or atoms in general) caused by magnetic fields is known as the Zeeman effect. Here, we discuss the interaction of a magnetic moment $\vec{\mu}$ of an atom with a static and homogenous magnetic field $\vec{B} = (0, 0, B)$. The Hamiltonian is given by

$$\hat{H}_0 = -\hat{\vec{\mu}} \cdot \vec{B} \tag{2.1}$$

The magnetic moment can be caused by either electron spins, orbital angular momentum, nuclear spins, or a combination thereof. For trapped $^{40}\mathrm{Ca}^+$ ions, the magnetic moment is given by the valence electron spin $\hat{\vec{S}}$ and, depending on the populated electronic state, an additional orbital angular momentum $\hat{\vec{L}}$. If the interaction $\hat{H}_0$ is small compared to the spin-orbit coupling, the magnetic moment is given by

$$\hat{\vec{\mu}} = -g \frac{e}{2m_e} \hat{\vec{J}} \tag{2.2}$$

with the total angular momentum $\hat{\vec{J}} = \hat{\vec{S}} + \hat{\vec{L}}$, and the Landé factor of the electronic state g. then, the Hamiltonian becomes

$$\hat{H}_0 = g \frac{e}{2m_e} \hat{\vec{J}} \cdot \vec{B} = g \frac{\mu_\mathrm{B}}{\hbar} \hat{J}_z \cdot B \tag{2.3}$$

with the Bohr magneton $\mu_\mathrm{B} = \frac{e\hbar}{2m_e}$. The energy eigenvalues are

$$E_m = g\mu_\mathrm{B} m B = m\hbar\omega_\mathrm{L} \tag{2.4}$$

with the Larmor frequency $\omega_\mathrm{L} = g\mu_\mathrm{B}\frac{B}{\hbar}$ and $m = -j, -j+1, \ldots, j$. The eigenstates are denoted as $|j, m\rangle$. Equation 2.4 shows that static magnetic fields split the magnetic sublevels of an electronic state equidistantly by $\hbar\omega_\mathrm{L}$.

Oscillating magnetic fields: Hamiltonian

If the magnetic sublevels of a given electronic state are split by a static magnetic field, transitions between these levels can be driven by applying an additional oscillating magnetic field $\vec{B}_{\mathrm{rf}} = \left(B_{\mathrm{rf},\perp}\cos(\Omega_{\mathrm{rf}}t), 0, B_{\mathrm{rf},\|}\cos(\Omega_{\mathrm{rf}}t)\right)$. The oscillating field leads to an additional contribution to the Hamiltonian:

$$\hat{H}(t) = \hat{H}_0 + \hat{V}(t) \tag{2.5}$$

$$\hat{V}(t) = 2\Omega_\perp \hat{J}_x \cos(\Omega_{\mathrm{rf}}t) + 2\Omega_\| \hat{J}_z \cos(\Omega_{\mathrm{rf}}t) \tag{2.6}$$

with $\Omega_\perp = \frac{1}{2}g\frac{\mu_{\mathrm{B}}}{\hbar}B_{\mathrm{rf},\perp}$ and $\Omega_\| = \frac{1}{2}g\frac{\mu_{\mathrm{B}}}{\hbar}B_{\mathrm{rf},\|}$. Due to the rotational symmetry of $\hat{H}_0$, it is safe to omit the y-component in the oscillating magnetic field. The z-component in the magnetic field does not contribute to the result. We rather include it to prove that it does not cause a systematic error in the experiment.

For the following calculations, it is beneficial to switch to the interaction picture. The interaction Hamiltonian is transformed as

$$\hat{V}_I(t) = \mathrm{e}^{\mathrm{i}\hat{H}_0 t/\hbar}\hat{V}(t)\mathrm{e}^{-\mathrm{i}\hat{H}_0 t/\hbar} \tag{2.7}$$

$$= 2\Omega_\| \hat{J}_z \cos(\Omega_{\mathrm{rf}}t) + \mathrm{e}^{\mathrm{i}\omega_{\mathrm{L}}t\hat{J}_z/\hbar} 2\Omega_\perp \hat{J}_x \cos(\Omega_{\mathrm{rf}}t)\mathrm{e}^{-\mathrm{i}\omega_{\mathrm{L}}t\hat{J}_z/\hbar}. \tag{2.8}$$

Then, we express $\hat{V}_I(t)$ in terms of the ladder operators $\hat{J}_\pm = \hat{J}_x \pm \mathrm{i}\hat{J}_y$:

$$\hat{V}_I(t) = 2\Omega_\| \hat{J}_z \cos(\Omega_{\mathrm{rf}}t) + \Omega_\perp \cos(\Omega_{\mathrm{rf}}t)\mathrm{e}^{\mathrm{i}\omega_{\mathrm{L}}t\hat{J}_z/\hbar}\left(\hat{J}_+ + \hat{J}_-\right)\mathrm{e}^{-\mathrm{i}\omega_{\mathrm{L}}t\hat{J}_z/\hbar}. \tag{2.9}$$

The relevant states for this thesis are the $S_{1/2}$ state with $j = 1/2$, and the $D_{5/2}$ state with $j = 5/2$. By writing down the matrix elements of $\hat{J}_z$ and $\hat{J}_\pm$ for these states and performing the matrix multiplications, we obtain

$$\hat{V}_I(t) = 2\Omega_\| \hat{J}_z \cos(\Omega_{\mathrm{rf}}t) + \Omega_\perp \cos(\Omega_{\mathrm{rf}}t)\left(\hat{J}_+\mathrm{e}^{\mathrm{i}\omega_{\mathrm{L}}t} + \hat{J}_-\mathrm{e}^{-\mathrm{i}\omega_{\mathrm{L}}t}\right) \tag{2.10}$$

$$= 2\Omega_\| \hat{J}_z \cos(\Omega_{\mathrm{rf}}t) + \frac{1}{2}\Omega_\perp\left[\hat{J}_+\left(\mathrm{e}^{\mathrm{i}(\omega_{\mathrm{L}}+\Omega_{\mathrm{rf}})t} + \mathrm{e}^{\mathrm{i}(\omega_{\mathrm{L}}-\Omega_{\mathrm{rf}})t}\right) + \right. \tag{2.11}$$

$$\left. \hat{J}_-\left(\mathrm{e}^{-\mathrm{i}(\omega_{\mathrm{L}}+\Omega_{\mathrm{rf}})t} + \mathrm{e}^{-\mathrm{i}(\omega_{\mathrm{L}}-\Omega_{\mathrm{rf}})t}\right)\right]. \tag{2.12}$$

By introducing the definitions $\delta = \omega_{\mathrm{L}} - \Omega_{\mathrm{rf}}$ and $\Sigma = \omega_{\mathrm{L}} + \Omega_{\mathrm{rf}}$, the interaction Hamiltonian becomes

$$\hat{V}_I(t) = 2\Omega_\| \hat{J}_z \cos(\Omega_{\mathrm{rf}}t) + \frac{\Omega_\perp}{2}\left[\hat{J}_+\left(\mathrm{e}^{\mathrm{i}\Sigma t} + \mathrm{e}^{\mathrm{i}\delta t}\right) + \hat{J}_-\left(\mathrm{e}^{-\mathrm{i}\Sigma t} + \mathrm{e}^{-\mathrm{i}\delta t}\right)\right]. \tag{2.13}$$

If the radiation is near resonant, i.e. $\delta \approx 0$, this Hamiltonian gives rise to the well-known *Rabi oscillations* between magnetic sublevels. More details about Rabi oscillations are, e.g., described by Budker et al. [Bud08]. The theoretical derivation of Rabi oscillations usually involves the *rotating wave approximation*, where the rapidly oscillating terms $\mathrm{e}^{\mathrm{i}\Sigma t}$ are neglected.

Far off-resonant oscillating magnetic fields

Let us now discuss the case of far off-resonant excitation. In this case, the rotating wave approximation is not valid, and the problem can be instead tackled by solving the time-dependent Schrödinger equation in the interaction picture according to Budker et al. [Bud08]. It is

$$\mathrm{i}\hbar\frac{\mathrm{d}}{\mathrm{d}t}\left|\Psi(t)\right\rangle_I = \hat{V}_I(t)\left|\Psi(t)\right\rangle_I . \tag{2.14}$$

The interaction-picture state can be expressed as a general superposition of Zeeman sublevels of the electronic state:

$$\left|\Psi(t)\right\rangle_I = \sum_{m=-j}^{j} c_m(t)\left|j,m\right\rangle . \tag{2.15}$$

Upon multiplying Eq. 2.14 with $\langle j,n|$, we obtain the set of equations

$$\mathrm{i}\hbar\,\dot{c}_n(t) = \sum_{m=-j}^{j} c_m(t)\left\langle j,n\right|\hat{V}_I(t)\left|j,m\right\rangle , \tag{2.16}$$

where $n=-j,-j+1,\ldots,j$. Since only far off-resonant excitation is considered here, we assume that the populations $|c_n(t)|$ do not change over time. Then, it is beneficial to write

$$c_n(t) \approx c_n(0)\,\mathrm{e}^{-\mathrm{i}\varphi_n(t)}. \tag{2.17}$$

The time derivative is

$$\dot{c}_n(t) = -\mathrm{i}\,c_n(0)\,\dot{\varphi}_n(t)\,\mathrm{e}^{-\mathrm{i}\varphi_n(t)}. \tag{2.18}$$

In the first step, we assume that the accumulated phase is small, i.e. $\mathrm{e}^{-\mathrm{i}\varphi_n(t)} \approx 1$. The phase accumulation rate becomes

$$\dot{\varphi}_n(t) \approx \frac{\mathrm{i}}{c_n(0)}\dot{c}_n(t) = \frac{1}{\hbar c_n(0)}\sum_{m=-j}^{j}\left\langle j,n\right|\hat{V}_I(t)\left|j,m\right\rangle c_m(t) \tag{2.19}$$

where we inserted Eq. 2.16 in the last step. We additionally cast Eq. 2.16 into an integral equation

$$\mathrm{i}\hbar\,c_n(t) = \sum_{m=-j}^{j}\int_0^t c_m(t)\left\langle j,n\right|\hat{V}_I(t')\left|j,m\right\rangle \mathrm{d}t' \;\approx \sum_{m=-j}^{j} c_m(0)\left\langle j,n\right|\int_0^t \hat{V}_I(t')\mathrm{d}t'\left|j,m\right\rangle . \tag{2.20}$$

Then, we insert the integral equation into Eq. 2.19, and the phase accumulation rate becomes

$$\begin{aligned}\dot{\varphi}_n(t) &\approx \frac{1}{\mathrm{i}\hbar^2 c_n(0)}\sum_{m=-j}^{j}\sum_{k=-j}^{j} c_k(0)\left\langle j,n\right|\hat{V}_I(t)\left|j,m\right\rangle\left\langle j,m\right|\int_0^t \hat{V}_I(t')\mathrm{d}t'\left|j,k\right\rangle \\ &= \frac{1}{\mathrm{i}\hbar^2 c_n(0)}\sum_{k=-j}^{j} c_k(0)\left\langle j,n\right|\hat{V}_I(t)\int_0^t \hat{V}_I(t')\mathrm{d}t'\left|j,k\right\rangle\end{aligned} \tag{2.21}$$

Then, we consider the product

$$
\begin{aligned}
V_I(t)\int_0^t \hat{V}_I(t')\mathrm{d}t' = &\left(2\Omega_\parallel \hat{J}_z\cos(\Omega_\mathrm{rf}t) + \tfrac{\Omega_\perp}{2}\hat{J}_+\left(\mathrm{e}^{\mathrm{i}\Sigma t}+\mathrm{e}^{\mathrm{i}\delta t}\right) + \tfrac{\Omega_\perp}{2}\hat{J}_-\left(\mathrm{e}^{-\mathrm{i}\Sigma t}+\mathrm{e}^{-\mathrm{i}\delta t}\right)\right) \times \\
\times &\left(\tfrac{2\Omega_\parallel}{\Omega_\mathrm{rf}}\hat{J}_z\sin(\Omega_\mathrm{rf}t) + \tfrac{\Omega_\perp}{2}\hat{J}_+\left(\tfrac{\mathrm{e}^{\mathrm{i}\Sigma t}-1}{\mathrm{i}\Sigma}+\tfrac{\mathrm{e}^{\mathrm{i}\delta t}-1}{\mathrm{i}\delta}\right) + \tfrac{\Omega_\perp}{2}\hat{J}_-\left(\tfrac{\mathrm{e}^{-\mathrm{i}\Sigma t}-1}{-\mathrm{i}\Sigma}+\tfrac{\mathrm{e}^{-\mathrm{i}\delta t}-1}{-\mathrm{i}\delta}\right)\right).
\end{aligned}
\tag{2.22}
$$

After time averaging, the only relevant terms are

$$\left\langle V_I(t)\int_0^t \hat{V}_I(t')\mathrm{d}t'\right\rangle = -\mathrm{i}\frac{\Omega_\perp^2}{4}\left(\hat{J}_-\hat{J}_+ - \hat{J}_+\hat{J}_-\right)\left(\frac{1}{\Sigma}+\frac{1}{\delta}\right) \tag{2.23}$$

Due to the commutator relation $\left[\hat{J}_+,\hat{J}_-\right] = 2\hbar\hat{J}_z$, this simplifies to

$$\left\langle V_I(t)\int_0^t \hat{V}_I(t')\mathrm{d}t'\right\rangle = \mathrm{i}\hbar\frac{\Omega_\perp^2}{2}\hat{J}_z\left(\frac{1}{\Sigma}+\frac{1}{\delta}\right). \tag{2.24}$$

Plugging this result into Eq. 2.21, the sum collapses and we obtain the time-averaged phase accumulation rate for each Zeeman sublevel n:

$$\langle\dot{\varphi}_n\rangle = \frac{\Omega_\perp^2}{2}n\left(\frac{1}{\Sigma}+\frac{1}{\delta}\right) = n\Omega_\perp^2\frac{\omega_\mathrm{L}}{\omega_\mathrm{L}^2-\Omega_\mathrm{rf}^2}. \tag{2.25}$$

This phase accumulation rate is equivalent to an additional energy shift, the *AC Zeeman shift*. If two magnetic sublevels m_1 and m_2 are populated, the differential phase accumulation rate is

$$\omega^{(\mathrm{ac},1)} := \langle\dot{\varphi}_{m_1}\rangle - \langle\dot{\varphi}_{m_2}\rangle = \Delta m\left(g\frac{\mu_\mathrm{B}}{2\hbar}B_{\mathrm{rf},\perp}\right)^2\frac{\omega_\mathrm{L}}{\omega_\mathrm{L}^2-\Omega_\mathrm{rf}^2} \tag{2.26}$$

with $\Delta m = m_1 - m_2$. Since the phase is linearly accumulating with time, the assumption $\mathrm{e}^{-\mathrm{i}\varphi_n(t)} \approx 1$ does not hold for large evolution times. In order to obtain a more accurate result, we solve the differential equation 2.16 again, but with the revised assumption $\mathrm{e}^{-\mathrm{i}\varphi_n(t)} = \mathrm{e}^{-\mathrm{i}\omega^{(\mathrm{ac})}t}$. This leads to a similar expression:

$$\omega^{(\mathrm{ac})} = \Delta m\left(g\frac{\mu_\mathrm{B}}{2\hbar}B_{\mathrm{rf},\perp}\right)^2\frac{\nu}{\nu^2-\Omega_\mathrm{rf}^2}, \tag{2.27}$$

where the Larmor frequency ω_L is replaced by the total absolute (angular) frequency splitting between neighboring magnetic sublevels

$$\nu := \omega_\mathrm{L} + \omega^{(\mathrm{ac})}. \tag{2.28}$$

This quantity does not only make the result more accurate, but is also easier accessed in the experiment.

The only relevant oscillating magnetic field in this experiment is caused by the RF electrodes of the ion trap. The field imposes a tiny correction to the energy splitting of the trapped calcium ions: The ground state spin levels are split by approximately $2\pi \cdot 10$ MHz, and the contribution from the AC Zeeman effect on the order of $2\pi \cdot 10$ Hz is negligible for most experiments. Nevertheless, it has to be accounted for in the high-precision magnetic-field sensing scheme presented in chapter 7.

2.2. Light-atom interactions with trapped ions

Lasers are not only a crucial tool for initializing, manipulating, and reading out the internal electronic state of ions, but also for manipulating their motion. This chapter outlines the theoretical description of the interaction between lasers and trapped ions, following the approaches in James [Jam98], Leibfried et al. [Lei03a], and Poschinger [Pos10]. A more thorough description can be found in these sources.

The motional state of a single trapped ion is, to a good approximation, described by a three-dimensional harmonic oscillator. For an exact solution, the rapidly oscillating RF trapping field has to be taken into account, which leads to additional *micromotion* at the frequency of the oscillating field. For the experiments presented in this thesis, micromotion does not play a crucial role, and is therefore not discussed here. The main effects are an increased linewidth during Doppler cooling, and a reduction of Rabi frequencies for coherent laser interactions. The effects of micromotion are discussed in greater detail by Cirac et al. [Cir94]. A thorough explanation on the confining mechanism of Paul traps is, e.g., given by Paul [Pau90] and Poschinger [Pos10].

If multiple ions are trapped in a single harmonic potential, they form *ion crystals* in which each ion oscillates around its equilibrium position. The oscillations of N ions are described by N collective normal modes in each direction, and the equilibrium positions are usually separated by a few micrometers.

We approximate the internal electronic structure of the ions by a two-level system with levels $|g\rangle$ and $|e\rangle$. This approximation is justified if the interacting laser is close to the resonant frequency of two internal levels of the ion. Thus, the energy eigenstates of a single trapped ion are

$$|\Psi\rangle = |g,e\rangle\,|n_x\rangle\,|n_y\rangle\,|n_z\rangle \tag{2.29}$$

with $n_{x,y,z}$ the quantum numbers characterizing the respective harmonic oscillator states along the x, y, z direction. The quantum number $n_{x,y,z}$ is also commonly called *phonon number*, because the collective motion of ion crystals behaves similarly to vibrations in solid state systems.

The experiments in this thesis utilize three types of laser-ion interactions: Electric dipole-allowed transitions, electric quadrupole-allowed transitions, and stimulated Raman transitions. Electric dipole-allowed transitions exhibit a strong coupling to lasers and are, e.g., used for Doppler cooling and state detection, where a large number of scattered photons is beneficial. Electric quadrupole-allowed transitions feature small linewidths and long decay times, and thus are suitable for coherent operations.

Stimulated Raman transitions [Mon95] are two-photon transitions, and thus require two laser beams with a well-defined phase relation, usually from a common laser source. A third energy level is used as an intermediate step for the two-photon transition. The optical frequency of both beams must be close to this third level, but sufficiently detuned to avoid population transfer. The detuning is usually in the range of 10 GHz to a few THz. Similar to electric quadrupole-allowed transitions, stimulated Raman transitions allow for driving coherent operations between two levels $|g\rangle$ and $|e\rangle$.

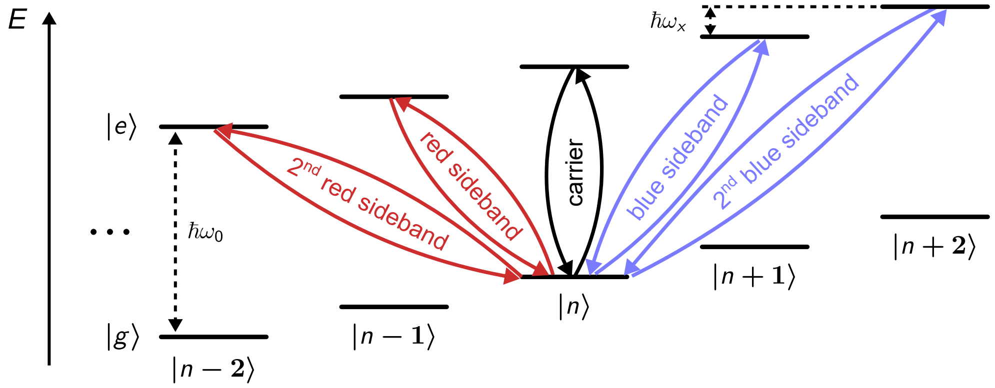

Figure 2.1.: Energy levels of a single trapped ion, and allowed transitions for an ion initialized to $|g\rangle\,|n\rangle$.

Electric dipole-allowed transitions, electric quadrupole-allowed transitions, and stimulated Raman transitions can be described by an effective Rabi frequency Ω, an effective light frequency ω, and an effective wave vector $\vec{k}$ in a unified framework. For stimulated Raman transitions, the effective wave vector and light frequency are given by the respective differences of both laser beams. Assuming running plane wave light fields, the interaction is described by a coupling Hamiltonian

$$\hat{H} = \frac{\hbar}{2}\Omega\left(|g\rangle\langle e| + |e\rangle\langle g|\right)\left(e^{i(\vec{k}\hat{\vec{x}}-\omega t)} + e^{-i(\vec{k}\hat{\vec{x}}-\omega t)}\right). \tag{2.30}$$

A solution of the Schrödinger equation is presented by Bardroff et al. [Bar96]. The main results are summarized in the following, considering only the ion motion along the x direction, with $n := n_x$.

The energy eigenstates of a single trapped ion are represented by an energy ladder: The ion motion gives rise to equidistant energy levels, separated by $\hbar\omega_x$. Here, ω_x is the oscillation frequency of the ion, also called *trap frequency*. In addition, the energy levels of the internal two-level system are separated by $\hbar\omega_0$. Figure 2.1 visualizes the resulting level scheme. If the laser is tuned to match energy difference $\hbar\omega_0$, the Hamiltonian in Eq. 2.30 permits coupling between the states $|g\rangle$ and $|e\rangle$ without affecting the motion. This is called the *carrier transition*. Furthermore, it is possible to drive transitions that add or remove phonons from the motion while also driving the internal degree of freedom. Assuming an ion initialized to $|g\rangle\,|n\rangle$, excitation of the Nth *blue sideband* at a frequency of $\omega = \omega_0 + N\omega_x$ leads to the state $|e\rangle\,|n+N\rangle$ and vice versa. Similarly, excitation of the Nth *red sideband* at a frequency of $\omega = \omega_0 - N\omega_x$ transforms the state $|g\rangle\,|n\rangle$ to $|e\rangle\,|n-N\rangle$ and vice versa (see also Fig. 2.1).

Laser light resonant to one of these transitions drives *Rabi oscillations* with effective Rabi frequencies that depend on the initial motional state n and the final motional state $n \pm N$:

$$\Omega_{n,n\pm N} = M_{n,n\pm N}\Omega. \tag{2.31}$$

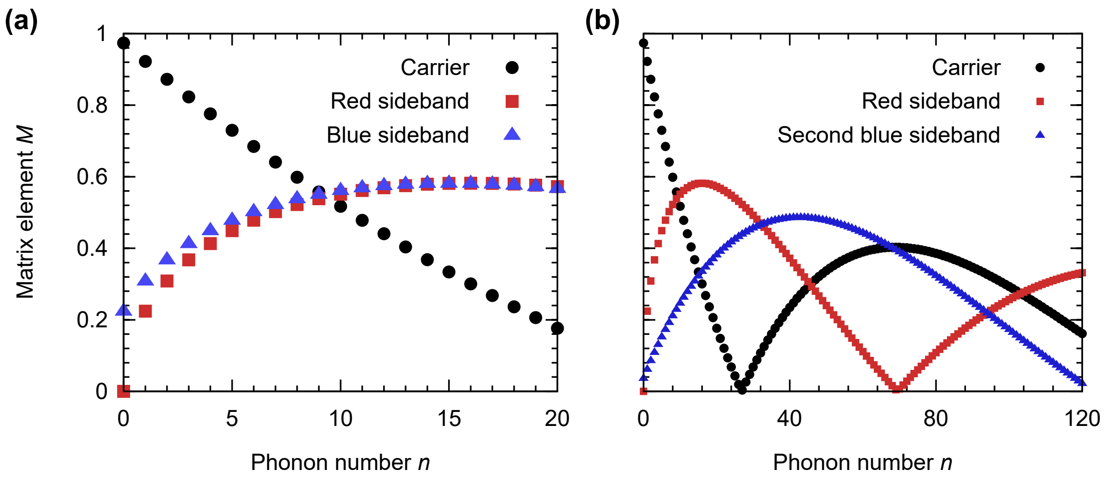

Figure 2.2.: Calculated matrix elements $M_{n,n\pm N}$ for $\eta = 0.23$. **(a)** Carrier ($N = 0$), red ($N = -1$) and blue ($N = +1$) sideband for $n \leq 20$. **(b)** Carrier ($N = 0$), red ($N = -1$) and second blue ($N = +2$) sideband for $n \leq 120$.

The matrix elements are calculated via [Win79]

$$M_{n,n\pm N} = \mathrm{e}^{-\eta^2/2} \, (\mathrm{i}\eta)^N \, \mathcal{L}_n^N(\eta^2) \left(\frac{n!}{(n+N)!} \right)^{\pm 1/2} . \tag{2.32}$$

Here, $\mathcal{L}$ are the generalized Laguerre polynomials, and $\eta = k\sqrt{\frac{\hbar}{2m\omega_x}}$ is the *Lamb-Dicke parameter*. The Lamb-Dicke parameter depends on the projection of the wave vector on the direction of the ion motion k, the trap frequency ω_x, and the ion mass m.

For stimulated Raman transitions that couple to the axial mode of motion, a typical Lamb-Dicke parameter in the experiment is $\eta = 0.23$. Figure 2.2 depicts calculated matrix elements for $N = 0, \pm 1, 2$. The matrix elements for $N = \pm 1$ differ only for small phonon numbers $\lesssim 10$. If a transition is driven while the motion is described by a statistical mixture or a superposition state, the ion undergoes Rabi oscillations for each populated phonon number. Thus, at resonance and after initialization to the ground state, the population of the excited state is

$$p_e(t) = \sum_{n=0}^{\infty} p_n \sin^2 \left(\frac{\Omega_{n,n+N}}{2} t \right) \tag{2.33}$$

with p_n the initial phonon distribution function.

The bare Rabi frequency Ω does not only depend on the power of the laser beam, but also on its polarization and angle with respect to the magnetic-field direction. For this reason, the choice of a magnetic-field axis, in this context also called *quantization axis*, is critical in the experiment.

For electric dipole-allowed transitions, we can intuitively understand this phenomenon by considering a classical oscillating electric charge in three dimensions. In the presence

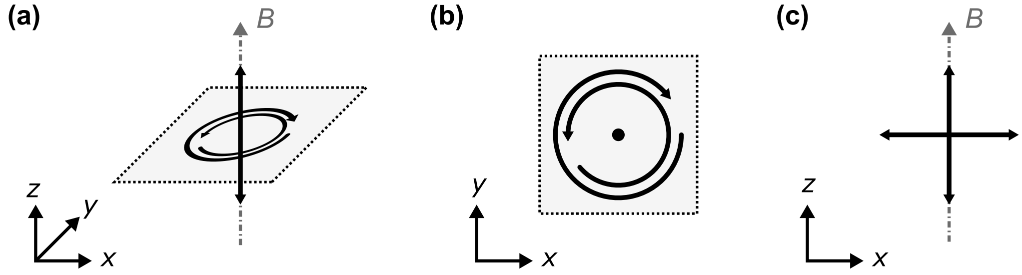

Figure 2.3.: Classical picture of electric-dipole radiation. **(a)** Motion of the electric charge in three-dimensional space. The charge may oscillate along the magnetic-field axis, and circle around the magnetic-field axis. **(b)** View from an observer along the z-axis. Only the circular part is observed. **(c)** View from an observer along the y-axis. The circular motion is observed as linear in horizontal direction.

of a magnetic field, the oscillation can be conveniently expressed by three components that are consistent with the symmetry axis given by the magnetic field: A linear oscillation along the magnetic-field axis that corresponds to π transitions with $\Delta m = 0$, and two circular oscillations perpendicular to the magnetic field axis that correspond to $\sigma_\pm$ transitions with $\Delta m = \pm 1$ (Fig. 2.3(a)). The circular motions may be right- or left-handed, and are therefore accelerated or decelerated by the magnetic field, shifting the frequency of the emitted (or absorbed) light. Figures 2.3(b),(c) show that both circular motions can be simultaneously excited by horizontally polarized light from the x or y direction, and by any linearly polarized light along the z direction. In order to excite only a single circular motion, circularly polarized light along the z direction is required. The linear oscillation may be excited by vertically polarized light traveling along the x or y direction, but does not have a projection along the z axis. Thus, in the experiment, the polarizations and angles of the laser beams relative to the magnetic field have to be chosen according to the desired transitions.

2.3. Motional state reconstruction

Rabi oscillations (Eq. 2.33) are an ideal tool for characterizing the motional state of trapped ions. The matrix elements $M_{n,n\pm N}$ depend on the populated phonon numbers, and thus the phonon distribution function p_n can be extracted from curve fits on measured Rabi oscillations. Since the mapping of matrix elements $M_{n,n\pm N}$ to phonon numbers is ambiguous (see Fig. 2.2), it is in general insufficient to measure Rabi oscillations on a single motional sideband if a high dynamic range is required. This is the case for analyzing the motional excitation after ion-crystal separation, which may readily transfer energies of more than 10^3 phonons.

A combined fit on multiple sidebands yields additional information and extends the dynamic range. For populated phonon numbers $n < 10$, a fit to Rabi oscillations on the carrier, red sideband, and blue sideband transitions yields high precision. For higher phonon numbers, oscillations on the carrier, red sideband, and second red sideband should be recorded, because the matrix elements of the red and blue sidebands are similar.

The reconstruction of *arbitrary* phonon distribution functions p_n is only feasible if the maximum phonon number is restricted to low values, e.g. $n_{\max} <= 10$, because the number of free fit parameters would be overwhelming for higher $n_{\max}$. This technique has been, e.g., successfully applied to low-lying *Fock states* [Zie13]. Also called number states, these states are characterized by a single populated phonon number k, i.e. $p_n = \delta_{nk}$.

If higher phonon numbers are populated, it is generally required to assume a phonon distribution function depending on only a few parameters. Common states in ion trap experiments are *coherent states* and *thermal states*, or a combination thereof.

Coherent states

Coherent states $|\alpha\rangle$ are obtained by applying the *displacement operator* $\hat{D}(\alpha)$ on the vacuum state:

$$|\alpha\rangle = \hat{D}(\alpha)\,|0\rangle \qquad \text{with} \qquad \hat{D}(\alpha) = \exp\left(\alpha\hat{a}^\dagger - \alpha^*\hat{a}\right). \tag{2.34}$$

The *displacement parameter* α can be any complex number, and fully characterizes the state. The phonon number distribution of a coherent state is Poissonian, i.e.

$$p_n^{(\mathrm{coh})}(\alpha) = |\langle n|\alpha\rangle|^2 = \frac{|\alpha|^{2n}}{n!}\mathrm{e}^{-|\alpha|^2} \tag{2.35}$$

with the mean phonon number $\bar{n}_{\mathrm{coh}} = |\alpha|^2$. Coherent states play a crucial role in the field of quantum optics, because they closely resemble the oscillatory behavior of a classical harmonic oscillator. The wave packet of the state in position representation follows the trajectories of a classical particle, and retains its shape at all times.

In segmented ion traps, acceleration along the trap axis creates coherent states. The movement of the potential in shuttling operations essentially causes a classical force on the particles, because the spatial extend of the confining potential is much larger than the wave packet of trapped ions. This classical force leads to an oscillatory motion, described by a coherent state. In a quantum-mechanical picture, the motional excitation caused by shuttling operations is expressed by a displacement operator if the trap frequency remains constant (or varies slowly) during the process [Lau11].

A key feature of the displacement operator $\hat{D}(\alpha)$ is that it can be canceled by another displacement $\hat{D}(-\alpha)$ of the same magnitude, but phase shifted by 180°. This principle has been used to realize fast near-ground- state ion transport [Wal12b, Bow12].

Thermal states

If an ion is coupled to a thermal reservoir, its motion is described by an ensemble with the density matrix

$$\hat{\rho}_{\mathrm{th}} = \frac{1}{\bar{n}_{\mathrm{th}}+1}\sum_{n=0}^{\infty}\left(\frac{\bar{n}}{\bar{n}_{\mathrm{th}}+1}\right)^n |n\rangle\langle n|\,. \tag{2.36}$$

The occupation probabilities of the harmonic-oscillator states are thus thermally distributed:

$$p_n^{(\mathrm{th})} = \frac{\bar{n}_{\mathrm{th}}^n}{(\bar{n}_{\mathrm{th}} + 1)^{n+1}}. \tag{2.37}$$

In ion traps, thermal states are mostly created by the process of Doppler cooling, where the cooling laser is equivalent to a thermal reservoir. Motional excitation of trapped ions due to electrical noise is also described by a thermal process.

One might wonder why it is appropriate to represent the state of a single ion by a statistical ensemble. As the results of projective measurements in quantum mechanics are of statistical nature, it is necessary to repeat experiments many times to obtain expectation values of the desired observables. If the ion reaches thermal equilibrium during Doppler cooling before each experimental run, each repetition of the experiment can be treated as a statistical realization of the same process. In each realization, a different phonon number n is occupied, with the probability given by Eq. 2.37.

Displaced thermal states

For the ion-separation procedure presented in chapter 5, both oscillatory and thermal excitation occur. The motion is then described by *displaced thermal states* with both a coherent displacement α and a thermal mean phonon number $\bar{n}_{\mathrm{th}}$:

$$p_n(\bar{n}_{th}, \alpha) = \langle n| \hat{D}^\dagger(\alpha)\hat{\rho}_{\mathrm{th}}\hat{D}(\alpha) |n\rangle \,. \tag{2.38}$$

By inserting $\hat{\rho}_{\mathrm{th}}$ (Eq. 2.36), we obtain

$$p_n(\bar{n}_{\mathrm{th}}, \alpha) = \sum_{k=0}^{\infty} \frac{\bar{n}_{\mathrm{th}}^k}{(\bar{n}_{\mathrm{th}} + 1)^{k+1}} \left|\langle n|\hat{D}(\alpha)|k\rangle\right|^2 . \tag{2.39}$$

In practice, the summation is truncated appropriately. The matrix elements of the displacement operator are given by [Oli90]

$$\left|\langle n|\hat{D}(\alpha)|k\rangle\right|^2 = \frac{k!}{n!} \mathrm{e}^{-|\alpha|^2} |\alpha|^{2(n-k)} \cdot \left|\mathcal{L}_k^{(n-k)}(|\alpha|^2)\right|^2 \tag{2.40}$$

with $n \geq k$ and the associated Laguerre polynomial $\mathcal{L}_n^{(k-n)}(x)$. For calculating matrix elements with $k < n$, the symmetry $\left|\langle n|\hat{D}(\alpha)|k\rangle\right|^2 = \left|\langle k|\hat{D}(\alpha)|n\rangle\right|^2$ can be utilized.

The mean phonon number of a displaced thermal state is calculated via $\bar{n} = \bar{n}_{\mathrm{th}} + \bar{n}_{\mathrm{coh}} = \bar{n}_{\mathrm{th}} + |\alpha|^2$. Figure 2.4 depicts example phonon distribution functions p_n for varying $\bar{n}_{\mathrm{th}}$ and $\bar{n}_{\mathrm{coh}}$. For low mean phonon numbers $\bar{n} < 1$, only the total mean excitation can be reliably reconstructed from measurement data, because coherent and thermal excitation lead to similar distribution functions. For higher mean phonon numbers, states with mostly coherent excitation can be clearly distinguished from thermal states.

An alternative method for evaluating Eq. 2.38 relies on numerical thermalization of the phonon distribution of a displaced state. A thermalization process of a quantized harmonic oscillator can be modeled by a set of rate equations [Lam97]:

$$\dot{p}_n = \lambda_{\mathrm{h}} \left(np_{n-1} + (n+1)p_{n+1} - (2n+1)p_n\right), \tag{2.41}$$

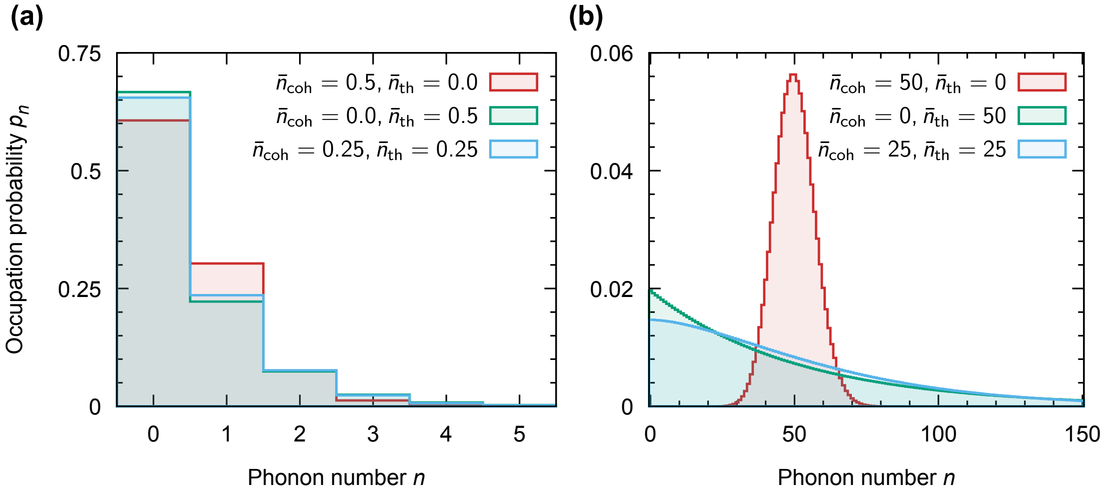

Figure 2.4.: Phonon distribution functions for displaced thermal states with **(a)** $\bar{n} = 0.5$ and **(b)** $\bar{n} = 50$.

where the heating rate is $\dot{\bar{n}} = \lambda_\mathrm{h}$. Defining the heating kernel

$$K_{n,m} = n\delta_{n,m-1} + (n+1)\delta_{n,m+1} - (2n+1)\delta_{n,m}, \tag{2.42}$$

the phonon distribution for a displaced thermal state is obtained from

$$\boldsymbol{p}(\bar{n}_\mathrm{th}, \alpha) = \exp\left(\lambda_\mathrm{h} K t\right) \boldsymbol{p}^{(\mathrm{coh})}(\alpha) \tag{2.43}$$

where $\boldsymbol{p}(\bar{n}_\mathrm{th}, \alpha)$ and $\boldsymbol{p}^{(\mathrm{coh})}(\alpha)$ are vectors representing the respective phonon distributions. The heating kernel $K = D\Lambda D^{-1}$ is a tridiagonal matrix, for which the eigenvectors D and eigenvalues Λ can be computed once and stored for a given truncation phonon number n_max. For arbitrary mean thermal phonon numbers $\bar{n}_\mathrm{th} = \lambda_\mathrm{h} t$, the distribution

$$\boldsymbol{p}(\bar{n}_\mathrm{th}, \alpha) = D \exp\left(\bar{n}_\mathrm{th} \Lambda\right) D^{-1} \boldsymbol{p}^{(\mathrm{coh})}(\alpha) \tag{2.44}$$

is computed by performing three matrix-vector products, which are much faster numerically calculated than Eq. 2.39. Equation 2.44 has thus been used for data evaluation in chapter 5.

3 Operation of the calcium spin qubit

The experimental realization of qubits does not only require well-defined quantum mechanical two-level systems with long coherence times, but also means to manipulate, initialize and measure the state of the qubit. In the following chapter, the implementation of these requirements is explained in detail, similar to the description by Poschinger et al. [Pos09].

The ion species employed in this thesis is $^{40}\mathrm{Ca}^+$. This species is widely used in quantum information experiments, because it features a relatively simple hydrogen-like electronic structure and a vanishing nuclear spin. Most importantly, all required transitions are close to the visible spectrum of light and can be driven with commercial diode lasers. The relevant energy levels and transitions for the experiments in this thesis are sketched in Fig. 3.1.

The qubit is encoded in the two Zeeman sublevels of the $S_{1/2}$ ground state, which offer an infinite lifetime. Since the ground state does not carry angular momentum,

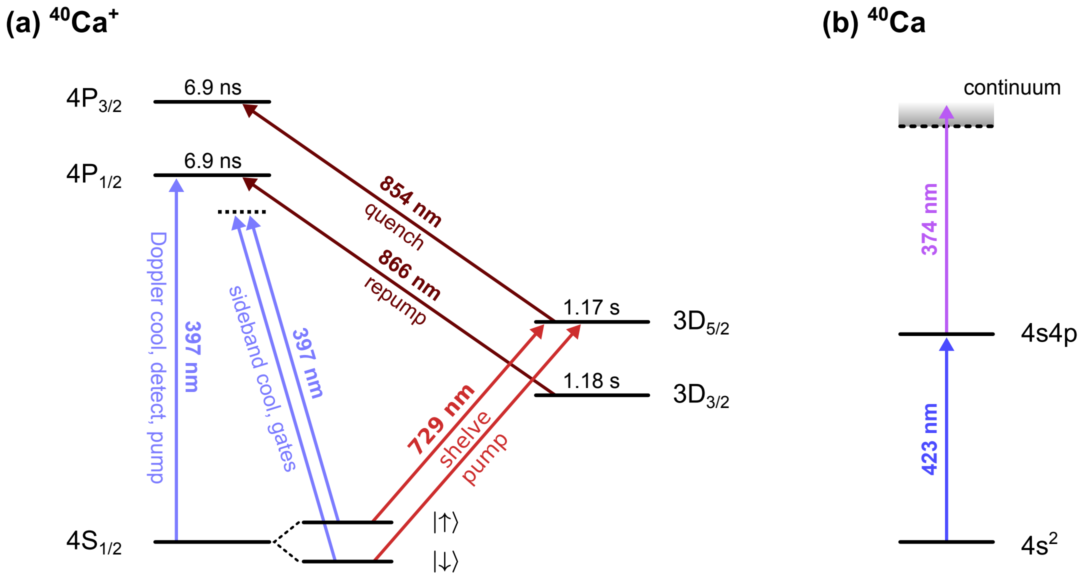

Figure 3.1.: **(a)** Relevant energy levels and laser-driven transitions of the $^{40}\mathrm{Ca}^+$ spin qubit. For each energy level, the decay time is depicted [Jin93, Kre05, Het15]. **(b)** Two-photon ionization scheme in neutral $^{40}\mathrm{Ca}$.

the two Zeeman sublevels directly correspond to the valence electron spin states $|{\downarrow}\rangle$ and $|{\uparrow}\rangle$. A magnetic field at the trap location lifts the degeneracy of the spin states, and leads to a ground-state Zeeman splitting of about $2\pi \cdot 10.5$ MHz. This is sufficient to separate the qubit states and their motional sidebands in frequency space, but smaller than the natural linewidth of the $S_{1/2} \leftrightarrow P_{1/2}$ transition, simplifying Doppler cooling and detection.

3.1. Ionization of calcium ions

Before calcium ions can be loaded in the Paul trap, they have to be created first. The first ionization energy of calcium is about 6.11 eV, which corresponds to a laser wavelength below 203 nm. Operation of such a laser would imply tremendous technical issues and is thus avoided here. Instead, an isotope-selective two-step ionization scheme is used to ionize a beam of neutral calcium atoms inside the trap volume [Gul01]. Two lasers are required to implement this scheme: The first laser is resonant to the $4s^2 \leftrightarrow 4s4p$ transition near 423 nm in neutral calcium. For the second step, a laser with a wavelength below 390 nm is sufficient to excite the atom from the 4s4p state to the continuum. In this work, a laser running at 374 nm drives this transition (see Fig. 3.1(b)). Illumination of both lasers for a few seconds is sufficient to ionize single calcium atoms inside the trap volume.

3.2. Cooling and state initialization

After calcium ions have been ionized, they carry a significant amount of kinetic energy. Ion detection with high efficiency and the formation of stable ion crystals is only feasible if the ions are brought close to rest via *Doppler cooling* [Cir94, Pos10]. The ions are Doppler cooled by simultaneously exciting all Zeeman sublevels of the $S_{1/2} \leftrightarrow P_{1/2}$ transition (in the following termed *cycling transition*) near 397 nm. The $P_{1/2}$ state features a short decay time of 7.1 ns, and thus a large amount of photons are scattered upon laser radiation. Since the laser light is red-detuned from resonance by a few tens of MHz, a net cooling force arises until an equilibrium state is reached.

The $P_{1/2}$ state not only decays to the ground state, but also to the metastable $D_{3/2}$ state with a probability of about 6% [Het15]. In order to avoid population trapping in the metastable state, an additional repump laser beam near 866 nm is employed that transfers the trapped population back to the $P_{1/2}$ state.

After Doppler cooling, the ion motion is described by a thermal state with the mean phonon occupation number $\bar{n}$. For higher trap frequencies, lower mean phonon numbers are reached. In this experiment, typical trap frequencies are $\omega_x = 2\pi \cdot 1.5\text{MHz}$, $\omega_y = 2\pi \cdot 3.8\text{MHz}$, $\omega_z = 2\pi \cdot 4.6\text{MHz}$, and mean phonon numbers of about $\bar{n}_x = 18$, $\bar{n}_y = 6$, $\bar{n}_z = 4$ are attained for a single trapped ion. Here, x denotes the motion along the axial trap direction, and y, z denote the radial modes of motion. Doppler cooling is performed for about 1.5 ms before each experimental cycle.

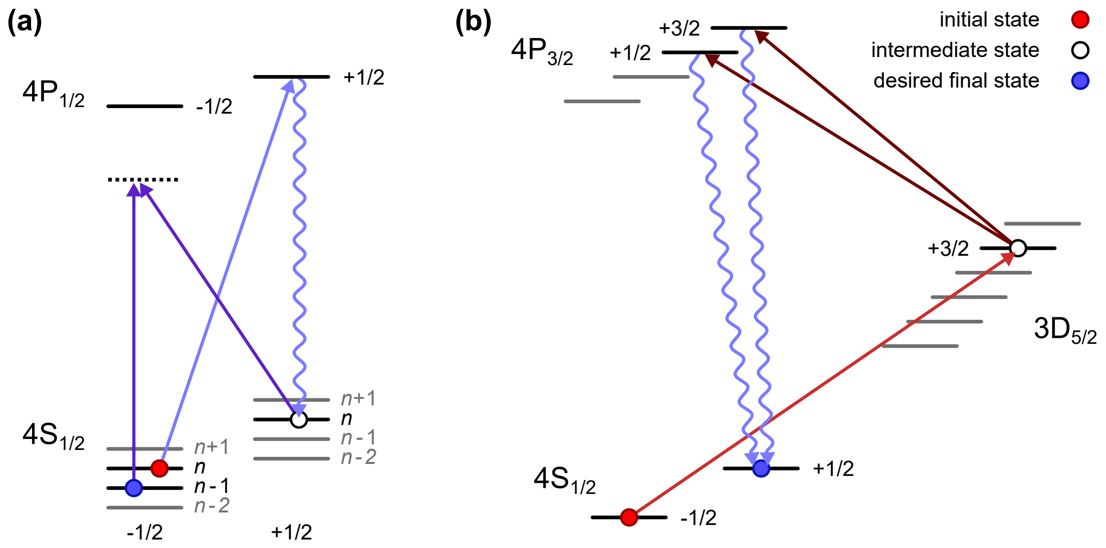

Figure 3.2.: Schematic view of *(a)* sideband cooling and *(b)* frequency selective optical pumping. Straight lines indicate transitions excited by laser light, and curved lines indicate spontaneous decay. Magnetic quantum numbers m and motional quantum numbers n are given for relevant energy levels.

For various experiments, it is desired to further cool the motion close to the ground state via *resolved sideband cooling* [Mon95], a technique that relies on driving red motional sidebands on a narrow transition. Here, stimulated Raman transitions between the qubit states are used to repeatedly perform π-pulses on red sideband transitions, which transform the state $|\uparrow\rangle\,|n\rangle$ to $|\downarrow\rangle\,|n-1\rangle$ (Fig. 3.2(a)).

Spin initialization to the state $|\uparrow\rangle$ is required prior to each laser pulse on the red sideband. If population resided in the $|\downarrow\rangle$ state, a π-pulse on the red sideband would actually *add* a phonon to the motional state. The qubit state is thus initialized to $|\uparrow\rangle$ via optical pumping on the cycling transitions, where only σ_+ transitions are driven to deplete population in the $|\downarrow\rangle$ state. A pulse duration of 2 µs is sufficient to initialize the $|\uparrow\rangle$ state with about 99% efficiency. In total, about 50 pulses on the red sideband with a duration in the $10-20$ µs range are performed to cool the axial mode of motion close to the ground state. For the radial modes of motion, fewer pulses are necessary, but with higher pulse times. Mean phonon numbers below $\bar{n} = 0.1$ are typically reached after sideband cooling.

At the beginning of the cooling sequence, the application of pulses on the second red sideband improves the cooling rate, because two phonons are discarded with a single pulse instead of one. Furthermore, there are certain Fock states for which the Rabi frequencies of the first-order red sideband are close to zero (see Fig. 2.2(b)). Thus, an optimized cooling strategy includes pulses on both first and second order red sidebands [Che17].

Sideband cooling is concluded by optical pumping to the state $|\uparrow\rangle$. Optical pumping on the cycling transitions is strongly dependent on the beam polarization: An imperfect polarization and an imperfect angle between laser beam and magnetic field lead to undesired σ_- contributions, which slightly deplete the $|\uparrow\rangle$ state and limit the fidelity of state preparation. In order to surpass these limitations, additional frequency-selective pumping utilizing the narrow $\mathrm{S}_{1/2} \leftrightarrow \mathrm{D}_{5/2}$ quadrupole transition near 729 nm is used. This pumping scheme is visualized in Fig. 3.2(b): A narrow-band laser at a wavelength near 729 nm drives the dipole-forbidden transition between the $|\downarrow\rangle$ state and the $m = +3/2$ sublevel of the $\mathrm{D}_{5/2}$ metastable state. Due to the small linewidths of the transition and of the laser, this population transfer is frequency-selective and hence does not affect the $|\uparrow\rangle$ state. Complete population transfer is typically achieved within 10µs. Then, the transition $\mathrm{D}_{5/2} \leftrightarrow \mathrm{P}_{3/2}$ is driven by a laser near 854 nm. Transitions to the $m = 1/2$ and $m = 3/2$ sublevels are dipole-allowed, and the population in the $\mathrm{D}_{5/2}$ state is typically depleted within 2 µs. From these sublevels, rapid spontaneous decay occurs preferably to the desired qubit state $|\uparrow\rangle$. The pumping procedure is usually repeated a few times, leading to an occupation probability above 99.9% in the desired state.

3.3. Single-qubit gates

Single-qubit gates are executed by turning on two laser beams that drive stimulated Raman transitions. Both beams are close to resonance of the cycling transition, but sufficiently detuned to avoid population and spontaneous emission from the $\mathrm{P}_{1/2}$ state.

The choice of the detuning Δ is a compromise between desired Rabi frequency, tolerable spontaneous-emission rate, and available laser power: Assuming equal intensity I for both laser beams at the ion position, the Rabi frequency scales as $\Omega \propto I/\Delta$, and the decoherence rate caused by spontaneous emission scales as $R \propto I/\Delta^2$ [Pos10, Appendix A]. If detuning and laser intensities are increased by the same factor, the Rabi frequency remains constant, but the spontaneous emission rate is reduced. The detuning in the experiments typically ranges between $2\pi \cdot 0.3 - 3$ THz depending on the application.

The beam geometry has a significant impact on the quality of single-qubit rotations. The relative angle of the two laser beams determines the effective wave vector $\vec{k}_{\mathrm{eff}} = \vec{k}_1 - \vec{k}_2$ of the stimulated Raman transitions, and the projection of $\vec{k}_{\mathrm{eff}}$ to the motional modes of an ion crystal determines the coupling strength to the respective modes. Coupling to the motion is desired for spectroscopy of motional frequencies and two-qubit gates, but leads to additional errors for single-qubit gates, because the Rabi frequency depends on the populated phonon numbers in the motion. In general, multiple phonon numbers are populated, and Rabi oscillations with different Rabi frequencies are simultaneously driven, which leads to decoherence. This effect can be eliminated by employing a pair of co-propagating laser beams, where the effective wave vector $\vec{k}_{\mathrm{eff}}$ vanishes. With co-propagating laser beams and a Raman detuning of about $\Delta = 2\pi \cdot 3.1$ THz, high-quality single qubit gates with an error per gate of $5.1(2) \cdot 10^{-5}$ have been achieved in the present experiment [Kau17a].

Resonant driving of a single qubit is described by the unitary operator

$$\hat{R}_\phi(\theta) = \exp\left(-\mathrm{i}\,\frac{\theta}{2}\left(\hat{\sigma}_x \cos\phi + \hat{\sigma}_y \sin\phi\right)\right) \tag{3.1}$$

with the Pauli matrices and the basis states

$$\hat{\sigma}_x = \begin{pmatrix} 0 & 1 \\ 1 & 0 \end{pmatrix}, \quad \hat{\sigma}_y = \begin{pmatrix} 0 & -\mathrm{i} \\ \mathrm{i} & 0 \end{pmatrix}, \qquad \begin{pmatrix} 1 \\ 0 \end{pmatrix} \equiv |{\uparrow}\rangle\,, \quad \begin{pmatrix} 0 \\ 1 \end{pmatrix} \equiv |{\downarrow}\rangle\,. \tag{3.2}$$

The rotation angle ϕ on the Bloch sphere is controlled by the phase of the light field, and the pulse area $\theta = t\Omega$ is experimentally set by a laser-pulse time t and Rabi frequency Ω [Sch13].

3.4. Two-qubit gate

A universal set of quantum gates for realizing arbitrary unitary operations on multiple qubits not only requires the physical implementation of single-qubit gates, but also one type of gate acting on two qubits. This experiment relies on a *phase gate* expressed by the unitary operator

$$\hat{G} = \begin{pmatrix} \mathrm{e}^{\mathrm{i}\pi/2} & 0 & 0 & 0 \\ 0 & 1 & 0 & 0 \\ 0 & 0 & 1 & 0 \\ 0 & 0 & 0 & \mathrm{e}^{\mathrm{i}\pi/2} \end{pmatrix} \tag{3.3}$$

in the logical basis

$$\begin{pmatrix} 1 \\ 0 \\ 0 \\ 0 \end{pmatrix} \equiv |{\uparrow\uparrow}\rangle\,, \quad \begin{pmatrix} 0 \\ 1 \\ 0 \\ 0 \end{pmatrix} \equiv |{\uparrow\downarrow}\rangle\,, \quad \begin{pmatrix} 0 \\ 0 \\ 1 \\ 0 \end{pmatrix} \equiv |{\downarrow\uparrow}\rangle\,, \quad \begin{pmatrix} 0 \\ 0 \\ 0 \\ 1 \end{pmatrix} \equiv |{\downarrow\downarrow}\rangle\,. \tag{3.4}$$

A possible physical implementation of $\hat{G}$ is the *geometric phase gate* [Lei03b], which offers an intrinsic resistance to certain experimental imperfections and can be implemented by using the Raman laser beams that are already present for sideband cooling and single-qubit gates. In the following, we outline the working principle of the geometric phase gate based on the explanation by Leibfried et al. [Lei03b]. Systematic errors of this gate scheme have been thoroughly investigated by Ballance [Bal14].

The interaction is driven by two orthogonally propagating laser beams, with the effective wave vector $\vec{k}_{\text{eff}}$ aligned perpendicular to the trap axis. A standing-wave pattern arises in the overlapping region of both laser beams, where the polarization is periodically varying between left circular and right circular. The regions pertaining to left and right circular polarization travel along the direction of $\vec{k}_{\text{eff}}$ (Fig. 3.3(a)). At the positions of the ions, the polarization oscillates at a frequency equivalent to the frequency difference $\Delta\omega$ between both laser beams.

Circularly polarized optical fields give rise to a differential AC Stark shift between the qubit states of both ions, leading to a spin-dependent optical dipole force $F = \pm F_0 \sin(\Delta\omega t - \varphi_0)$, where the sign of the force depends on the ion spin. If $\vec{k}_{\text{eff}}$ is perfectly aligned at a 90° angle relative to the trap axis, the phase offset φ_0 is identical for both ions. The phase is only well-defined if the size of the ions' wave packets is small

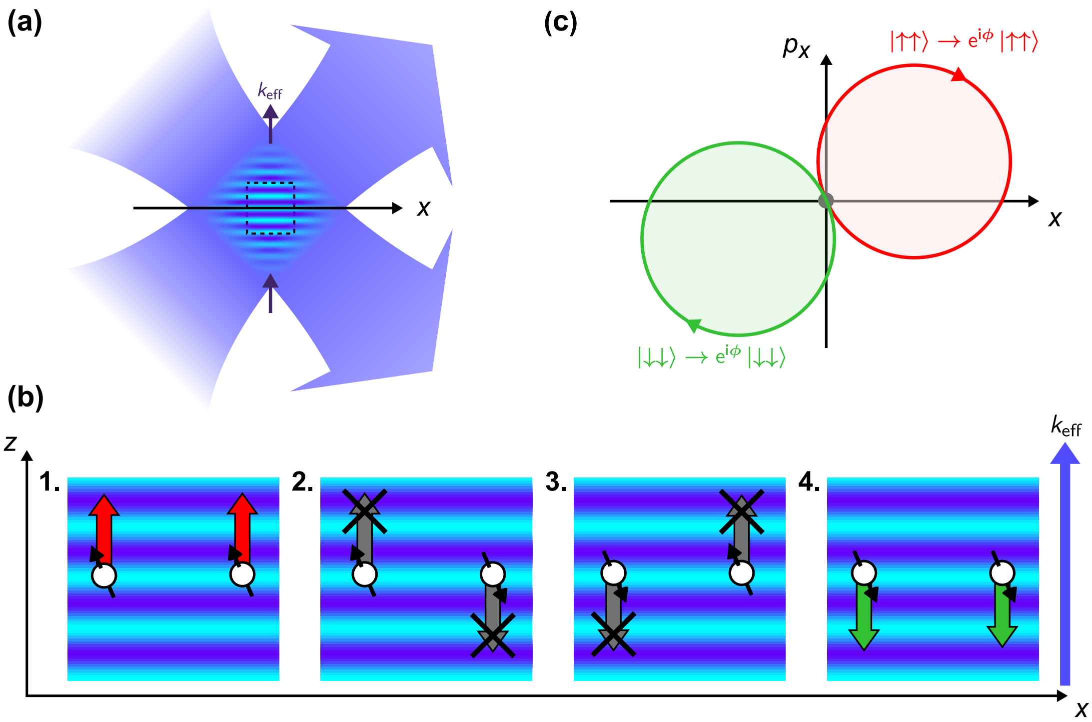

Figure 3.3.: Geometric phase gate. **(a)** Beam geometry relative to the trap axis x. The angles of the laser beams are chosen such that the effective wave vector $\vec{k}_{\text{eff}}$ is aligned perpendicular to the trap axis. **(b)** Forces arising from the oscillating polarization pattern for all possible spin configurations of the ions. If the force is resonant to the oscillation frequency of the center-of-mass mode, cases 2. and 3. are forbidden, because these require resonance to the oscillation frequency of the rocking mode. **(c)** Trajectories in phase space for a detuned force acting on the center-of-mass mode, in the rotating frame of the ion motion. The accumulated phase ϕ is proportional to the enclosed area of the loops. (initially published in [Bru17] and modified)

compared to the wavelength of the laser beams. This is only the case if the ions are cooled close to the ground state of motion.

Two normal modes of motion can be excited by the optical dipole force: The center-of-mass mode at frequency ω_{COM}, where both ions oscillate in phase, and the rocking mode at frequency $\omega_{\text{R}} = \sqrt{\omega_{\text{COM}}^2 - \omega_{\text{x}}^2}$, where both ions oscillate by 180° out of phase. Here, ω_{x} denotes the oscillation frequency of the axial center-of-mass mode. A significant excitation only occurs if the driving force is resonant to a normal mode.

Let us discuss the case of $\Delta\omega = \omega_{\text{COM}}$, i.e. when the force is resonant to the center-of-mass mode. In order to excite the motion, the force on both ions has to match the oscillation pattern of the center-of-mass mode (Fig. 3.3(b)). If the ion spins are prepared in the $|\uparrow\uparrow\rangle$ or $|\downarrow\downarrow\rangle$ states, the force on both ions is identical and the center-of-mass mode is excited. For the $|\uparrow\downarrow\rangle$ and $|\downarrow\uparrow\rangle$ states, the force is acting in opposite directions, which corresponds to the oscillation pattern of the rocking mode. However, since we assume

$\Delta\omega = \omega_{\mathrm{COM}}$, the driving force is off-resonant to the rocking-mode frequency, and the mean excitation is negligible.

Rather than driving the center-of-mass mode resonantly, a slight detuning δ is added to the driving frequency such that $\Delta\omega = \omega_{\mathrm{COM}} + \delta$. The driving force is therefore slightly asynchronous with the motion, but re-synchronizes after a duration $T = 2\pi/\delta$. In the experiment, the detuning δ is usually in the range of $2\pi \cdot 10 - 30$ kHz. During T, the ions undergo circular trajectories in phase space (Fig. 3.3(c)), and return to the initial position. During this process, a phase ϕ proportional to the enclosed phase-space area is acquired [Lei03b]. By tuning the laser power, we can adjust the enclosed phase-space area and choose a phase of $\phi = \pi/2$, effectively implementing the operator $\hat{G}$ (Eq. 3.3).

In the experiment, the geometric phase gate is implemented by performing two loops in phase space, with a π-pulse on the ion spins between both loops. In this case, the laser power is tuned such that the ions acquire a phase of $\phi = \pi/4$ during each loop. This technique suppresses certain error sources, such as unequal illumination of the ions by the laser beams. The duration of the two-loop gate is usually between $30 - 100$ µs.

3.5. Spin readout

After the application of gate operations, the spin state of the ions has to be analyzed. Complete information about the spin wave function $|\Psi\rangle = a\,|\uparrow\rangle + b\,|\downarrow\rangle$ cannot be reconstructed in a single experimental run. Instead, measurements on quantum states are *projective*: Upon measurement, the wave function randomly collapses to one of the basis states $|\uparrow\rangle$ and $|\downarrow\rangle$, with the respective probabilities $|a|^2$ and $|b|^2$. Thus, in order to reconstruct the parameters a and b, an experiment has to be repeated under the same conditions to obtain the probabilities $|a|^2$ and $|b|^2$. Experiments where the relative phase between both spin states is of interest require an additional $\pi/2$ laser pulse is required prior to readout, which transforms the relative phase to a population imbalance (see Sec. 6.1).

For performing a projective measurement of the ion spin, population in the $|\uparrow\rangle$ state is first transferred to the long-lived $\mathrm{D}_{5/2}$ state by the narrowband laser near 729 nm (Fig. 3.4(a)). This transfer is also called *shelving* [Nag86]. Two *rapid adiabatic passage* pulses [Mal01] transfer population from the $|\uparrow\rangle$ state to the $m = +1/2$ and $m = -3/2$ sublevels of the $D_{5/2}$ manifold. Starting at $t = 0$, the frequency ω_{L} of the laser pulse is linearly swept through the qubit resonance ω_0 via

$$\omega_{\mathrm{L}}(t) = \omega_0 + \delta\left(2\frac{t}{T} - 1\right) \tag{3.5}$$

with the total pulse duration T and the maximum detuning δ. In theory, best efficiency is reached for $\delta \to \infty$. Here, a maximum detuning of $\delta = 2\pi \cdot 120$ kHz is chosen to avoid off-resonant driving of transitions from the $|\downarrow\rangle$ level to the $\mathrm{D}_{5/2}$ state. The pulse duration in the experiment is $T = 200$ µs. The laser intensity is varied according to

$$I(t) = I_0 \sin^2\left(\pi\frac{t}{T}\right) \tag{3.6}$$

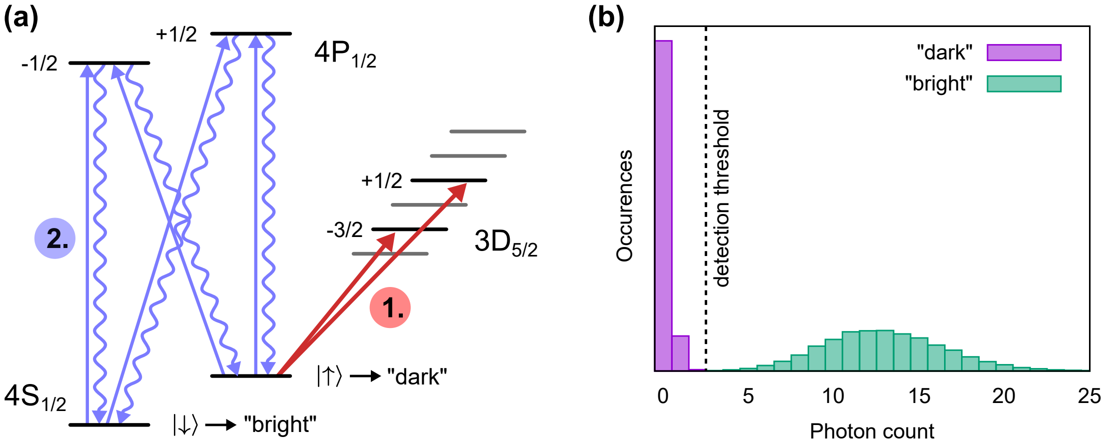

Figure 3.4.: Experimental spin readout. **(a)** Schematic view of relevant transitions. First, population in the state $|\uparrow\rangle$ is transferred to the $m = +1/2$ and $m = -3/2$ sublevels of the $D_{5/2}$ state. Then, the $\mathrm{S}_{1/2} \leftrightarrow \mathrm{D}_{5/2}$ cycling transition is excited, and photons are only scattered if the ion has been projected to the $|\downarrow\rangle$ state. Spontaneous decay to the $\mathrm{D}_{3/2}$ state is counteracted by the repump laser at 866 nm. This is omitted for simplicity. **(b)** Histogram of observed photon counts during a detection time of 500 µs. A predetermined detection threshold serves to classify the observed photon count as "dark" or "bright".

with I_0 the intensity on resonance. Rapid adiabatic passage pulses enable highly efficient broadband population transfer insensitive to variations in the Rabi frequency. The population transfer is therefore robust to laser-frequency and power drifts.

Significant loss of shelving efficiency is only observed in experiments where the motional state of the ions is strongly excited by heating or oscillatory excitation. This is because the Rabi frequency of the relevant transitions is affected by the motional state of the ions. Moreover, transition matrix elements of higher-order motional sidebands are enhanced for highly excited motional states, which leads to undesired off-resonant depletion of the $|\downarrow\rangle$ state. For experiments with strong motional excitation, it is therefore necessary to characterize readout errors in separate measurements.

After shelving, the cycling transition is driven by the laser near 397 nm that is also used for Doppler cooling (Fig. 3.4(a)). If the ion has been projected to the ground state, scattered photons are observed by a photomultiplier tube. Compared to the initial Doppler cooling step, the laser power is increased by a factor of about 5 to maximize the number of scattered photons. If the ion has been projected to the $\mathrm{D}_{5/2}$ state, the laser near 397 nm is non-resonant and the number of observed photons is greatly reduced.

Figure 3.4(b) depicts a histogram of observed photon counts within a detection time of 500 µs. Here, repeated experimental runs have been performed where the ion has been alternately prepared in the ground state ("bright") and the $\mathrm{D}_{3/2}$ metastable state ("dark"). Both states yield photon count distributions that can be clearly separated by a fixed threshold. This threshold can be used in arbitrary experiments to classify the observed result as "dark" or "bright", corresponding to the respective spin states $|\uparrow\rangle$ and $|\downarrow\rangle$ prior to shelving.

Longer detection times further separate both photon count distributions and reduce the error of the state-discrimination procedure. However, spontaneous decay from the metastable state is also aggravated and leads to readout errors. In the present experiment, a detection time of about 0.7 ms is an optimal compromise between both effects, and combined errors for state preparation and measurement ("SPAM") as low as $8 \cdot 10^{-4}$ are observed [Kau17c].

Detection of state-dependent fluorescence concludes an experimental run. The subsequent experimental cycle is initiated by Doppler cooling, where the laser near 854 nm is turned on to deplete remaining population in the metastable $D_{5/2}$ state.

4 Experimental Apparatus

This chapter presents the experimental apparatus in detail. The core of the experiment is the ion trap (Sec. 4.1), mounted inside a vacuum chamber. A μ-metal magnetic-shielding enclosure contains the trap setup (Sec. 4.2), which consists of a vacuum chamber, coils and permanent-magnet rings for magnetic-field generation (Sec. 4.4), and laser beam-focusing optics (Sec. 4.3). An electronic supply system generates time-dependent voltages for the trap electrodes and performs switching of laser beams (Sec. 4.5).

4.1. Ion trap

Two versions of segmented ion traps have been operated for the experiments presented in this thesis (Fig. 4.1), with designs similar to [Sch09]. The version one (V1) trap has been designed and built by Claudia Warschburger. It consists of two gold-coated chips, which constitute the trap electrodes, and an insulating layer that separates the two chips. Trapped ions reside in a slit that defines the center of the trap and spatially separates the DC and radio-frequency (RF) electrodes of the chips. In total, these electrodes form 32 independent segments. The width of the trap slit is about $w = 400$ µm, the distance between the center of neighboring electrodes is about $d = 230$ µm, and the thickness of the insulating layer is about $t = 250$ µm. The work on ion crystal separation (chapter 5) has been conducted with this trap.

A key property of ion traps is the electrical noise arising from the trap surface. This electrical noise heats the motion of the ions, and is thus commonly characterized by the *heating rate*, given by the number of phonons added to the motional state within unit time. In the V1 trap, a typical axial heating rate of about 2000 phonons/s at an oscillation frequency of $2\pi \cdot 1.4$MHz has been observed, thus limiting its use for experiments on a long timescale. The physical mechanisms leading to this electrical noise are, in general, not well understood [Bro15].

For the version two (V2) trap, it has been attempted to reduce electrical noise by increasing the thickness of the gold layer from about 0.5 µm to 8 µm, and by increasing the distance between the trapped ions to the nearest dielectrics from about 400 µm to 700 µm. The distance between the center of neighboring electrodes has been reduced to about 200 µm to ease ion-crystal separation.

The V2 trap has been designed and built in a collaborative project involving Henning Kaufmann, Christian Schmiegelow, Marco Dillmann, and Max Hettrich. A detailed description of the trap is given by Kaufmann [Kau17a]. The most remarkable improvement

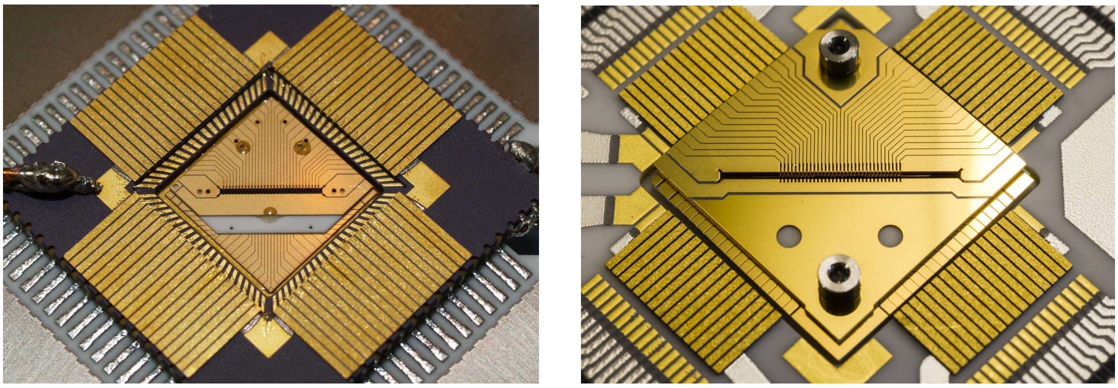

Figure 4.1.: Photographs of the segmented ion traps used within this thesis. Left: Version one (V1) trap, which has been employed for measurements in chapter 5 (Image taken by Claudia Warschburger). Right: Version two (V2) trap, used for measurements in chapters 6 and 7 (Image taken by Henning Kaufmann).

is a reduction of the heating rate of all motional modes to the $3 - 20$ phonons/s range, enabling measurements with long wait times (see chapters 6 and 7). Furthermore, the electrical-field stability has been substantially improved, reducing the calibrational effort for ion-crystal separation (see Sec. 5.1).

4.2. Trap setup

The ion trap is mounted inside a vacuum chamber with a diameter of around 25 cm. A magnetic-shielding enclosure[1] with outer dimensions of 510 mm (height) × 625 mm × 625 mm protects the setup from ambient magnetic-field fluctuations. It consists of two layers of μ-metal (an alloy of 80% Ni and 20% Fe with a permeability of about 80000), each with 2 mm thickness and separated by a 6 mm Al layer. The enclosure is composed of one bottom part and two removable top parts, where overlapping μ-metal lids ensure that the shielding efficiency is not compromised by the gaps between the parts (Fig. 4.2). Attenuation factors for the magnetic field amplitude in the range between 150 and 300 for signal frequencies between 0 Hz and 100 kHz have been measured [Kes12].

An ion-getter vacuum pump[2] is connected via a 30 cm long tube to the vacuum chamber, and resides outside of the magnetic-shielding enclosure because it contains magnetic parts. An additional non-evaporable getter pump[3] (not shown in Fig. 4.2) is mounted close to the ion trap, and does not require electrical connections or magnetic parts for operation. Both pumps maintain a pressure below 10^{-11} mbar inside the vacuum chamber.

---

[1] Sekels GmbH, Ober-Mörlen, Germany

[2] NEXTorr D100-5, SAES Getters, combination of non-evaporable getter and sputter ion pump

[3] CapaciTorr D100, SAES Getters

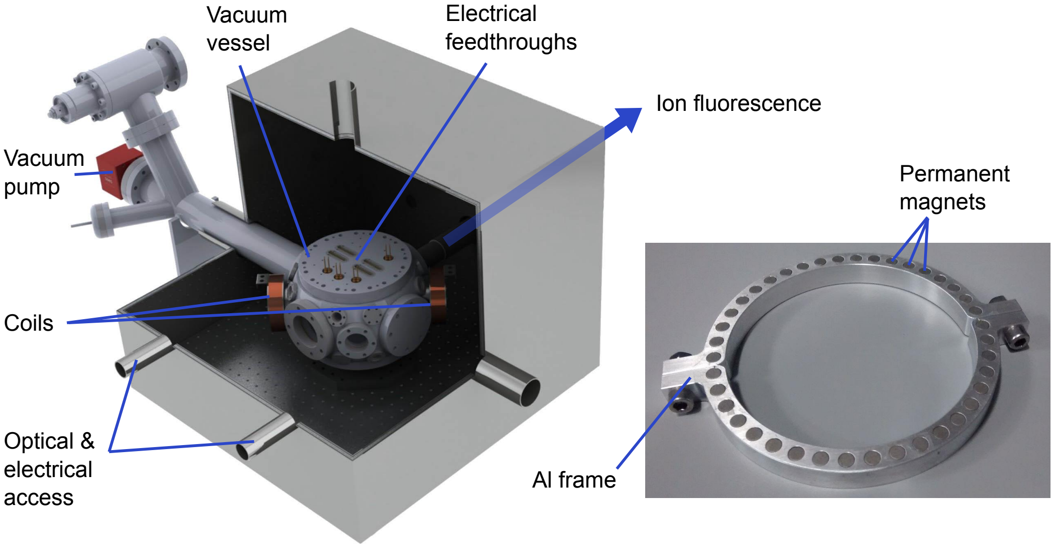

Figure 4.2.: Left: Rendered image of the ion-trap setup with magnetic-shielding enclosure, shown with one top part removed. The laser-focusing optics are not shown. Electrical signals and optical single-mode fibers are supplied via the holes with cylindrical sleeves. An additional hole on the back side allows for imaging of fluorescence emitted from the trapped ions (Image by Claudia Warschburger, taken from [Rus16]). Right: Photograph of an aluminum frame bearing permanent magnets. Two frames have been built and directly mounted on the magnetic-field coils.

Laser beams are supplied to the trap setup via single-mode fibers. All fibers and electrical signals, as well as the free-space photon collection optics, are fed into the enclosure through circular holes with diameters of up to 100 mm. The holes feature cylindrical μ-metal sleeves of 100 mm length outside the enclosure in order to retain shielding efficiency.

The radio-frequency (RF) electrodes of the ion trap are supplied with an alternating voltage of about 320 V peak-to-peak at a frequency of $\Omega_{\mathrm{rf}} = 2\pi \cdot 33$ MHz. The voltage is generated by an RF source[4] and amplified by a water-cooled RF amplifier[5]. The output of the amplifier is fed into the magnetic-shielding enclosure, where the voltage is further amplified by a helical resonator and guided to the trap. The RF voltage is actively stabilized in order to provide stable ion oscillation frequencies along the radial directions of the trap. A detailed description of the circuit is given by Kaufmann [Kau17a].

A calcium oven inside the vacuum chamber continuously directs a vapor of calcium atoms to the trap. These atoms are ionized by laser beams on demand (Sec. 3.1). The oven is composed of a stainless steel tube filled with calcium granules, heated by an electrical current of about 2.9 A[6]. About 2 W of heat is dissipated by the oven and the electrical wires. The oven is constantly heated during experiments to avoid thermal

---

[4] Rohde & Schwarz SMB100A

[5] Mini-Circuits ZHL-5W-1

[6] supplied by an Agilent E3646A power supply in current control mode

drifts of the trap setup. A negative impact on the qubit-coherence time could not be observed.

4.3. Optical setup

The optical setup can be considered as two parts: (1) The laser-focusing optics inside the magnetic-shielding enclosure, and (2) the laser setup outside of the enclosure, where all lasers are installed and the beams are controlled by either mechanical shutters or *acousto-optic modulators* (AOMs).

Acousto-optic modulators diffract light via sound waves in a quartz crystal. The sound waves are created by a piezoelectric transducer, driven by an external RF source. In a nutshell, acousto-optic modulators transfer the amplitude, frequency, and phase of an RF signal to a laser beam. In the present setup, AOMs are used in *single-pass* and *double-pass* configurations. In a single-pass configuration, the laser beam passes the crystal once, and is diffracted at an angle θ that depends on the frequency of the RF source. Up to 90% diffraction efficiency can be achieved if the size of the laser beam is sufficiently large. Typical diffraction efficiencies in the experiment range from 60% to 85%. In a double-pass configuration, a mirror reflects the laser beam back to the AOM after the first diffraction, where it is diffracted a second time at an angle $-\theta$. A double-pass configuration offers the advantage that the frequency shift is applied twice (permitting higher total frequency shifts), and that the laser position is independent of the diffraction angle. Drawbacks of double-pass configurations are higher space requirements and a reduction of the total diffraction efficiency. More information is, e.g., given by Donley et al. [Don05].

In the course of this thesis, the beam-focusing optics inside the magnetic-shielding enclosure have been entirely reworked. The following discussion therefore focuses on this part of the optical setup. Figure 4.3 gives an overview over the laser-beam configuration, and Fig. 4.4 depicts the beam-focusing optics in the regions marked as (a)-(d) in Fig. 4.3.

Single-mode fibers guide all beams from the laser setup into the enclosure. Since beams exiting the fibers are divergent, lenses with focal lengths $f \leq 12.5$ mm first create collimated beams. A second lens then focuses each laser beam to the trap position. In order to avoid scattered laser light at the trap electrodes, the $1/e^2$ beam diameter of the Gaussian laser beams at the trap location must be much smaller than the width of the trap slit of about 400 µm. Smaller beam diameters also lead to higher field intensities at the location of the ion, i.e. less laser power is required for attaining similar Rabi frequencies. In the present setup, all beams, as well as the fluorescence-collection optics, are focused to the same trap segment, the *laser interaction zone*. A dedicated laser-alignment camera eases the process of aligning laser beams to a specific trap segment.

Before the beam-focusing optics was installed, the expected beam diameters at the trap location had been determined in a separate test setup by a beam profiler[7]. For all beams, $1/e^2$ diameters in the range of 50 µm and 100 µm had been measured (Table 4.1).

---

[7] Thorlabs BC106-VIS CCD Camera Beam Profiler

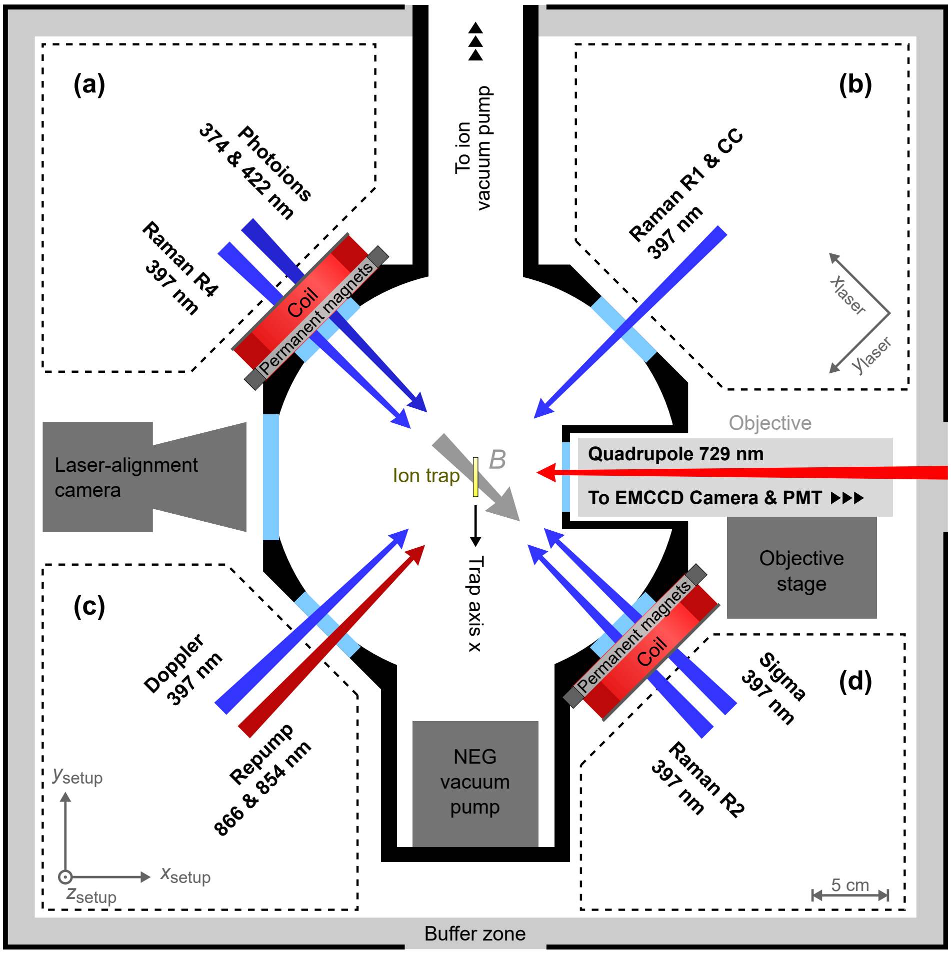

Figure 4.3.: Top view on the optical setup inside the magnetic-shielding enclosure. The *buffer zone* is occupied by the upper parts of the μ-metal shielding. In the regions (a)-(d), additional optics is installed in order to focus the laser beams to the trap and to prepare the correct beam polarizations. A more detailed overview on the optics is shown in Fig. 4.4.

Since a beam profiler cannot be placed at the location of the ion trap, the diameters might slightly deviate in the final setup. If further knowledge about the beam profile at the trap location is desired, a trapped ion may serve as a high-resolution probe in future measurements [Sch16b].

All beams can be adjusted remotely via piezo-controlled mirror holders[8] or translation stages[9], each of them featuring two motorized axes for vertical and horizontal beam alignment. The models in the present setup do not require a connection to a power-supply unit to maintain their position, and thus do not introduce magnetic noise near the ion trap. For monitoring laser powers remotely, small fractions of all laser beams are

---

[8] 8807 Picomotor Center Mount, New Focus

[9] 9061-XZ-M translation stages with 8302 Tiny Picomotor actuators, New Focus

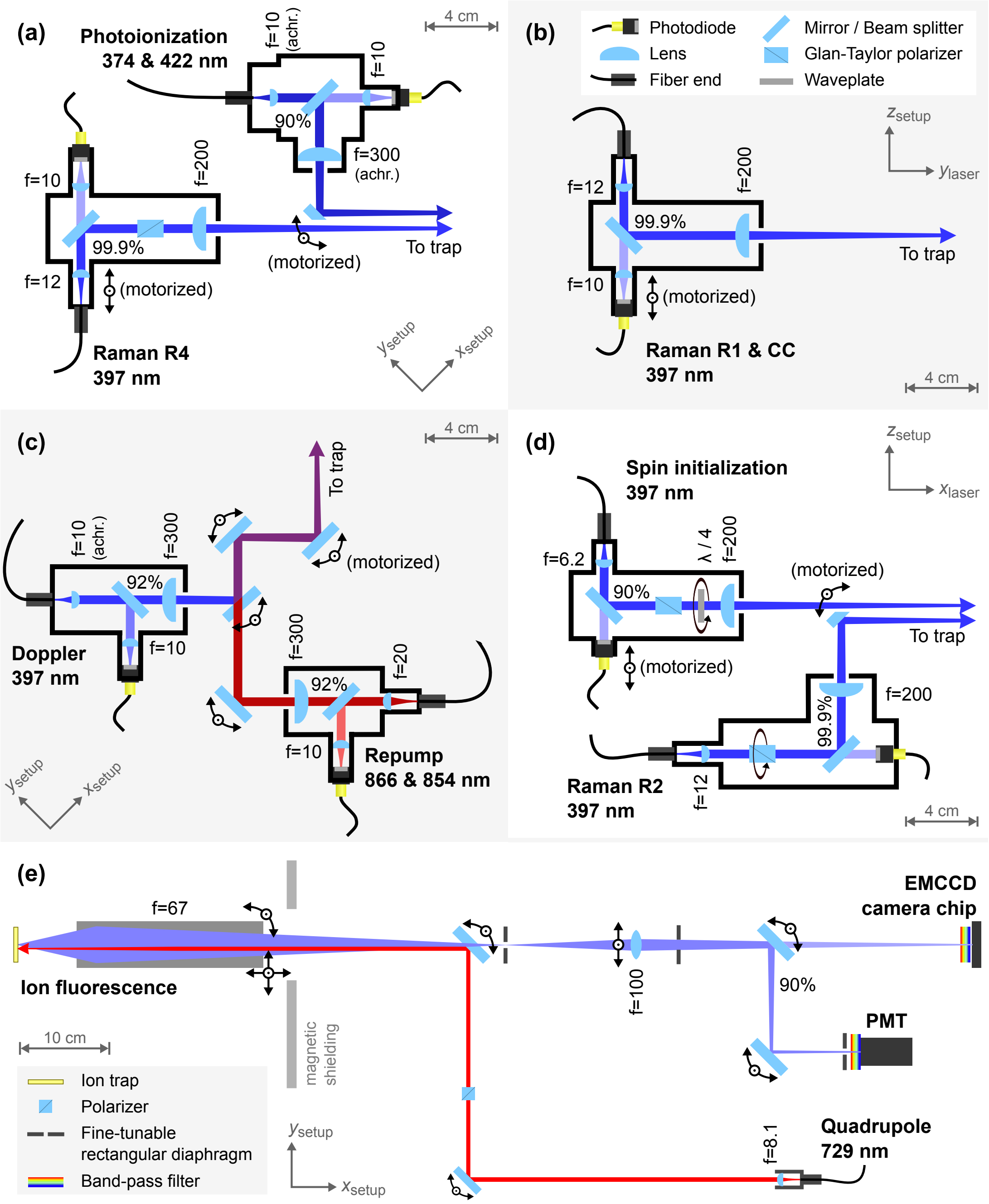

Figure 4.4.: Detailed view on the optical setup corresponding to the regions (a)-(d) in Fig. 4.3. In (e), the optical setup for collecting ion fluorescence is shown. For lenses, the respective focal lengths in mm, and for beam splitters, the respective extinction rations are given. Black arrows depict fine-tunable degrees of freedom, and black borders indicate optics mounted within the same housing (Thorlabs Cage Systems).

Name	$\boldsymbol{\lambda}$ **(nm)**	**Control**	**Pol.**	**Power**	$\sphericalangle(\vec{k},\vec{B})$	Δm	d **(µm)**
Quadrupole	729.347	AOM (2x)	H	15 mW	45°	$0, \pm 2$	75
Doppler	396.959	AOM (2x)	H	50 µW	90°	0	75
Spin init.	396.959	AOM (2x)	R	30 µW	180°	+1	90
Repump	866.451	AOM (2x)	D	25 µW	90°	$0, \pm 1$	90
Quench	854.443	AOM (2x)	$\overline{\mathrm{D}}$	10 µW	90°	$0, \pm 1$	90
Photoion	374	shutter	V	1 mW	0°	±1	75
Photoion	422.791	shutter	H	4 mW	0°	±1	90
Raman R1	396.56	AOM (1x)	H	2 mW	90°	0	50
Raman CC	396.56	AOM (1x)	V	2 mW	90°	±1	50
Raman R2	396.56	AOM (1x)	H	200 µW	180°	±1	50
Raman R4	396.56	AOM (1x)	H	2 mW	0°	±1	50

Table 4.1.: Properties of all laser beams at the trap location. λ denotes the vacuum wavelength. Polarizations are either horizontal (H), vertical (V), diagonal (D), anti-diagonal ($\overline{\mathrm{D}}$), or right circular (R). The polarization and the angle between the laser beam and the magnetic field $\sphericalangle(\vec{k},\vec{B})$ determines the allowed transitions Δm. The diameter d denotes the $1/\mathrm{e}^2$ width of the laser beam, as measured by a beam profiler in a separate setup (see text).

branched off by beam-splitters and focused to photodiodes[10]. All photodiode amplifiers reside outside of the magnetic-shielding enclose. In the following, we discuss the generation and control of each beam in more detail. Table 4.1 summarizes the properties of all laser beams.

Ion-fluorescence detection

Ion-fluorescence light near 397 nm for qubit detection (see Sec. 3.5) is collected by an imaging objective[11] and detected by a photomultiplier tube[12] (PMT) and an EMCCD camera[13], both of which reside outside the magnetic-shielding enclosure at a distance of about 102 cm to the ion trap (see Fig. 4.4(e)). The ions are imaged to the sensor of the EMCCD camera with a magnification of about 15. In contrast to the PMT, the EMCCD camera allows for resolving individual ions within ion crystals, but requires a 2-3 times longer detection time for dark/bright discrimination of a single ion. A beam splitter directs 90% of the light to the PMT and only 10% of the light to the EMCCD camera, which is mainly utilized for measurements of ion positions and for monitoring purposes. A total of three rectangular diaphragms block laser light scattered at the trap electrodes, and band-pass filters[14] suppress light at wavelengths outside the range of about 390 nm - 400 nm.

---

[10] Thorlabs SM05PD1A

[11] $f \approx 67$ mm, $d = 45$ mm, $l = 192$ mm, S6ASS2241/045 SILL 132177, Sill Optics GmbH & Co. KG

[12] Photon counting head H10682-210, Hamamatsu Photonics K.K.

[13] Andor iXon, Model No. DV860DCS-UVB

[14] Semrock FF01-395/11 for the PMT, and Edmund 394 #65-131 for the EMCCD camera

Qubit readout of a two-ion crystal requires discrimination between four states: (1) dark & dark, (2) dark & bright, (3) bright & dark, (4) bright & bright. The PMT only allows for measuring the number of bright ions, i.e. it cannot distinguish between case (2) and (3). In many experiments, this information is already sufficient. If the complete information is required, it can be obtained by using either the EMCCD camera or by separating the ion crystal as presented in chapter 5. After an ion crystal has been separated, fluorescence of the individual ions can be consecutively measured by the PMT and all four states can be discriminated.

729 nm for shelving and qubit initialization

The laser beam for driving the $S_{1/2} \leftrightarrow D_{5/2}$ quadrupole transition at a wavelength of 729.347 nm for shelving (see Sec. 3.5) and qubit initialization (Sec. 3.2) is generated by a titanium-sapphire laser[15]. The laser is frequency stabilized to a high-finesse Fabry-Perot cavity[16] via the Pound-Drever-Hall technique [Bla01, Mac12]. The beam is controlled by an AOM in double-pass configuration, supplied to the setup via a single-mode fiber, and focused to the ion trap by the imaging objective. It is aligned at a 90° angle to the trap axis x in order to suppress coupling to the axial mode of motion. Thus, shelving efficiency is unaffected by motional excitation of the ions along the axial direction, mainly caused by shuttling. The beam is horizontally polarized and therefore couples only to $\Delta m = 0, \pm 2$ transitions [Roo00], minimizing errors due to off-resonant excitation.

397 nm for Doppler cooling and qubit initialization

Laser light for Doppler cooling and qubit initialization (see Sec. 3.2) near 396.959 nm is generated by the same diode laser[17] and split into two beams. The Pound-Drever-Hall technique is used to compensate frequency drifts of the diode laser. Each beam is controlled by a separate AOM in double-pass configuration and guided to the trap setup via a separate single-mode fiber. The laser beam for spin initialization must be circularly polarized in order to drive only the $\Delta m = +1$ transition. For this purpose, a Glan-Taylor polarizer first produces extremely pure linear polarization. Then, a $\lambda/4$-plate transforms the polarization to right circular.

866 nm & 854 nm for repumping and quenching

Two diode lasers[18] at wavelengths of 866.451 nm ("repump", see Sec. 3.2) and 854.443 nm ("quench", see Sec. 3.5) produce light for depleting the $D_{3/2}$ and $D_{5/2}$ levels of the trapped calcium ions, respectively. Frequency drifts of the repump laser are compensated via the Pound-Drever-Hall stabilization scheme. Frequency stability of the quench laser is less critical - it is merely regulated to a wavelength meter with an accuracy of about

---

[15] Matisse TX, Sirah - Lasertechnik GmbH

[16] ATFilms 6020 notched cavity, finesse $\mathcal{F} \approx 140\,000$ [Mac12]

[17] DL 100 Pro (TOPTICA Photonics)

[18] DL 100 (TOPTICA Photonics)

10 MHz[19]. Both laser beams are controlled by separate AOMs in double-pass configuration, overlapped by a polarizing beam splitter, and coupled into the same single-mode fiber. After passing through the polarizing beam splitter, the beams are orthogonally polarized to each other. Inside the trap setup, the polarizations are altered to (anti-) diagonal. This way, both $\Delta m = 0, \pm 1$ transitions are driven and all magnetic sublevels of both $D_{3/2}$ and $D_{5/2}$ states are depleted.

374 & 422 nm for photoionization

Two diode lasers at wavelengths of 374 nm[20] and 422.791 nm[21] serve to ionize calcium atoms at the trap location (see Sec. 3.1). The frequency of the laser at 422.791 nm is regulated based on the wavelength meter. Since the laser at 374 nm drives the transition to the continuum, a frequency regulation is not necessary. A mechanical shutter blocks both beams if the desired number of ions is stored inside the ion trap. The beams are overlapped by a polarizing beam splitter and coupled into the same single-mode fiber.

397 nm for stimulated Raman transitions

A total of four laser beams are used for qubit manipulation (see Secs. 3.3,3.4). The beams are directed to the ion trap at different angles, so that stimulated Raman transitions can be driven with different effective $\vec{k}$-vectors by choosing the appropriate pairs of laser beams. For the copropagating beams termed *R1* and *CC*, the effective $\vec{k}$-vector vanishes and the transition is completely decoupled from the motion of the ions. By combining the beams *R1* and *R2*, the transition couples only to the axial modes of motion with a Lamb-Dicke parameter of about $\eta \approx 0.2$. Similarly, the beams *R1* and *R4* drive transitions that couple to the radial modes of motions with $\eta \approx 0.1$. For performing two-qubit gates that couple only to the radial modes of motion without driving the qubit transition, the beams *R4* and *CC* are used.

All beams are derived from a common laser source at 396.56 nm[22], blue detuned by about $2\pi \cdot 740$ GHz from the $S_{1/2} \leftrightarrow P_{1/2}$ cycling transition. An electro-optic modulator[23] and a polarizer serve to stabilize the laser power based on a photodiode[24]-signal. The signal is fed to a regulation circuit[25] that controls the input voltage of the electro-optic modulator such that a constant laser power is maintained.

The beams are separated by polarizing beam splitters and individually controlled by AOMs[26] in single-pass configuration. Here, single-pass configurations enable a compact optical setup [Not17, Kau17a], which is crucial for maintaining relative phase stability between the laser beams. The beams *R2* and *R4* are coupled into individual fibers, and

---

[19] Wavelength Meter WSU, HighFinesse Laser and Electronic Systems

[20] free running diode, DL 100 (TOPTICA Photonics)

[21] DL 100 Pro (TOPTICA Photonics)

[22] frequency doubled diode laser, TA-SHG (TOPTICA Photonics)

[23] LINOS LM 0202 P 5W VIS

[24] Thorlabs PDA8A/M

[25] TEM Messtechnik NoiseEater 3V2 & HighVoltageAmplifier-Fast

[26] Gooch & Housego I-M110-3C10BB-3-GH27, I-M095-3C10BB-3-GH27

the beams *R1* and *CC* are jointly guided to the trap setup by the same fiber. Inside the magnetic-shielding enclosure, Glan-Taylor polarizers ensure pure linear polarization for the *R2* and *R4* beams. This leads to balanced coupling to the $\Delta m = +1$ and $\Delta m = -1$ transitions, which is crucial for avoiding differential AC Stark shifts between the qubit states [Pos10].

4.4. Magnetic-field generation

A magnetic field inside the enclosure, either generated via magnetic-field coils or permanent magnets, splits degenerate energy levels of the trapped calcium ions and provides a quantization axis. Two magnetic-field coils with an inner diameter of 75 mm and 170 windings are placed around viewports of the vacuum chamber in a coaxial geometry. The distance of each coil to the ion trap is about 155 mm. A specially designed current source[27] delivers a current of about 3.3 A to both coils with fluctuations on the order of $\Delta I/I \approx 10^{-5}$ [Mon11a, p. 33]. The current generates a magnetic field of about 0.37 mT at the ion location and splits the ground state Zeeman sublevels of the trapped calcium ions by about $2\pi \cdot 10$ MHz. A total voltage of 4.3 V is required to supply both coils in series. Under operation, the coils dissipate about 15 W of heat inside the magnetic-shielding enclosure.

As part of this work, generation of the quantizing field by permanent magnets was investigated. A magnetic field of similar magnitude can be created by 80 individual Sm_2Co_{17} cylindrical magnets with 6 mm diameter and 4 mm length[28], see Fig. 4.2. This material combines a high remanence of about 1 T with a low temperature dependence of about -0.03 %/K. Remanence describes the magnetization of ferromagnetic materials at zero external field after they have been magnetized to saturation. The magnets are glued at constant spacing into two round aluminum frames with an inner diameter of 108 mm and an outer diameter of 128 mm. The two frames are directly mounted around the magnetic-field coils. An advantage of the permanent magnets with respect to the coils is that no heat is dissipated inside the magnetic-shielding enclosure. This leads to a greatly improved stability of the laser-focusing optics.

Figure 4.5 illustrates the magnetic field generated by (a) the permanent magnets and (b) the coils. The permanent magnets have been modeled as magnetic dipoles with a dipole moment $\mu = B_\mathrm{R} V/\mu_0$ resulting from the magnets' volume V, the remanence of about $B_\mathrm{R} = 1$ T, and the vacuum permeability μ_0. For the coils, each wire has been described as a circular current loop. The main difference in the field distribution is that for the permanent magnets, the field direction switches signs along the symmetry axis given by the center of both Aluminum rings.

The different field geometries have consequences on the field homogeneity at the trap position: For the permanent magnets, the optimal ring radius for best homogeneity is $R_\mathrm{ring} \approx 0.29\, d$ instead of $R_\mathrm{coil} = d$ in the case of coils, with d the distance between the

---

[27] Design from Prof. Rainer Blatt's group, University of Innsbruck, supplied by an Agilent E3633A power supply in voltage control mode

[28] DeltaMagnet DE64, IBS Magnet, Berlin, Germany

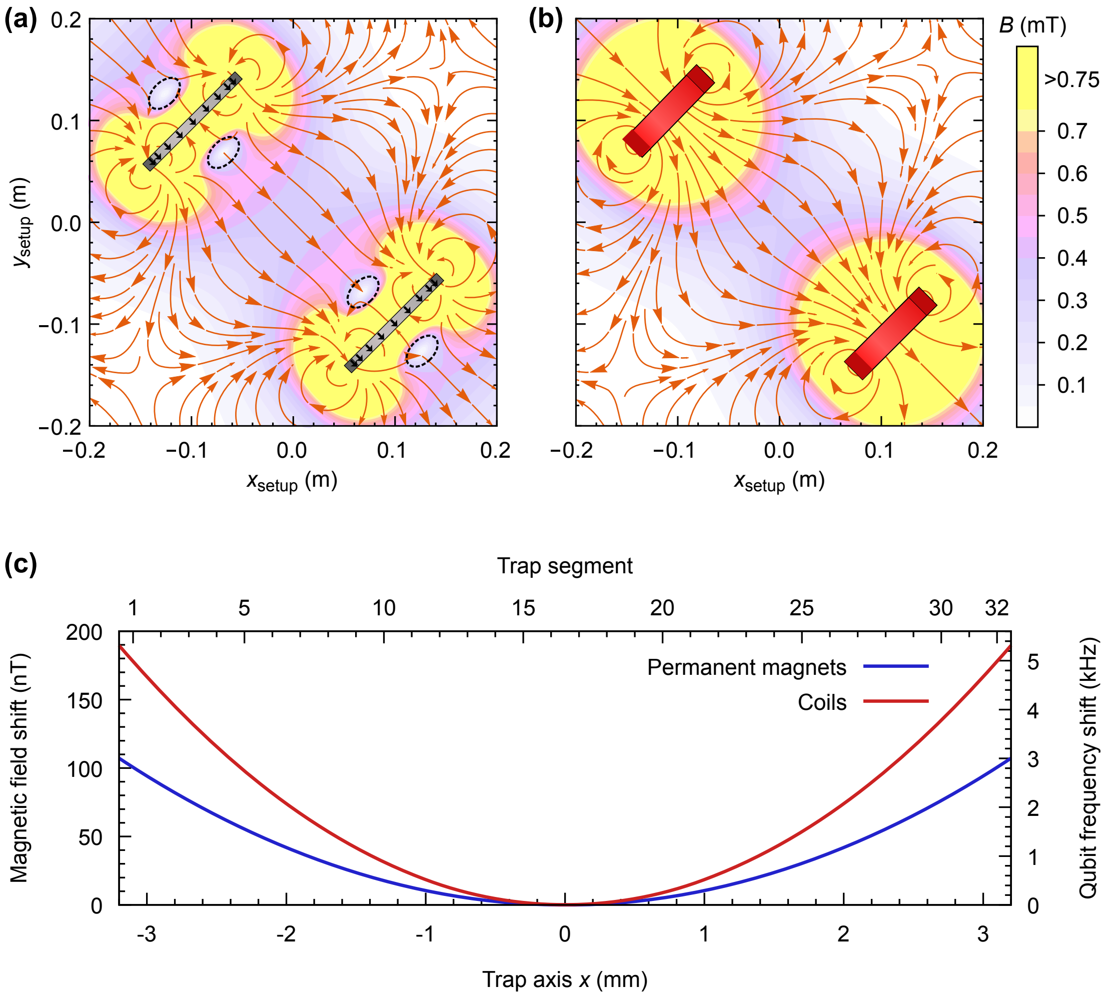

Figure 4.5.: Simulated magnetic field generated from **(a)** permanent-magnet rings and **(b)** coils. A cross section along the plane given by $z_{\text{setup}} = 0$ is shown, and coordinates are given relative to the ion trap center. Arrows and shaded areas depict the field direction and strength, respectively. In **(a)**, black arrows indicate the directions of the magnetic dipoles, and black dashed ellipses indicate regions in which the magnetic field approaches zero. **(c)** Calculated magnetic-field shift along the trap axis x relative to the trap center in the case of permanent magnets (blue curve) and coils (red curve). A qubit frequency shift of 3 kHz corresponds to a relative frequency shift of about 0.03%.

rings. The latter relation is also known as *Helmholtz configuration*, and would maintain homogeneity over a larger range as compared to the permanent-magnet configuration. However, in our ion-trap setup, the radius of the coils and magnet rings is limited by space constraints. In this case, the permanent magnets exhibit a slightly better field homogeneity along the trap axis (Fig. 4.5(c)). Due to the inhomogeneous magnetic field, spins stored at different trap locations rotate with slightly different Larmor frequencies and the qubits accumulate additional phases throughout shuttling operations, which have to be taken into account in quantum algorithms with multiple ions [Kau17c].

The field simulations in Fig. 4.5 do not take variations of the individual magnets' remanescences, magnetic interactions among the magnets, experimental alignment imperfections, and magnetization of the vacuum chamber into account. These effects lead to a spatial variation of the quantization field that differs from the simulation results. The field variation along the trap axis is characterized by measuring the Zeeman splitting at different locations [Wal11]. Initial measurements had revealed a parabolic variation of the magnetic field, where the minimum of the parabola was located outside of accessible trap volume. To shift the minimum into the accessible trap volume, eight additional magnets have been placed uniformly distributed along one of the aluminum frames. Finally, one aluminum frame has been slightly moved such that the minimum coincides with the laser interaction region, where laser-driven gates are carried out and a magnetic-field gradient would represent an error source.

4.5. Experimental control system

Typical experiments require fast switching of laser beams on a microseconds to milliseconds timescale, dynamic control of trap voltages, ion-fluorescence detection, and many more tasks that have to be synchronized with each other. These tasks are handled by multiple devices in the laboratory that are connected to a personal computer. The computer runs a C++ program that creates the necessary data for controlling the hardware and evaluates the measurement results received from the EMCCD camera or the PMT. Figure 4.6 sketches the most important devices required for dynamic control of the experiment and how they communicate with each other.

Time-dependent voltages for the DC trap segments are generated by a custom-made FPGA-based arbitrary waveform generator. It supplies all trap electrodes with voltages in the range of ±40 V with a resolution of about 1.2 mV and a maximum update rate of 2.5 MSamples/s. Second-order Π-type low-pass filters with a cutoff frequency of about 50 kHz for each trap electrode suppress electrical noise. For the ion-crystal-separation experiments presented in chapter 5, an earlier version of the device has been used where the voltage range is limited to ±10 V. The arbitrary waveform generator also features 24 digital outputs with an update rate of 50 MSamples/s, synchronized with the voltage outputs. The digital outputs are used for switching laser beams and triggering other time-critical tasks, such as data acquisition of the EMCCD camera and the PMT, and the output of a programmable frequency generator[29].

---

[29] Versatile frequency generator VFG-150, TOPTICA Photonics

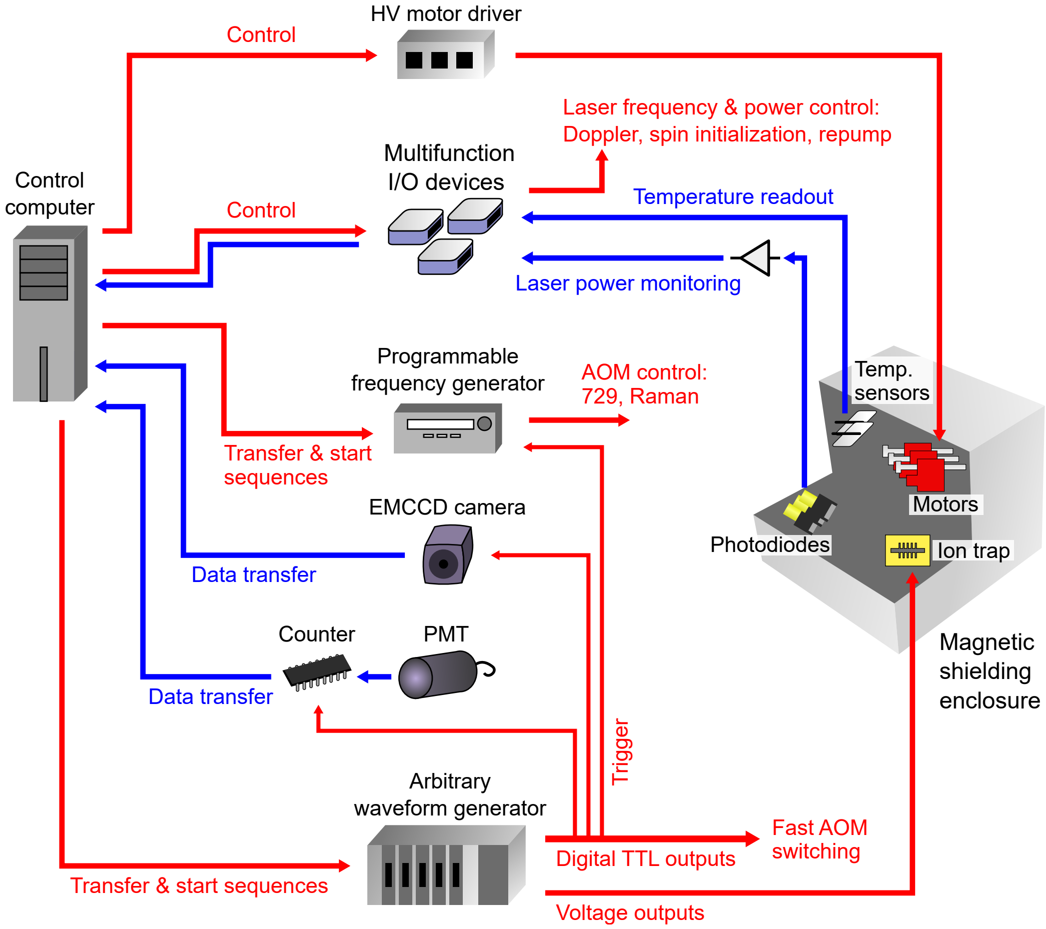

Figure 4.6.: Relevant devices in the laboratory for dynamic control of experiments and monitoring of parameters inside the magnetic-shielding enclosure. Red arrows indicate data that has to be transferred from the control computer to the experiment and blue arrows indicate measured data that is transferred to the computer for evaluation.

The programmable frequency generator outputs an RF signal that drives AOMs for coherent operations on the qubit levels and the quadrupole transition near 729 nm. The frequency, amplitude, and phase of the output signal can be freely modified in steps of 5 ns. Since stimulated Raman transitions require two laser beams, a static frequency generator[30] additionally supplies a second AOM and also serves as a phase reference for the programmable frequency generator. Radio-frequency switches[31] guide the RF signals of both frequency generators to the desired AOMs. The AOMs that control the laser

---

[30] Rohde & Schwarz SML01

[31] Mini-Circuits ZYSW-2-50DR

beams for Doppler cooling, spin initialization and repumping are supplied by voltage controlled oscillators[32] and fast switching is enabled by RF switches in a similar fashion.

Temperature sensors and photodiodes for measuring laser powers inside the magnetic-shielding enclosure are monitored by the control computer via multifunction I/O devices[33]. These also control the frequency and intensity of the laser beams for Doppler cooling, spin initialization, and repumping. Laser alignment on the ion trap can be controlled from the computer via motorized optical mounts.

In order to minimize the amount of data transferred between the control computer and the laboratory devices, the arbitrary waveform generator allows for repeating experimental sequences N times, with N typically ranging from 50 to 300 depending on the desired error bar. After all repetitions have been completed, the measured data from the EMCCD camera or PMT is transferred to the computer and evaluated.

---

[32] Mini-Circuits ZOS-150

[33] National Instruments USB-6000 & USB-6008

5 Separation of ion crystals

Ion-crystal separation is not only an essential building block for scalable quantum-information experiments in segmented ion traps, but also a key ingredient for the magnetometer presented in chapter 7. It is desired to perform the procedure as fast as possible, while keeping the excitation of the ions' motion at a minimum.

In this chapter, a separation protocol following the guidelines by Kaufmann et al. [Kau14] is experimentally realized. A two-ion crystal, initially stored at the *center* segment C (Fig. 5.1), is to be split into two ions trapped in separate potential wells at the neighboring *split* segments S. The center segment coincides with the laser interaction zone of the ion trap to ease calibration measurements. The *outer* segments O serve to null a possible background force along the trap axis and provide additional axial confinement during the separation procedure.

The main experimental difficulty is that the harmonic confinement transiently vanishes during the process. At this *critical point*, the ions are susceptible to energy-increase mechanisms, i.e., oscillatory excitation and motional heating. In order to control these effects, we need to accurately predict the behavior of the ions by precisely calibrating the parameters of the electrostatic trap potential (Sec. 5.1). This enables us to tune the

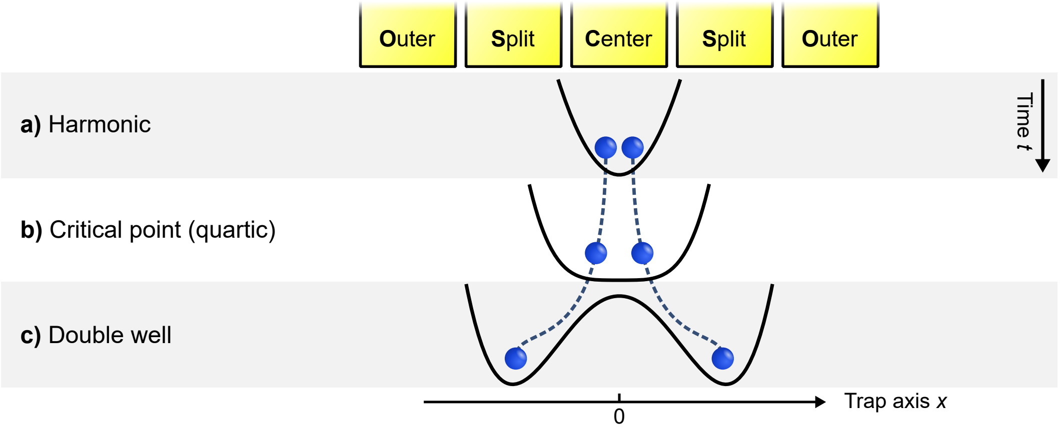

Figure 5.1.: Sketch of the ion-crystal separation procedure. An initial harmonic potential is transformed to a double-well potential in order to separate a two-ion crystal stored at the center segment. The harmonic confinement transiently vanishes at the critical point. The DC voltages of the center, split, and outer segments are modified during the process.

ions' velocity and acceleration at the critical point by creating suitable voltage ramps (Sec. 5.2). The energy increase depends strongly on the trap frequency and the heating rate close to the critical point, which are characterized in Sec. 5.3. Finally, measurements of the energy increase are presented in Sec. 5.4. Since the separation takes place along the trap axis x, we only consider the axial motion of the ions.

5.1. Trap characterization

We parametrize the electrostatic potential along the trap axis x by a Taylor approximation around the initial center-of-mass position at the center segment [Hom06]

$$V(x,t) \approx \beta(t)\, x^4 + \alpha(t)\, x^2 + \gamma(t)\, x. \tag{5.1}$$

This approximation holds for ion distances much smaller than the width of a trap segment. In the following, we omit explicit time dependencies to keep the notation uncluttered. The coefficients depend on the time-dependent electrode voltages U_i with $i = \{\mathrm{C}, \mathrm{S}, \mathrm{O}\}$ and the trap geometry:

$$\alpha = U_\mathrm{C}\alpha_\mathrm{C} + U_\mathrm{S}\alpha_\mathrm{S} + U_\mathrm{O}\alpha_\mathrm{O} + \alpha' \tag{5.2}$$
$$\beta = U_\mathrm{C}\beta_\mathrm{C} + U_\mathrm{S}\beta_\mathrm{S} + U_\mathrm{O}\beta_\mathrm{O} + \beta' \tag{5.3}$$
$$\gamma = \Delta U_\mathrm{S}\gamma_\mathrm{S} + \Delta U_\mathrm{O}\gamma_\mathrm{O} + \gamma'. \tag{5.4}$$

The voltage U_S (U_O) is applied to both S (O) electrodes, while the voltage ΔU_S (ΔU_O) is a differential voltage between the electrodes comprising the respective pair. The constant coefficients $\alpha_i, \beta_i, \gamma_i$ are determined by the second, fourth, and first derivatives of the respective electrode potentials at $x = 0$. Experimental imperfections are characterized by offset coefficients α', β', γ'. Such contributions arise from stray charges, residual ponderomotive forces, and asymmetries in the trap geometry. The values for the geometry coefficients could be in principle obtained by electrostatic simulations of the ion trap [Sin10]. However, simulations of the employed trap deviate substantially from the experimental values, so that the required degree of control for separation is not achieved.

The initial situation is characterized by predominantly harmonic confinement $\alpha \gg 0$. Separation of the two-ion crystal is performed by sweeping α from a positive to a negative value, transforming a single-well potential at the center segment to a double-well potential at the split segments. At the critical point (CP) $\alpha = 0$, the axial confinement is at its minimum strength, while the rate of change of the equilibrium ion distance attains its maximum. This corresponds to a strong impulsive drag, possibly leading to oscillatory excitation of up 10^6 phonons [Kau14]. Thus, the voltage ramps need to be designed such that α varies slowly near the critical point, which in turn requires precise knowledge of the coefficients α_i from Eq. 5.2.

Harmonic coefficients

For calibrating the α_i-parameters, we determine the squared axial trap frequency

$$\omega_x^2 = 2e\alpha/m = 2\frac{e}{m}\left(U_\mathrm{C}\alpha_\mathrm{C} + U_\mathrm{S}\alpha_\mathrm{S} + U_\mathrm{O}\alpha_\mathrm{O} + \alpha'\right) \tag{5.5}$$

by applying resolved sideband spectroscopy on the stimulated Raman transition between the spin states of a single trapped ion. Resolved sideband spectroscopy is carried out by measuring the spin-flip probability for varying AOM frequencies of the Raman R1 laser beam, while keeping the frequency of the Raman R2 beam constant [Pos09]. The axial trap frequency is determined by the difference frequency between the blue sideband and the carrier transition. The segment voltages are ramped to a desired voltage configuration just before the spectroscopy laser pulse and restored to the initial configuration after the spectroscopy pulse has been applied.

For determining α_C and α', the axial trap frequency for varying U_C is measured while keeping the other voltages at zero. Similarly, α_S (α_O) is determined by setting different values for U_S (U_O) while keeping U_C constant. The α_i-coefficients are then obtained by performing linear regression of the squared trap frequencies versus the corresponding voltage. This procedure allows for measuring all α_i-parameters, including the imperfection α', with sub-percent accuracy.

Figure 5.2 shows an example measurement in the V1 trap. The coefficients and the expected values from the trap simulation[1] are

$$\alpha_\mathrm{C} = -2.626(3)\cdot 10^6\ \mathrm{m}^{-2} \qquad \alpha_\mathrm{C}^{(\mathrm{sim})} = -3.034\cdot 10^6\ \mathrm{m}^{-2} \tag{5.6}$$

$$\alpha_\mathrm{S} = +1.278(3)\cdot 10^6\ \mathrm{m}^{-2} \qquad \alpha_\mathrm{S}^{(\mathrm{sim})} = +1.715\cdot 10^6\ \mathrm{m}^{-2} \tag{5.7}$$

$$\alpha_\mathrm{O} = +0.991(6)\cdot 10^6\ \mathrm{m}^{-2} \qquad \alpha_\mathrm{O}^{(\mathrm{sim})} = +1.016\cdot 10^6\ \mathrm{m}^{-2}. \tag{5.8}$$

For the offset parameter α', a drift from about $-1\cdot 10^6\,\mathrm{Vm}^{-2}$ to about $-4\cdot 10^6\,\mathrm{Vm}^{-2}$ within 6 weeks has been observed. This corresponds to a spurious voltage of about +0.4 V to +2 V on the center segment. During this time, the coefficients α_i remained constant on a sub-percent level.

In the V2 trap, the coefficients[2] are

$$\alpha_\mathrm{C} = -3.020(1)\cdot 10^6\ \mathrm{m}^{-2} \qquad \alpha_\mathrm{C}^{(\mathrm{sim})} = -3.122\cdot 10^6\ \mathrm{m}^{-2} \tag{5.9}$$

$$\alpha_\mathrm{S} = +1.244(1)\cdot 10^6\ \mathrm{m}^{-2} \qquad \alpha_\mathrm{S}^{(\mathrm{sim})} = +1.361\cdot 10^6\ \mathrm{m}^{-2} \tag{5.10}$$

$$\alpha_\mathrm{O} = +1.262(1)\cdot 10^6\ \mathrm{m}^{-2} \qquad \alpha_\mathrm{O}^{(\mathrm{sim})} = +1.283\cdot 10^6\ \mathrm{m}^{-2} \tag{5.11}$$

$$\alpha' = -0.36(4)\cdot 10^6\ \mathrm{V\ m}^{-2} \qquad \alpha'^{(\mathrm{sim})} = 0. \tag{5.12}$$

Compared to the V1 trap, all parameters are considerably closer to the simulated results and remained constant within the given level of accuracy for several weeks.

---

[1] Simulations for the V1 trap were carried out by Claudia Warschburger using the scheme presented by Singer et al. [Sin10]

[2] Simulations for the V2 trap were carried out by Henning Kaufmann using the scheme presented by Singer et al. [Sin10]

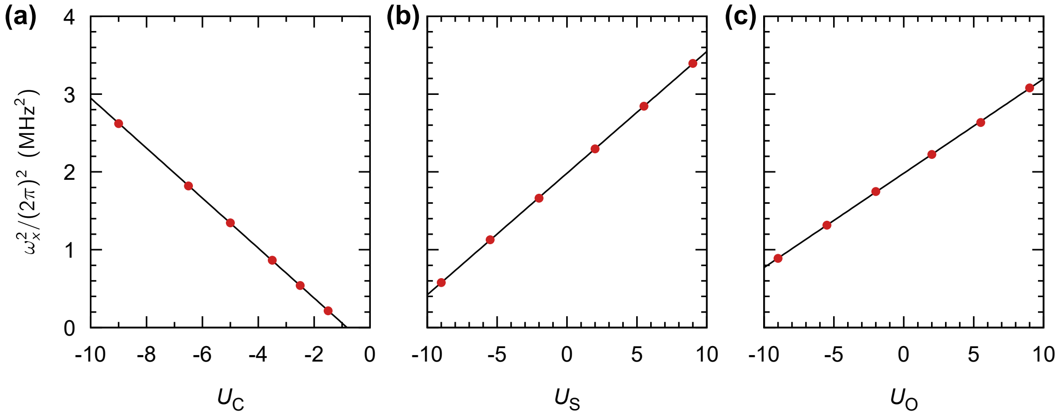

Figure 5.2.: Example measurement for determining the α_i-coefficients. A linear regression (black line) to the squared axial trap frequencies versus the voltages **(a)** U_C, **(b)** U_S, and **(c)** U_O is performed. The slopes are proportional to the respective coefficients $\alpha_{\mathrm{C,S,O}}$, and the offset in **(a)** is proportional to α'.

Quartic coefficients

The values for the parameters β_i are calibrated by measuring ion distances in a purely quartic potential: The calibrated α_i-values are used to apply voltage sets to the segments that correspond to $\alpha = 0$. The ion distance is then given by [Kau14]

$$d_{\mathrm{eq}}^{(\mathrm{CP})} = \left(\frac{2e}{4\pi\varepsilon_0\beta}\right)^{1/5}. \tag{5.13}$$

Thus, a measurement of the ion distance on the EMCCD camera (see Appendix A) reveals β, and a linear fit to the measurement results for varying voltage sets yields the segment coefficients β_i. For 22 different voltage configurations, the ion distances at the critical point vary between 25 µm and 55 µm. In the V1 trap, the coefficients are

$$\beta_\mathrm{C} = +3.1(1)\cdot 10^{13}\ \mathrm{m}^{-4} \qquad \beta_\mathrm{C}^{(\mathrm{sim})} = +2.708\cdot 10^{13}\ \mathrm{m}^{-4} \tag{5.14}$$

$$\beta_\mathrm{S} = -0.62(3)\cdot 10^{13}\ \mathrm{m}^{-4} \qquad \beta_\mathrm{S}^{(\mathrm{sim})} = -3.048\cdot 10^{13}\ \mathrm{m}^{-4} \tag{5.15}$$

$$\beta_\mathrm{O}^{(\mathrm{sim})} = +0.224\cdot 10^{13}\ \mathrm{m}^{-4} \tag{5.16}$$

$$\beta' = +15(1)\cdot 10^{13}\ \mathrm{m}^{-4} \qquad \beta'^{(\mathrm{sim})} = 0. \tag{5.17}$$

Due to the small feed-through of the outer segments, no value for β_O could be determined with this method. The large offset parameter indicates the presence of strongly inhomogeneous static background fields, and even dramatically improves the confinement at the critical point.

In the V2 trap, the ion distances at the critical point are found to match the simulation within the accuracy of the ion-position measurements. We thus refrain from doing experimental calibrations and instead directly use the simulated coefficients

$$\beta_{\mathrm{C}}^{(\mathrm{sim})} = +3.352 \cdot 10^{13}\ \mathrm{m}^{-4} \tag{5.18}$$

$$\beta_{\mathrm{S}}^{(\mathrm{sim})} = -3.683 \cdot 10^{13}\ \mathrm{m}^{-4} \tag{5.19}$$

$$\beta_{\mathrm{O}}^{(\mathrm{sim})} = +0.155 \cdot 10^{13}\ \mathrm{m}^{-4} \tag{5.20}$$

$$\beta'^{(\mathrm{sim})} = 0. \tag{5.21}$$

Potential tilt

A residual electric field γ' along the trap axis breaks the symmetry of the electrostatic potential. It can be sufficiently strong to tilt the potential at the critical point such that the ions are not separated, but rather stay confined in one of the potential wells. This asymmetry is canceled in the experiment by applying an appropriate compensation voltage ΔU_{O}. The separation procedure succeeds within the window of compensation voltages $\Delta U_{\mathrm{O}}^{(l)} \leq \Delta U_{\mathrm{O}} \leq \Delta U_{\mathrm{O}}^{(u)}$, and the window center $(\Delta U_{\mathrm{O}}^{(l)} + \Delta U_{\mathrm{O}}^{(u)})/2$ roughly corresponds to a canceled background field $\gamma = 0$. The compensation voltage ΔU_{O} is experimentally set to the window center by monitoring slowly separating ions on the EMCCD camera, and adjusting ΔU_{O} such that the center-of-mass of both ions is constant during the process [Ebl10]. The half width $\delta U_{\mathrm{O}} = \left(\Delta U_{\mathrm{O}}^{(u)} - \Delta U_{\mathrm{O}}^{(l)}\right)/2$ is about 16 mV, corresponding to a force on a single ion at $x = 0$ of only about 800 zepto Newton. The accuracy for compensating the potential tilt is limited by the resolution at which the segment voltages can be set and the electric feed-through of the segments used for the compensation. In our case, the voltage resolution is 0.3 mV, leading to a tilt field resolution of about 0.1 V/m or a force resolution of 15 zeptoN. In [Kau14], it is shown that merely compensating to values within the window where the separation succeeds is not sufficient, as nonzero tilt fields can lead to strongly increased motional excitation due to quasi-discontinuous trajectories of the equilibrium positions. It is therefore crucial not only to calibrate the compensation voltage ΔU_{O} accurately, but also to compensate for temporal drifts of the tilt field.

Drifts of the trap parameters can be caused by laser induced charging of the trap surface [Har10, Wan11] acting on short (minutes) timescales, or by thermally activated surface processes on long timescales (hours). The most substantial impact on tilt-field drifts is caused by the photoionization laser beams at 423 nm and 374 nm. These either charge the trap directly via the photoelectric effect, or indirectly if ions created near the trap are accelerated onto trap surfaces by the RF electric field [Här14]. Since it is necessary to reload ions at intervals ranging roughly between 10 minutes and 1 hour, the drifts caused by photoionization are too large to maintain good separation results. The charging rates are observed to be fluctuating and to be extremely sensitive on the beam alignment. This problem is mitigated by adjusting the photoionization beams to a *loading zone* 5 segments away from the center segment, so that charging takes place

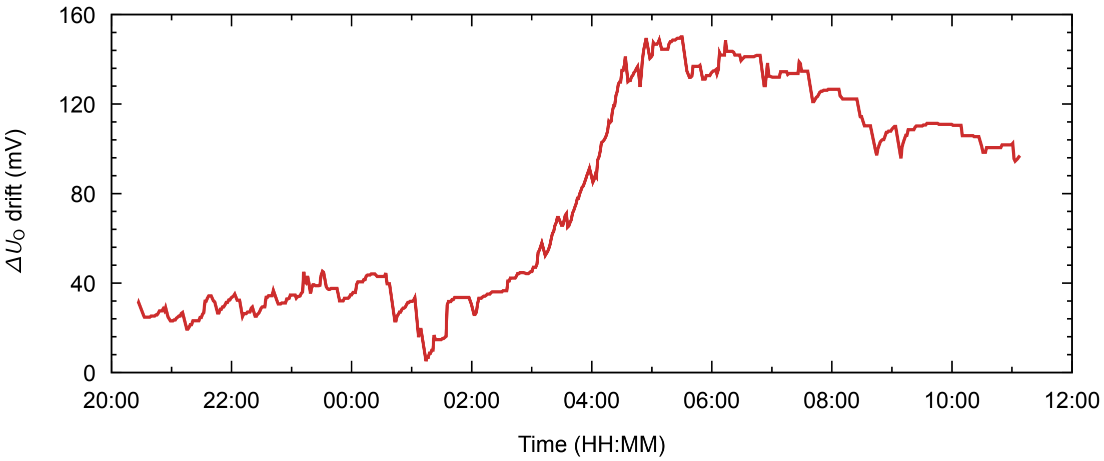

Figure 5.3.: Long-term drift of the tilt-compensation voltage ΔU_{O} caused by photoionization at a remote segment and superimposed thermal processes. The data was measured with laser powers of about 1 mW for the laser at 422 nm, and about 300 µW for the laser at 374 nm.

at a distant location. A remote-loading procedure is realized by periodically shuttling a confining axial potential well from the loading zone to the center segment within 160 µs.

Figure 5.3 shows a long-term record of ΔU_{O}. A total drift of more than 100 mV occurred during a night, significantly exceeding the precision required for working separation. Frequent tilt recalibration is thus inevitable despite the remote-loading procedure.

The improvements made in the V2 trap have considerably decreased the drift rates. This eliminates the need for the remote-loading procedure, and enables the usage of higher laser powers for photoionization. During typical operation of the experimental apparatus, the tilt-compensation voltage ΔU_{O} remains constant on a 2 mV level for several weeks. Hence, frequent tilt recalibration is no longer necessary in the V2 trap.

5.2. Voltage ramp design

The voltage ramps $\{U(t)\} = \{U_{\mathrm{C}}(t), U_{\mathrm{S}}(t), U_{\mathrm{O}}(t)\}$ are designed in a two-step scheme. Since the harmonic coefficient α is monotonically decreasing throughout the separation process, we can define voltage sets $\{U(\alpha)\}$ as a function of α. We first specify the voltages U_{S} and U_{O} at the start, at the critical point, and at the end of the separation process, and linearly interpolate between these values. The voltage U_{C} is then obtained for each α by using Eq. 5.2 and the measured trap calibration data:

$$U_{\mathrm{C}}(\alpha) = \frac{1}{\alpha_{\mathrm{C}}} \left(\alpha - \alpha' - \alpha_{\mathrm{O}} U_{\mathrm{O}}(\alpha) - \alpha_{\mathrm{S}} U_{\mathrm{S}}(\alpha)\right) \tag{5.22}$$

The initial voltage set $\{U^{(\mathrm{i})}\} = \{-7V, 0V, 0V\}$ gives rise to an harmonic potential with an axial trap frequency of about $\omega_x \approx 2\pi \cdot 1.4$ MHz. The voltage set at the critical point $\{U^{(\mathrm{CP})}\} \approx \{-1.89V, -7.5V, +9V\}$ creates a purely quartic potential with a high

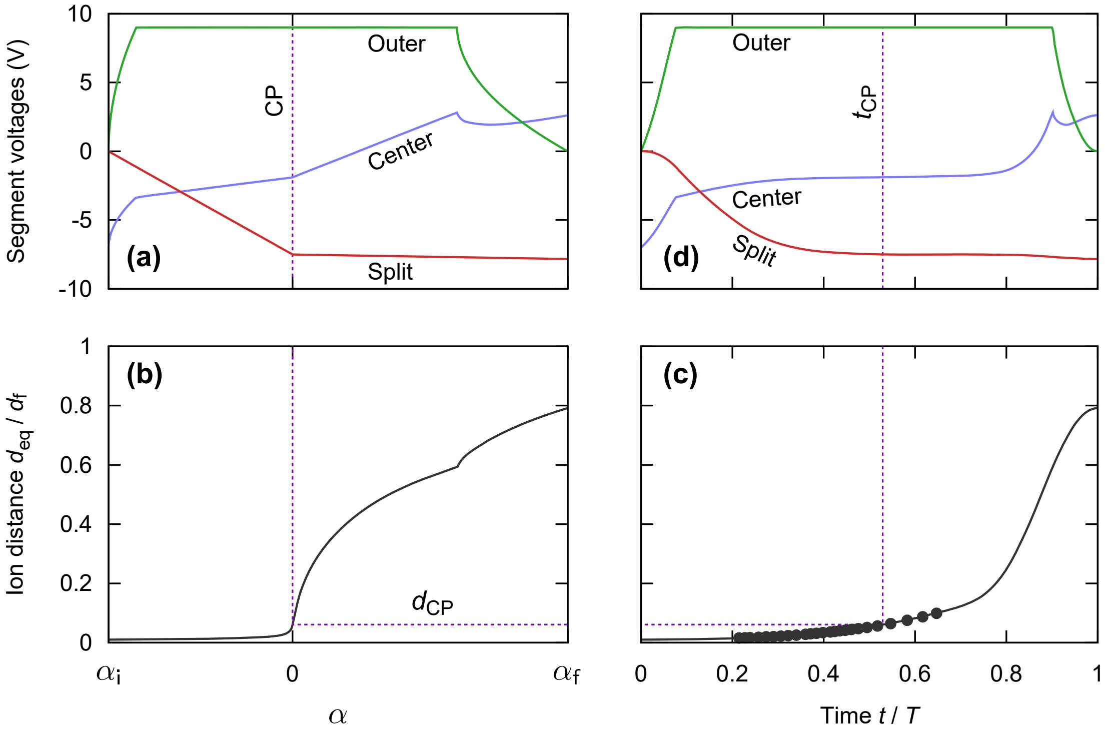

Figure 5.4.: Voltage ramp generation. **(a)** Voltage sets as a function of α. The initial and final values α_i and α_f correspond to the respective voltage sets $\{U^{(\mathrm{i})}\}$ and $\{U^{(\mathrm{f})}\}$ (see text). **(b)** Calculated equilibrium distance between both ions using the voltage sets from (a). The final distance d_f is not reached in the calculation, because the Taylor approximation $V(x,t)$ (Eq. 5.1) breaks down for ion distances $d_\mathrm{eq} \gg d_\mathrm{CP}$. **(c)** Desired equilibrium distance d_eq versus time as given by Eq. 5.23 and the truncation procedure (see text). The final distance is chosen according the range in (b). The dots indicate distance measurements with an EMCCD camera. **(d)** Variation of the segment voltages versus time. The critical point is indicated by a dashed line. Note the small variation of the voltages around the critical point.

β-coefficient, leading to a minimum axial frequency of about $\omega_{x,\mathrm{crit}} \approx 2\pi \cdot 170$ kHz. The final voltage configuration $\{U^{(\mathrm{f})}\} = \{+2.62V, -7.83V, 0V\}$ leads to separate harmonic potentials at the split segments, where the axial trap frequencies match the initial one. A more refined scheme ramps U_O faster near the initial and final steps, so that U_O is constant around the critical point (Fig. 5.4(a)).

Based on the voltage ramps $\{U(\alpha)\}$, we can now calculate the equilibrium distance between both ions $d_\mathrm{eq}(\alpha)$ during the process. This is implemented by numerically minimizing the electrostatic potential $V(x)$ using the calibrated α and β coefficients, and by including the Coulomb repulsion between both ions. The result is depicted in Fig. 5.4(b). The ions are strongly accelerated near the critical point, which in combination with the low axial trap frequency would lead to large motional excitation [Kau14].

We therefore desire to calculate time-dependent voltage ramps $\{U(t)\}$ that accelerate the ions slowly near the critical point. First, we define a trajectory that provides a sufficiently small acceleration at the critical point for separation times of about 100 µs:

$$d_{\mathrm{eq}}(t) = d_{\mathrm{i}} + (d_{\mathrm{f}} - d_{\mathrm{i}}) \left(\frac{t}{T}\right)^2 \sin^2\left(\frac{\pi}{2}\frac{t}{T}\right) , \qquad t \in [0, T] \tag{5.23}$$

with the respective initial and final distances d_{i} and d_{f}, and the total separation duration T. We further optimize the trajectory by truncating the initial 10% and final 30% of T by rescaling while leaving the voltages near the critical point fixed. Test measurements in the experiment verified that this does not affect the resulting motional excitations significantly, but allows for reducing the duration of the separation process. The trajectory is depicted in Fig. 5.4(c).

We finally calculate time-dependent voltages $\{U(t)\}$ by (i) determining $d_{\mathrm{eq}}(t)$ for a given time t from Eq. 5.23, (ii) finding the value of α for this distance, and (iii) looking up the voltages for this α value from the linearly interpolated ramps:

$$\{U(t)\} : t \xrightarrow{(i)} d_{\mathrm{eq}}(t) \xrightarrow{(ii)} \alpha(d_{\mathrm{eq}}(t)) \xrightarrow{(iii)} \{U(\alpha(d_{\mathrm{eq}}(t)))\} \tag{5.24}$$

The voltage ramps calculated with this scheme exhibit small variation rates around the critical point (see Fig. 5.4(d)). The performance of this scheme in the experiment relies on the ability to accurately predict the ion distance near the critical point. This is checked by measuring the ion distance with the EMCCD camera for various voltage sets during the separation procedure. Figure 5.4(c) shows the measurement results. For the accessible range of distances of up to roughly $2 \cdot d_{\mathrm{CP}}$, the measured data agrees with the expected trajectory within about 2 µm.

For fine-tuning the trajectory near the critical point and for possible compensation of errors in the calibration measurements and distortions from the low-pass filters, an additional voltage offset $\delta U_{\mathrm{C}}^{(\mathrm{CP})}$ is added to the center segment near the critical point.

5.3. Time-dependent trap frequency and heating rate

The main experimental difficulty in implementing the separation procedure is the weakening of the axial confinement when the critical point is approached. We therefore characterize the axial confinement during the process via measurements of the axial trap frequency. The experimental procedure is similar to the measurements of the harmonic coefficients in Sec. 5.1. Here, two ions are dynamically separated up to a fixed distance $d \leq d_{\mathrm{CP}}$ corresponding to a fraction of the total separation duration T. This is followed by the application of a spectroscopy pulse on the quadrupole transition, and moving the ions back to the initial distance before fluorescence readout. During the separation procedure, the lasers for Doppler cooling are disabled to ensure that the determination of the trap frequency is not hampered by insufficient Doppler cooling at low trap frequencies [Pou12]. The trap frequency measured this way is a *local* trap frequency given

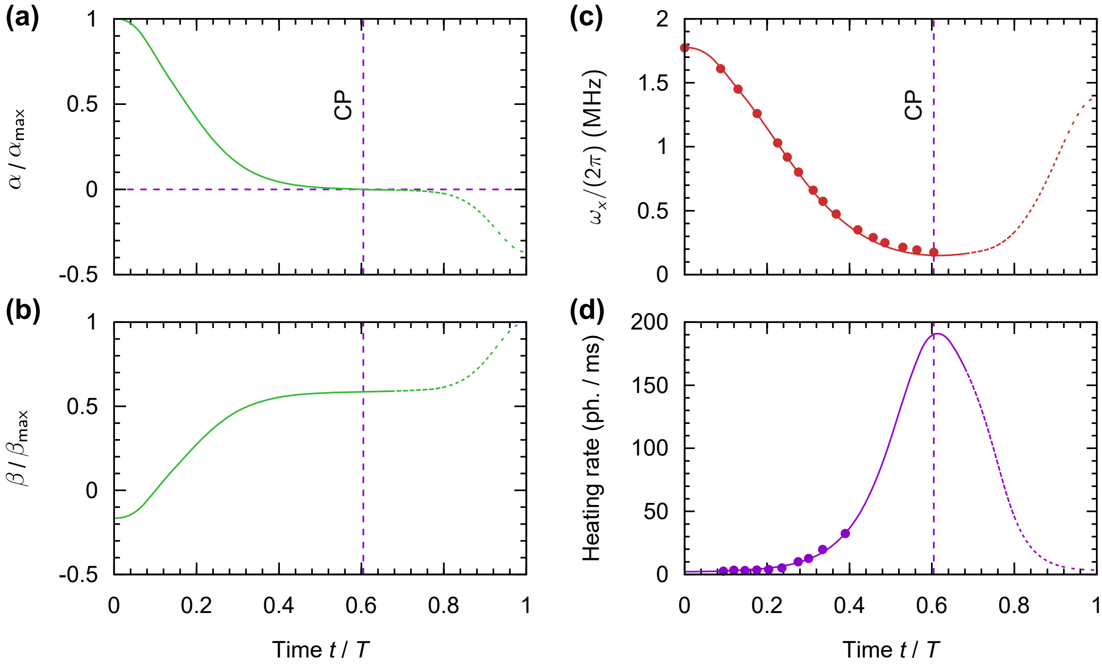

Figure 5.5.: Time-dependent trap frequency and heating rate. **(a)** and **(b)** show the variation of the respective harmonic (α) and quartic coefficients (β), as obtained from the trap calibration data and voltage ramps. The quantities beyond the critical point are shown as dashed lines, because the Taylor approximation $V(x,t)$ (Eq. 5.1) breaks down. **(c)** shows the trap frequency of the center-of-mass mode as calculated from Eq. 5.25 (solid line), along with measurement data (dots). The minimum trap frequency is $\omega_{\mathrm{CP}} \approx 2\pi \cdot 174(10)$ kHz. **(d)** shows the estimated heating rate, determined from a power law between heating rate and trap frequency (solid line). The power law has been inferred from a fit to measurement data (dots).

by the second derivative of the external potential at the position of each ion. It is given by [Hom06]:

$$\omega_x^2(t) = \frac{q}{m}\left(3\beta(t)d(t)^2 + 2\alpha(t)\right). \tag{5.25}$$

This corresponds to the trap frequency of the center-of-mass mode in the limit where the ions are confined in a common strongly harmonic potential well. The coefficients α, β are calculated from the voltage ramps in conjunction with the trap calibration data. The measurement results are shown in Fig. 5.5, and match well to Eq. 5.25[3]. The trap frequency at the critical point is substantially reduced to about 10% of the initial trap frequency. This leads to strongly increased heating rates [Niz12].

The dependency of the heating rate on the trap frequency is determined by ramping up the trap voltage (reducing its absolute value) at the center segment for a single ground-state cooled ion. The ion is kept at this lowered confinement for a given wait time

---

[3] Note that, compared to the other results in this thesis, slightly different voltage ramps were used for the data shown in Fig. 5.5, where the outer electrodes were constantly kept at the maximum voltage.

before raising the confinement to the initial value again and probing the energy increase via measurements of Rabi oscillations, as presented in Sec. 2.2. A linear regression of the energy increase versus wait time yields the heating rate at the trap frequency corresponding to a given voltage on the center segment. This way, we determine a phonon increase rate of $\Gamma(\omega) = 174(28) \cdot \omega^{-1.8(1)}\ \mathrm{ms}^{-1}$. An estimate of the total thermal energy gain during the separation is obtained by integrating over the heating rate, which is time-dependent via the time-dependent trap frequency, i.e. the area below the heating-rate curve in Fig. 5.5(d). As a result, we expect a thermal energy gain of $29(7)\ \mathrm{ms}^{-1} \cdot T$ phonons per ion at a separation duration T.

The results shown in Fig. 5.5 in conjunction with Eq. 5.25 can also be used for excluding that a significant amount of squeezing excitation occurs during separation. *Squeezing* describes the phenomenon that the wave function of an harmonic oscillator is modified such that the position uncertainty is reduced at the cost of an increased momentum uncertainty or vice versa, and might occur during rapid changes of the trap frequency. The occurrence of squeezing is governed by the adiabaticity parameter $|\dot{\omega_x}|/\omega_x^2$ [Che10, Bow12]. A conservative estimate for its upper bound is obtained from Eq. 5.25 by considering the distance increase rate and trap frequency at the critical point:

$$\frac{|\dot{\omega_x}|}{\omega_x^2} \lesssim 3 \frac{q}{m} \frac{\beta d \dot{d}}{\omega_x^3} \bigg|_{\mathrm{CP}} . \tag{5.26}$$

For the parameter regime of this work, it is $|\dot{\omega}|/\omega^2 < 0.07$. Significant squeezing excitation can therefore safely be excluded.

5.4. Characterization of motional excitation

The experimental procedure for characterizing the motional state of the ions starts with Doppler cooling a two-ion crystal on the center segment, followed by sideband cooling of both axial modes close to the motional ground state. Mean phonon numbers of $\bar{n}_{\mathrm{COM}} \approx 0.7$ on the center-of-mass mode and $\bar{n}_{\mathrm{STR}} \approx 0.7$ on the stretch mode are attained after sideband cooling. After initializing both ions to the state $|\uparrow\rangle$, a sequence of separation and transport operations is executed (Fig. 5.6). First, the crystal is separated so that both ions move to the respective split segments. One ion is then transported further away to the neighboring outer segment and kept there. After that, the second ion is transported back to the center segment. The voltage ramps are chosen such that an axial trap frequency of about $2\pi \cdot 1.4$ MHz is attained during and after the transports. It has been verified that both transports, with a duration of 24 µs each, do not significantly contribute to the total energy gain during the process. The motional state of the ion residing at the center segment is measured by driving the stimulated Raman transition on the carrier or on the axial sidebands with a pulse time t, followed by detection of the spin state (see Sec. 2.2). Finally, the sequence of transports and separation is executed in reverse order to restore the initial situation. The sequence can be carried out with mirrored transports to measure the state of the second ion.

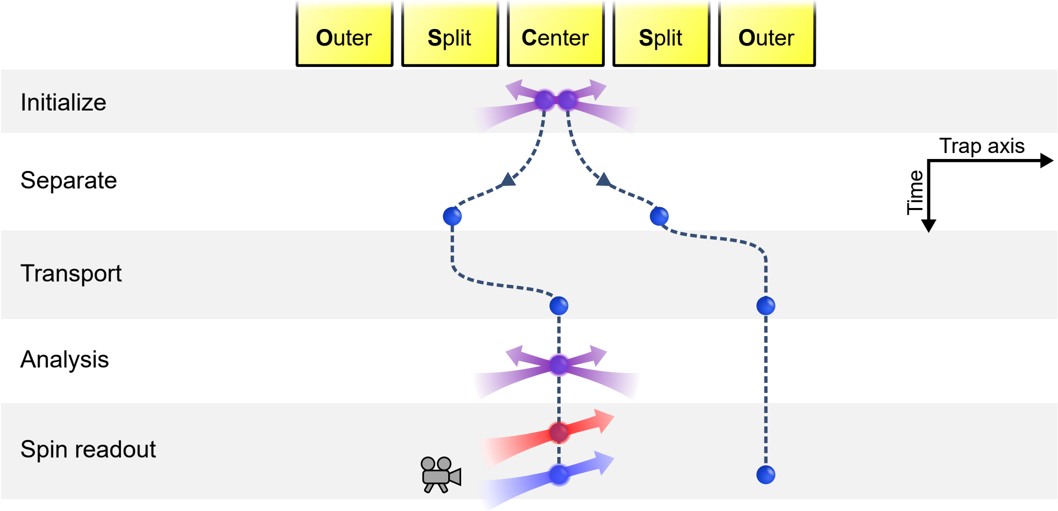

Figure 5.6.: Experimental procedure for measuring the ions' motional state after the separation procedure. The ions are first cooled and initialized at the center segment. After separating the ion crystal, ion 2 is moved to its outer segment, and ion 1 is transported back to the center segment, where driving of Rabi oscillations and spin readout take place.

After carrying out the experimental procedure 200 times, the occupation probability $p_{\uparrow,\Delta n}(t)$ of being in the state $|\uparrow\rangle$ is obtained. Here, Δn denotes the phonon number change pertaining to the transition that has been driven. By scanning t and acquiring data for several Δn, we can infer the phonon probability distribution p_n (see Sec. 2.3). For mean phonon numbers $\overline{n} \leq 20$, the carrier transition is probed ($\Delta n = 0$) as well as the red and blue sidebands ($\Delta n = \pm 1$). For higher phonon numbers, the second red sideband ($\Delta n = -2$) is also probed. Assuming displaced thermal states, the thermal and oscillatory mean phonon numbers $\bar{n}_{\text{th}}$ and $\bar{n}_{\text{coh}}$ can be extracted from a simultaneous curve fit[4] to all recorded transitions Δn. This method enables us to infer excitations of up to $\bar{n}_{\text{coh}} \lesssim 400$ at relative accuracies of about 5% near the ground state to 10% for large excitations, and allows for distinguishing thermal and oscillatory excitation. Case examples for Rabi oscillation data are shown in Fig. 5.7.

We investigate the dependence of the final motional excitation of the ions in the V1 trap on three parameters: (i) the voltage ΔU_{O} modifying the tilt field γ, (ii) the critical-point offset voltage at the center segment $\delta U_{\text{C}}^{(\text{CP})}$, and (iii) the total separation duration T. Figure 5.8 shows the measurement results. The energy increase for each ion in phonons pertaining to the final trap frequency at the center segment is obtained.

The dependence on the tilt field γ is characterized by measuring the motional excitation for different voltages ΔU_{O} at a total separation duration of 80 µs. The results are shown in Fig. 5.8(a). The energy increase of both ions is minimized for a tilt field where the energy increase is roughly equal for both ions. The best result is $\bar{n}_{1,\text{tot}} = 4.63(23)$

---

[4] Bayesian parameter estimation based on a Markov chain Monte-Carlo sampling method, developed by Ulrich Poschinger

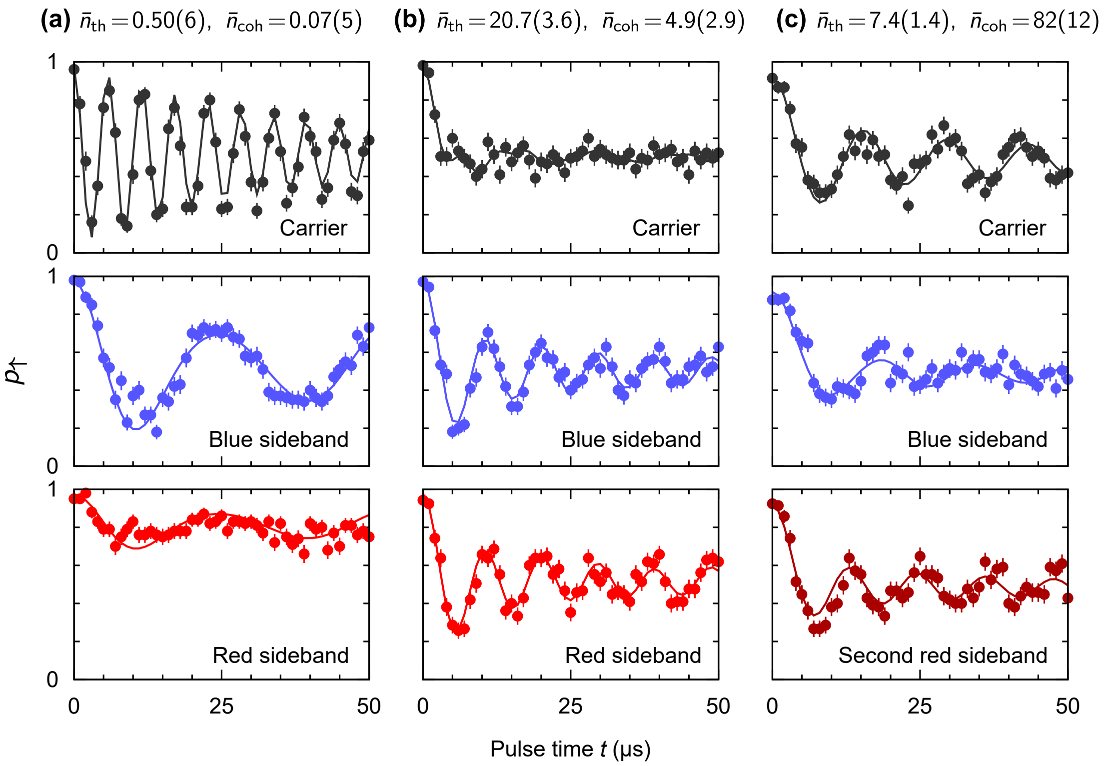

Figure 5.7.: Examples for the analysis of the vibrational state of a single ion by Raman excitation. **(a)** Rabi oscillations for an ion cooled close to the motional ground state, with (top to bottom) the carrier transition ($\Delta n = 0$), blue sideband ($\Delta n = +1$) and red sideband ($\Delta n = -1$). Blue and red sideband clearly exhibit different signals. **(b)** Similar data for an ion with thermal excitation of $\bar{n}_{\mathrm{th}} = 20.7(3.6)$, where no coherent dynamics is observed on the carrier, while the sidebands display Rabi oscillations. **(c)** Data for strong oscillatory excitation $\bar{n}_{\mathrm{coh}} = 82(12)$, where the second red sideband ($\Delta n = -2$) is used rather than the first red sideband to gain more information from the measurement. In all panels, the solid lines originate from a simultaneous fit of the data pertaining to the different transitions.

and $\bar{n}_{2,\mathrm{tot}} = 3.69(22)$. The voltage ΔU_{O} corresponding to theses values differs slightly from the center of the success range by about -2 mV. For a deviation from the optimum voltage of about 4 mV, strong oscillatory excitation on at least one of the ions corresponding to > 10 phonons occurs.

The dependence on the voltage offset $\delta U_{\mathrm{C}}^{(\mathrm{CP})}$ near the critical point, as shown in Fig. 5.8(b), is less pronounced. It has to be correctly set to an accuracy of about 10 mV to circumvent coherent excitation. A deviation of the optimum value of -70 mV with respect to the ideal case (0V) is observed, which presumably compensates for inaccuracies of the trap calibration data and voltage waveform distortions caused by the 50 kHz low-pass filters. For correct settings of $\delta U_{\mathrm{C}}^{(\mathrm{CP})}$ and ΔU_{O} at a separation duration of 80 µs, the motional excitation is dominated by heating.

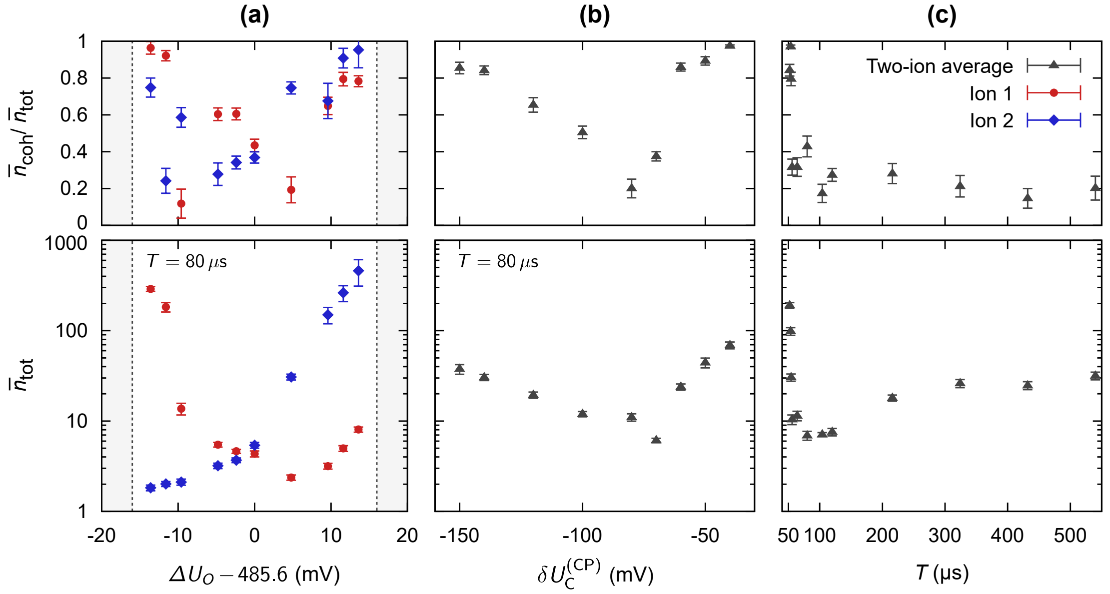

Figure 5.8.: Measured total motional excitation and coherent fraction after the separation process in the V1 trap versus **(a)** the tilt-compensation voltage ΔU_{O}, **(b)** the offset voltage of the center segment at the critical point $\delta U_{\mathrm{C}}^{(\mathrm{CP})}$, and **(c)** the total separation duration T. The tilt-compensation voltage ΔU_O had been calibrated to the best value for each measurement point in (b) and (c), and the optimal voltage $\delta U_{\mathrm{C}}^{(\mathrm{CP})}$ had been calibrated for each measurement point in (a) and (c) to compensate for drifts. For the dependency on ΔU_{O}, the motional excitation for each ion, while for the other parameters, the averaged excitation over both ions is shown. The gray shaded regions indicate values for ΔU_{O} where the separation failed.

Finally, we vary the total separation duration T, see Fig. 5.8(c). The offset voltage $\delta U_{\mathrm{C}}^{(\mathrm{CP})}$ and the tilt-compensation voltage ΔU_{O} are optimized for each duration T in order to compensate for voltage waveform distortions caused by the low-pass filters. This optimization is efficiently performed by probing carrier Rabi oscillations on the stimulated Raman transition at a pulse area of π, where a large spin excitation indicates low motional excitation. For durations below 60 µs, oscillatory excitation is dominant. In this regime, the excitation of the ions is extremely sensitive to the duration: Below 50 µs, even qubit readout is compromised, which indicates residual energies of $\bar{n} \gtrsim 400$ phonons per ion. In this regime, exponential behavior of the energy transfer, $\bar{n} \propto \exp(-T/\tau)$, with a time constant of $\tau = 1.4(2)$ µs is observed. This agrees well with numerical simulations performed by Kaufmann et al. [Kau14]. For separation durations longer than 60 µs, the excitation is mainly caused by heating. Given that the minimum total excitation is obtained if oscillatory and thermal excitation are of similar magnitude, the observed optimum value of $\bar{n} = 4.16(0.16)$ phonons per ion at a duration of $T = 80$ µs is roughly consistent with the expected amount of heating of 2.3(6) phonons per ion.

The separation of ion crystals has also been realized for $^{9}\mathrm{Be}^{+}$ ions by Bowler et al. [Bow12]. There, an energy increase of about two phonons per ion within a duration of 55 µs has been observed. Taking into account the higher trap frequencies due to the lighter mass of $^{9}\mathrm{Be}^{+}$ ions, we achieve a rather similar energy transfer within a similar separation time.

5.5. Conclusion

An ion-separation protocol has been successfully implemented that keeps the motional excitation in the few-phonons regime. It is mandatory to calibrate the trap parameters accurately and to adapt the voltage ramps with respect to the findings. Best performance has been achieved with separation durations comparable to that of entangling gate operations, and being well below the decoherence timescales of typical trapped-ion qubit systems.

The lowest attained energy increase and the energy increase at longer separation times is determined by heating in the V1 trap. This limitation has already been overcome with the V2 trap in the current experimental setup, and thus the energy increase is expected to be significantly lower in future experiments.

Technological improvements on arbitrary waveform generators [Bai13, Bow13] will allow for increasing the quartic confinement at the critical point. While the presented results have been acquired with a voltage range of ±10 V on the DC trap electrodes, the arbitrary waveform generator in the current experimental setup delivers voltages in the range of ±40 V. An increased quartic confinement would enable faster separation operations at low energy increase, as the tighter confinement serves to suppress undesired excitation at the critical point. Moreover, the cut-off frequency of the employed low-pass filters could be increased, which would enable faster separation durations.

The presented approach does not yet rely on a dedicated control strategy [Che11, Pal13], i.e. the limit pertaining to *adiabatic* separation is reached. Future investigations will include the applicability of techniques such as invariant-engineering approach or optimal-control theory to the separation process [Für14]. It is expected that such optimizations to the separation technique, combined with the already established technological improvements, will enable separation durations in the 30 µs range, at energy transfers below the single-phonon level.

The combination of ion-crystal separation and ion transport enables laser addressing and state detection of single ions. This is a prerequisite for various applications, e.g. for performing complete state tomography on a multi-qubit quantum state. Moreover, separation and transport are key ingredients for the magnetometer presented in chapter 7.

6 Spin-qubit coherence times

One of the key properties of quantum devices is the stability of the populated quantum states. Fluctuating energy levels lead to decoherence and limit the timescale during which the phase of superposition states is well defined. A stable phase relation is not only crucial for quantum computers, but also for quantum sensors. In the following chapter, we characterize the coherence time of the $^{40}\mathrm{Ca}^{+}$ spin qubit in the present experimental apparatus. All measurements have been carried out in the V2 ion trap.

For the ground-state spin levels, the main decoherence mechanism is given by magnetic-field fluctuations. Spontaneous decay does not play a role, and stimulated Raman transitions between the qubit states only require stability of the *relative* optical phase between the laser beams.

In Sec. 6.1, an efficient method for measuring the qubit coherence time is presented, and the results are shown in Sec. 6.2. The effect of long-term drifts of the magnetic field on the coherence time is investigated in Sec. 6.3. Section 6.4 discusses the effect of the 50 Hz AC-mains oscillations, and Sec. 6.5 describes further limitations in the current experimental setup.

6.1. Characterization method

In the presence of magnetic-field fluctuations, the magnetic field $B(t)$ differs during each repetition of an experiment. A single-qubit superposition state

$$|\Psi\rangle = \Big(|{\downarrow}\rangle + \mathrm{e}^{\mathrm{i}\varphi(t)}\,|{\uparrow}\rangle\Big)\big/\sqrt{2} \quad , \qquad \varphi(t) = \int_0^T \frac{g\mu_\mathrm{B}}{\hbar} B(t)\,\mathrm{d}t \tag{6.1}$$

thus accumulates a varying phase $\varphi(t)$ during a wait time T in each experimental run. In an ensemble-description of the measurement process, the state of a single qubit is represented by a density matrix

$$\hat{\rho} = \begin{pmatrix} p_\uparrow & \frac{C}{2}\mathrm{e}^{\mathrm{i}\varphi} \\ \frac{C}{2}\mathrm{e}^{-\mathrm{i}\varphi} & p_\downarrow \end{pmatrix} . \tag{6.2}$$

Here, $p_\uparrow$ and $p_\downarrow$ are the populations in the respective spin states, and the phase φ is an average over all repetitions. The contrast $C \in \left[0, 2\sqrt{p_\uparrow \cdot p_\downarrow}\right]$ describes the phase stability during the measurement. For $C = 1$, the phase is well defined and the density matrix corresponds to the pure state $|\Psi\rangle$. For $C = 0$, the qubit is fully described by a classical statistical mixture and the phase is completely undefined. We can therefore characterize the coherence time of a single qubit by measuring the contrast C of a superposition state for varying wait times T. However, the off-diagonal elements of the density matrix are inaccessible by our usual spin-readout scheme, where only the populations $p_\uparrow = \mathrm{Tr}\left(\hat{\rho}\,\hat{P}_\uparrow\right)$ and $p_\downarrow = 1 - p_\uparrow$ are measured. Here, $\hat{P}_\uparrow = |\uparrow\rangle\langle\uparrow|$ denotes the projection operator onto the $|\uparrow\rangle$-state.

For fully determining the density matrix, we perform quantum state tomography [Jam01]. This scheme relies on the fact that the density matrix can be expressed by a sum of Pauli matrices and the identity matrix $\hat{I}$ via

$$\hat{\rho} = \frac{1}{2}\left(\hat{I} + n_x\hat{\sigma}_x + n_y\hat{\sigma}_y + n_z\hat{\sigma}_z\right). \tag{6.3}$$

We infer the coefficients n_x, n_y, and n_z by inserting Eq. 6.2 into 6.3:

$$\begin{aligned} n_x &= C\cos(\varphi) = \mathrm{Tr}\left(\hat{\rho}\,\hat{\sigma}_x\right) && (6.4)\\ n_y &= -C\sin(\varphi) = \mathrm{Tr}\left(\hat{\rho}\,\hat{\sigma}_y\right) && (6.5)\\ n_z &= 2p_\uparrow - 1 = \mathrm{Tr}\left(\hat{\rho}\,\hat{\sigma}_z\right). && (6.6) \end{aligned}$$

The coefficients are thus given by the expectation values of the respective operators $\hat{\sigma}_x$, $\hat{\sigma}_y$, and $\hat{\sigma}_z$. It is evident that $p_\uparrow$, as obtained from spin readout in the experiment, contains the same information as n_z. In the Bloch-sphere representation of the qubit, measurement of the operators $\hat{\sigma}_x$, $\hat{\sigma}_y$, and $\hat{\sigma}_z$ is equivalent to projecting the Bloch vector of the state to either the x, y, or z-axis.

The determination of n_x and n_y in the experiment can be accomplished by applying a $\pi/2$ analysis laser pulse prior to spin readout. For the measurement of n_x, the phase of the analysis pulse is shifted by $\pi/2$ with regard to previous laser pulses. The results of these additional measurements

$$\begin{aligned} p_x &= \mathrm{Tr}\left(\hat{R}_{\frac{\pi}{2}}(\tfrac{\pi}{2})\,\hat{\rho}\,\hat{R}_{\frac{\pi}{2}}(\tfrac{\pi}{2})^\dagger\hat{P}_\uparrow\right) = \frac{1}{2}\left(1 - C\cos\varphi\right) && (6.7)\\ p_y &= \mathrm{Tr}\left(\hat{R}_0(-\tfrac{\pi}{2})\,\hat{\rho}\,\hat{R}_0(-\tfrac{\pi}{2})^\dagger\hat{P}_\uparrow\right) = \frac{1}{2}\left(1 + C\sin\varphi\right) && (6.8) \end{aligned}$$

contain the same information as n_x and n_y, respectively. From now on, we simply refer to them as $\hat{\sigma}_x$ and $\hat{\sigma}_y$ measurements. Using both results, the contrast and the phase can, in principle, be obtained by solving Eqs. 6.7 and 6.8 for C and φ:

$$C = 2\sqrt{\left(p_x - \tfrac{1}{2}\right)^2 + \left(p_y - \tfrac{1}{2}\right)^2} \tag{6.9}$$

$$\varphi = -\arctan\left(\frac{p_y - \frac{1}{2}}{p_x - \frac{1}{2}}\right) \tag{6.10}$$

Since results from a finite number of projective measurements are subject to statistical fluctuations, Eq. 6.9 might lead to unphysical values for the contrast $C \notin [0, 1]$. This can be prevented by employing the *maximum-likelihood estimation* method.

Spin readout is a realization of a Bernoulli process - the probability to detect the $|\uparrow\rangle$-state n times out of N trials for the $\hat{\sigma}_x$ measurement and m times out of M trials for the $\hat{\sigma}_y$ measurement is therefore governed by binomial statistics:

$$L(C,\varphi) := p(n,m\,|\,C,\varphi) \propto p_x^n(1-p_x)^{N-n}p_y^m(1-p_y)^{M-m}. \tag{6.11}$$

The function $L(C,\varphi)$ is called *likelihood function*, and expresses the probability that the joint measurement result $\{n,m\}$ is obtained for given parameters C and φ. By maximizing L with respect to C and φ, we obtain estimates $\langle\varphi\rangle$ and $\langle C\rangle$ for both parameters. If the sample sizes N and M are large, the log-likelihood ratio

$$R(C,\varphi) = 2\log\left(\frac{L\,(C,\varphi)}{L_{\max}}\right) \tag{6.12}$$

is approximately χ^2-distributed, and 68.3%-confidence intervals can be obtained via $R(C,\langle\varphi\rangle) \leq 1$ for C and $R(\langle C\rangle,\varphi) \leq 1$ for φ.

By using this evaluation method, the contrast C is constrained to the range $[0,1]$, but is slightly underestimated for cases where $C \lesssim 1$ [Sch15]. This phenomenon occurs mainly for phases that are not an integer multiple of $\pi/2$, which leads to unfavorable readout probabilities neither close to zero nor to one for *both* σ_x and σ_y measurements, so that readout noise increases. For these cases, the maximum-likelihood estimation of C yields reduced values with increased error bars. This behavior does not significantly affect the obtained coherence times, though.

6.2. Coherence-time measurements

We characterize the qubit coherence via *Ramsey-type* measurements. Each measurement sequence starts with a $\pi/2$-laser pulse on a single Doppler-cooled ion initialized in $|\uparrow\rangle$, resulting in the superposition state $\frac{1}{\sqrt{2}}\left(|\uparrow\rangle - \mathrm{i}\,|\downarrow\rangle\right)$. The ion is then shuttled to the neighboring segment in order to avoid residual scattering of photons on the $\mathrm{S}_{1/2} \leftrightarrow \mathrm{P}_{1/2}$ cycling transition due to imperfect switch-off of the laser near 397 nm. During a wait time T, the superposition accumulates a phase φ, yielding the state $\frac{1}{\sqrt{2}}\left(|\uparrow\rangle + \mathrm{e}^{\mathrm{i}\varphi}\,|\downarrow\rangle\right)$. Then, the ion is transported back to the laser interaction zone, where a concluding $\pi/2$-laser pulse with (without) $\pi/2$ phase w.r.t the first pulse is applied, followed by spin readout. This corresponds to measurement of the $\hat{\sigma}_x$ ($\hat{\sigma}_y$) operator. The experiment is repeated for a given wait time with alternating measurements of the $\hat{\sigma}_x$ and $\hat{\sigma}_y$ operators until each operator has been measured 300 times.

All electrical devices in the laboratory are connected to the AC mains and thus generate magnetic fields oscillating at the AC-line frequency of 50 Hz. In order to avoid decoherence caused by these fields, the start of each experimental cycle is synchronized with the AC line.

The measured Ramsey contrasts are shown in Fig. 6.1(a). For the case with permanent magnets, a Gaussian decay $C(T) = \exp\left(-T^2/(2(T_d^*)^2)\right)$ with a dephasing time constant of $T_d^* = 370(40)$ ms is obtained. The decay function depends on the type of noise present in the system, and therefore allows for inferring information about the noise $\delta B(t)$. In typical theoretical treatments, the noise is assumed to be a stationary Gaussian process, characterized by its autocorrelation function $\langle \delta B(t+\tau)\delta B(t)\rangle$ [Mon11b, Deg17]. Gaussian contrast decay occurs if the correlation time is long compared to the wait time in the experiment. Uncorrelated noise, e.g. white noise, would lead to exponential contrast decay.

For the case with coils, the Ramsey coherence time is 26(2) ms. This is only a modest increase compared to 8(1) ms with both top segments of the magnetic-shielding enclosure removed. We conclude that, in typical laboratory environment, the impact of ambient magnetic-field noise is on the same order of magnitude as the noise generated by low-noise current supplies. A substantial enhancement of coherence times thus requires *both* magnetic shielding and permanent magnets.

In addition to Ramsey-type measurements, we also perform *spin-echo* experiments (also known as Hahn-echo) with a refocusing π-pulse at half the wait time. The π-pulse reverses the sign of the phase accumulation rate during the second half of the wait time, suppressing fluctuations on a timescale slower than the total wait time. For the case with permanent magnets, the application of the refocusing pulse increases the coherence time to $T_d = 2.12(7)$ s (Fig. 6.1(b)). In our case of Gaussian contrast decay, the observed dephasing time corresponds to an rms amplitude of the effective magnetic-field fluctuations of about $\sqrt{\langle \delta B^2\rangle} = \hbar/(2\mu_\mathrm{B} T_d) = 2.7$ pT [Mon11a, Appendix A].

6.3. Long-term stability

The limiting mechanism for the Ramsey-type measurements with permanent magnets is most likely a magnetic-field drift on a minutes to hours timescale, induced by temperature drifts of the magnets. This would correspond to non-stationary noise, where the mean value of the magnetic field is different for each repetition of the experimental sequence. In order to verify this presumption, we first derive the expected contrast decay under the assumption that the ground-state Zeeman splitting is linearly drifting over time: $\omega(t) = \eta t + \omega_0$, with the constant drift rate η. We assume that each experimental cycle $j \in [1, N+M]$, described by the wave function $|\Psi_j(T)\rangle$, contributes to the density matrix via

$$\hat{\rho}(T) = \frac{1}{N+M} \sum_{j=1}^{N+M} |\Psi_j(T)\rangle \langle \Psi_j(T)| \,. \tag{6.13}$$

We infer the contrast from the off-diagonal matrix elements via

$$C_d(T) = 2\,|\langle\uparrow|\,\hat{\rho}(T)\,|\downarrow\rangle| = \frac{1}{N+M} \left| \sum_{j=1}^{N+M} \exp\left(\mathrm{i}\varphi_j(T)\right) \right| \tag{6.14}$$

with the accumulated phase of each experimental cycle

$$\varphi_j(T) = \int_{t_0}^{t_1} \omega(t)\,\mathrm{d}t = \tfrac{1}{2}\eta\left(t_1^2 + t_0^2\right) + \omega_0\left(t_1 - t_0\right). \tag{6.15}$$

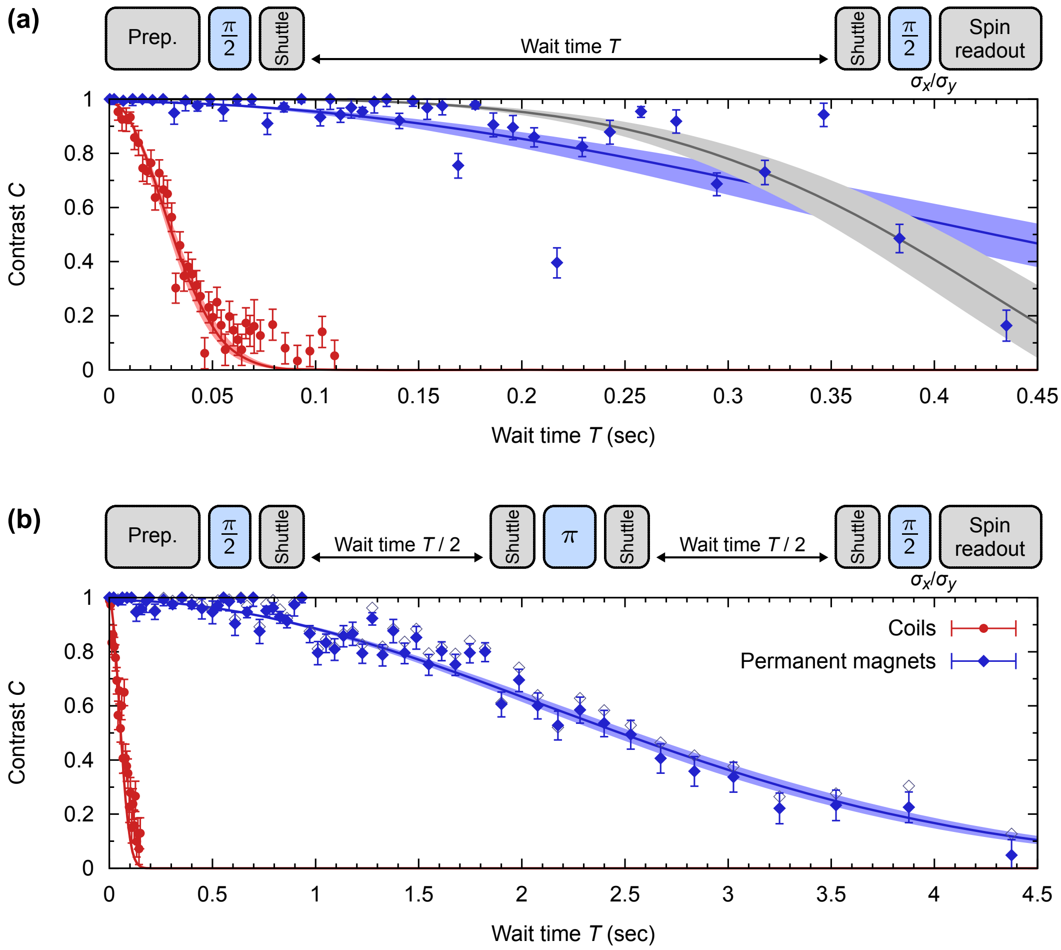

Figure 6.1.: Measured contrast versus wait time, with synchronization to the AC line and the magnetic-shielding enclosure fully installed. **(a)** shows data from Ramsey-type measurements, and **(b)** shows data from spin-echo measurements. Note the different scales on the x axes. Gaussian fits to the data (solid lines with 68%-confidence bands) reveal the $1/\sqrt{\mathrm{e}}$ coherence time for the settings with permanent-magnets (blue solid squares) and coils (red solid points). The fit results are summarized in Table 6.1. In (a), a fit of Eq. 6.19 (gray line with 68%-confidence bands) to the permanent-magnet data reveals a qubit-frequency drift of $\eta = 2\pi \cdot 23(3)$ Hz/h. In (b), open squares correspond to the permanent-magnet data with applied readout-error compensation. For each data point, the operators $\hat{\sigma}_x$ and $\hat{\sigma}_y$ were measured 300 times each, and the contrast was inferred via maximum-likelihood estimation (see text). The respective measurement sequences are depicted above each panel.

The boundaries of the integral are given by $t_0 = \tau(T)(j-1)$ and $t_1 = t_0 + T$, with $\tau(T)$ the duration of an experimental cycle. Then, the phase is given by

$$\varphi_j(T) = \eta\tau(T)Tj + \left(\tfrac{1}{2}\eta T^2 + \omega_0 T - \eta\tau(T)T\right) \tag{6.16}$$

and the contrast becomes

$$C_d(T) = \frac{1}{N+M}\left|\sum_{j=1}^{N+M} \exp\left(\mathrm{i}\eta\tau(T)Tj\right)\right|. \tag{6.17}$$

This expression can be simplified by considering the finite sum of the geometric series

$$\sum_{j=1}^{n} ar^{(j-1)} = \frac{a(1-r^n)}{1-r} \tag{6.18}$$

for $r \neq 1$. We finally obtain

$$C_d(T) = \frac{1}{N+M}\left|\frac{1-\exp(\mathrm{i}\eta\tau(T)T(N+M))}{1-\exp(\mathrm{i}\eta\tau(T)T)}\right|. \tag{6.19}$$

The duration of an experimental cycle is about $\tau(T) \approx 1.1(T+\delta)$, with δ the duration required for state initialization and readout. The factor 1.1 arises due to overhead from the experimental control system. A fit to the experimental data is shown in Fig. 6.1(a), and reveals a drift rate of $\eta = 2\pi \cdot 23(3)$ Hz/h. The curve $C_d(T)$ is in good agreement with the data. There are noticeable fluctuations of the measured contrasts at wait times $T > 0.15$ s, much larger than one would expect from the statistical error bar. This behavior is presumably caused by a time-dependent drift rate of the magnetic field.

Equation 6.19 shows that averaging over more experimental cycles does not necessarily reduce the fluctuations in the data: Even though the statistical error of each point shrinks with a higher number of experimental cycles, the measurement duration increases and the dependence of the contrast on the drifting magnetic field is enhanced.

A more suitable method for characterizing long-term drifts of the magnetic field is to repeatedly perform Ramsey measurements with *fixed* wait time, here $T = 15$ ms. The qubit frequency is inferred from the extracted phase of each measurement. The results are shown in Fig. 6.2. A maximum drift rate of about $2\pi\cdot 180$ Hz/h, and a total frequency change of about $2\pi \cdot 700$ Hz over 10 hours is observed. The settling behavior indicates that thermal drifts are most likely responsible for the qubit-frequency drift. With the dependence of the remanence of $\mathrm{Sm_2Co_{17}}$ of $-0.03\%/\mathrm{K}$, the data would correspond to a temperature change of about -0.2 K within 10 hours.

In additional measurements carried out by Nicodemus [Nic17], the qubit frequency drift has been simultaneously recorded along with the temperature of the magnet rings, revealing a near-perfect correlation between both parameters consistent with the temperature coefficient of $\mathrm{Sm_2Co_{17}}$. We conclude that the measured Ramsey-coherence times are limited by temperature drifts of the permanent magnets.

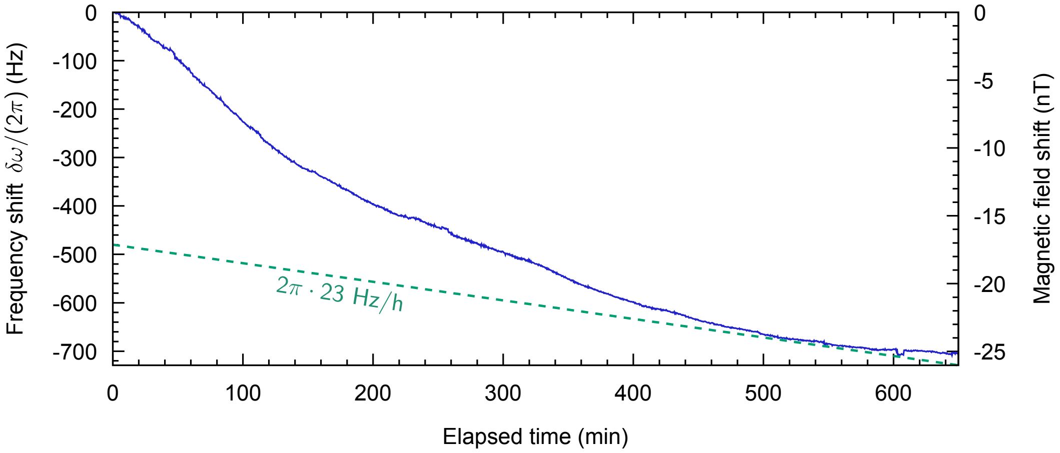

Figure 6.2.: Qubit frequency drift: The shift of the qubit frequency for the case with permanent magnets and closed shielding enclosure is tracked over a time of more than 10 hours via Ramsey measurements at 15 ms wait time. The measurement was started in the evening, and overnight settling can be clearly recognized. The measurement is performed similarly to the measurements presented in Fig. 6.1. The dashed line indicates the drift rate inferred from the Ramsey coherence-time measurement.

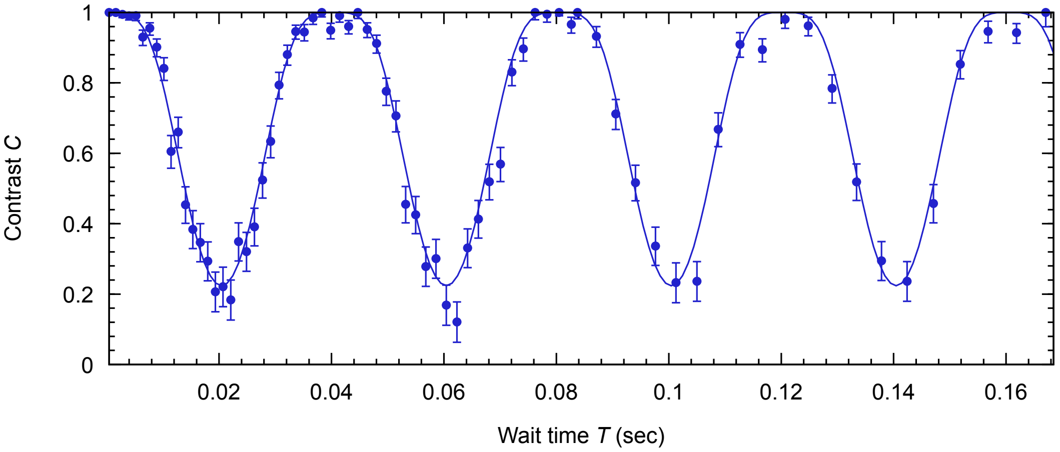

Figure 6.3.: Measured contrast versus wait time without triggering to the AC line, for the case of closed shielding and permanent magnets. The data shows results from spin-echo measurements, and the solid line is a fit to Eq. 6.21. The periodic contrast loss is caused by increased phase accumulation from magnetic fields oscillating at the AC-line frequency, enhanced by the refocusing pulse at half the line period. The inferred qubit frequency-modulation depth is $\Delta_{\mathrm{ac}} = 2\pi \cdot 25.0(5)$ Hz. The data was taken with the same method and parameters as in Fig. 6.1 (see text).

6.4. Residual AC line-induced field

Spin-echo measurements with one or more refocusing pulses allow for measuring the spectral components of magnetic-field noise [Kot11]. For the setting with permanent magnets and closed shielding enclosure, we quantify the residual field fluctuations at the 50 Hz AC-line frequency by performing spin-echo measurements without triggering to the AC line. As can be seen in Fig. 6.3, periodic loss and revival of coherence is observed at a period corresponding to the AC-line frequency. This occurs because refocusing at half the line period leads to the adverse effect of increase rather than cancellation of the accumulated phase. Assuming sinusoidal modulation of the qubit frequency at a line frequency of $\omega_{\mathrm{ac}} = 2\pi \cdot 50$ Hz, at a frequency-modulation depth Δ_{ac} and a random phase at sequence start χ_{ac}, the qubit accumulates a phase

$$\varphi_{\mathrm{ac}}(T, \chi_{\mathrm{ac}}) = \int_0^{T/2} \Delta_{\mathrm{ac}} \sin(\omega_{ac} t + \chi_{ac})\, \mathrm{d}t - \int_{T/2}^{T} \Delta_{\mathrm{ac}} \sin(\omega_{ac} t + \chi_{ac})\, \mathrm{d}t. \tag{6.20}$$

Here, we take into account the inversion of the phase accumulation rate after the refocusing π-pulse. We assume a uniform distribution of the phase χ_{ac} of the sequence start w.r.t. the AC line, which is justified if the repetition rate is different from the line frequency. The resulting contrast is then given by averaging over φ_{ac} with respect to χ_{ac}:

$$C(T) = \frac{1}{2\pi} \left| \int_0^{2\pi} \exp(\mathrm{i}\varphi_{\mathrm{ac}}(T, \chi_{\mathrm{ac}}))\, \mathrm{d}\chi_{\mathrm{ac}} \right| = \left| {}_0F_1 \left(1, -\tfrac{4\Delta_{\mathrm{ac}}^2 \sin^4(\omega_{\mathrm{ac}} T/4)}{\omega_{\mathrm{ac}}^2}\right) \right|, \tag{6.21}$$

where ${}_0F_1\,(a, z)$ is the regularized confluent hypergeometric function. Fitting Eq. 6.21 to the measured data reveals a residual AC line-induced frequency deviation of $\Delta_{\mathrm{ac}} = 2\pi \cdot 25(3)$ Hz. For the situation with the magnetic field generated by coils, the frequency deviation is about $\Delta_{\mathrm{ac}} = 2\pi \cdot 300$ Hz, while the permanent magnets without shielding enclosure yield $\Delta_{\mathrm{ac}} = 2\pi \cdot 1.5$ kHz. Note that for these cases, the frequency deviations were measured by performing Ramsey measurements with short wait times < 2 ms for fixed phases χ_{ac} w.r.t. the AC line, which provides a direct measurement of the variation of the qubit frequency during an AC-line cycle. For comparison, the coherence times and AC-line modulation depths for various settings are summarized in Table 6.1.

6.5. Decoherence sources

The longest coherence times are obtained for the setting with closed shielding enclosure, refocusing pulse and AC-line triggering. In the following, we discuss the mechanisms which can cause the remaining decoherence.

Limited shielding efficiency of the μ-metal enclosure

The measured spin-echo coherence times are 2.12(7) s for the closed enclosure and 11(2) ms for the opened enclosure. The respective dephasing rates are proportional

Field generation	Shield	Trigger on AC line	T_d^* time (ms)	T_d time (ms)	$\Delta_{\mathrm{ac}}/2\pi$ (Hz)
Coils	open	no	0.30(5)	2.0(2)	2500(200)
		yes	8(1)	11(2)	
	closed	no	1.0(1)	3.0(2)	300(50)
		yes	26(2)	48(3)	
Magnets	open	no	0.35(5)	2.0(2)	1400(100)
		yes	11(4)	11(2)	
	closed	no	20(10)	>100	25(3)
		yes	370(40)	2120(70)	

Table 6.1.: Summary of coherence times and AC line-induced frequency deviations for different experimental settings. The dephasing times T_d^* are obtained from Ramsey measurements, whereas the dephasing times T_d result from spin-echo measurements. Both T_d^* and T_d times are reported as $1/\sqrt{e}$ times corresponding to Gaussian contrast decay. Note that not for all cases the decay exhibits a Gaussian behaviour, in theses cases the reported values correspond to the time at which the contrast drops below $1/\sqrt{\mathrm{e}}$. An exception is the case with permanent magnets, closed shielding enclosure and without AC-line trigger (second-last line, see Fig. 6.3), where the contrast periodically revives even beyond 100 ms.

to the rms magnetic-field fluctuation amplitude. Their ratio is consistent with the measured attenuation factor in the range of 150 to 300 at low frequencies [Kes12]. Thus, residual penetration of fluctuating ambient magnetic fields is most likely the dominating source of decoherence.

Fluctuations of the 50 Hz AC-mains frequency

Shifts of several milliseconds of the AC-mains phase at a delay of 2 s w.r.t. an initial trigger flank have been observed during an observation time of about 10 min. This is consistent with 0.05 Hz frequency fluctuations of the AC-mains frequency. Together with the peak-to-peak phase modulation depth of about 1 π for a spin-echo sequence, this leads to significant dephasing within the maximum measured wait time of 4 s.

Magnetization of the permanent magnets

While the long-term drift of the quantizing magnetic field has been characterized, see Fig. 6.2, noise from the magnets on short timescales has not been quantitatively characterized. Such noise might possibly contribute to the observed decoherence.

Ion-position drift

A fluctuating ion position within an inhomogeneous magnetic field leads to fluctuations of the qubit frequency. In Sec. 7.4, it is shown that the typical frequency drift caused by a drifting ion position is below $2\pi \cdot 1$ Hz/h, and therefore does not limit the coherence time in the current setup.

Phase drifts of the Raman laser beams

Drifts of the relative optical phase between the two beams driving the qubit via the stimulated Raman transition might be a possible error source. For a similar setup, phase drifts of the relative optical phase of about 3π have been observed within 10 minutes [Sch16a]. However, as the interferometer area in the present fiber-coupled setup is much smaller and the phase drifts within the duration of a measurement cycle of about 4 s are negligible, this mechanism can be excluded.

Deterioration of qubit-readout fidelity

Heating of the ion's radial modes of motion leads to an effective contrast loss during the wait time. The efficiency of the population transfer from the $|\uparrow\rangle$ state to the $\mathrm{D}_{5/2}$ manifold is lowered if the motion is excited during the wait time (see Sec. 3.5). In separate measurements, the spin-readout fidelity has been characterized for the input states $|\uparrow\rangle$ and $|\downarrow\rangle$ at variable wait times. The loss of readout fidelity has been determined to be 20% at a wait time of $T = 4$ s, and is therefore excluded to be a limiting mechanism. Contrasts corrected for readout-efficiency deterioration [Kau17b] are also shown in Fig. 6.1(a).

6.6. Conclusion

In conclusion, an environment for AMO-physics experiments at variable, intermediate magnetic fields with short-term fluctuations of $\sqrt{\langle \delta B^2 \rangle} \leq 2.7 \cdot 10^{-12}$ T has been realized. We compare our setup to other experimental environments with low magnetic-field noise: For high fields of a few T strength, specially arranged superconducting solenoids [Gab88] yield sub-nT rms magnetic-field noise in the frequency range of 10 - 200 Hz [Bri16], while for fully shielded large facilities operating at null field, rms field fluctuations in the femto-Tesla range are attained [Bor00].

In this work, so far unprecedented coherence times of first-order magnetic-field sensitive atomic qubits have been demonstrated. In typical laboratory environments, residual current fluctuations in field coils seem to have a similar impact as ambient magnetic-field fluctuations, thus long coherence times may be reached using permanent magnets *in conjunction* with proper shielding. The presented results will influence the choice of the employed ion species and experimental setups for future trapped-ion experiments. Also, for ion or neutral atom species with clock states, the detrimental impact of higher-order Zeeman shifts on the operation of atomic frequency standards or precision measurements could be mitigated.

7 DC magnetometry with entangled ions

While the techniques presented in the preceding chapters have mainly been developed in the context of quantum information processing, they are not restricted to this application. In fact, many methods for controlling quantum states with high precision can also be applied to realize quantum sensors [Deg17]. In the following chapter, we combine the techniques of ion-crystal separation, efficient readout of quantum phases, and two-ion entanglement in a low-noise environment to realize a DC magnetic-field sensor.

The sensing scheme relies on the entangled *sensor state* $|\psi(\varphi)\rangle = \left(|\uparrow\downarrow\rangle + \mathrm{e}^{\mathrm{i}\varphi}|\downarrow\uparrow\rangle\right)/\sqrt{2}$. This state is sensitive to magnetic-field differences $\Delta B(x_1, x_2)$ between the locations of the constituent ions x_1 and x_2, while rejecting common-mode magnetic-field fluctuations. The DC magnetic-field difference can be inferred from the phase accumulation rate of the sensor state via the linear Zeeman effect

$$\Delta\omega(x_1, x_2)_{\mathrm{DC}} \equiv \dot{\varphi}_{\mathrm{DC}} = \frac{g\mu_{\mathrm{B}}}{\hbar}\Delta B(x_1, x_2). \tag{7.1}$$

In Sec. 7.1, the scheme for measuring quantum phases of single qubits (see Sec. 6.1) is generalized to efficiently read out the relative phase of the sensor state, and possible systematic errors are discussed. In Sec. 7.2, the experimental implementation of the phase-measurement scheme is discussed, and applied in Sec. 7.3 to determine phase accumulation rates $\Delta\omega(x_1, x_2)$. The coherence time of the sensor state, which is the main limitation for the sensitivity, is investigated in Sec. 7.4. Section 7.5 introduces a Bayesian frequency-estimation scheme for measuring $\Delta\omega(x_1, x_2)$ with high dynamic range.

The energy levels of the sensor state do not only depend on the linear Zeeman effect, but also on an AC Zeeman shift caused by differential AC magnetic fields. In the experiment, the charging and discharging currents of the RF trap electrodes cause a spurious AC magnetic field and thus affect the phase accumulation rate $\Delta\omega(x_1, x_2)$. In Sec. 7.6, a sensing scheme is presented that allows for separating this AC Zeeman shift from the DC Zeeman effect. The scheme relies on consecutive measurements on sensor states encoded in the $\mathrm{S}_{1/2}$ ground state and in the $\mathrm{D}_{5/2}$ metastable state.

Finally, in Sec. 7.7, possible applications of the presented sensing scheme are discussed.

7.1. Phase estimation method

The density matrix of the sensor state $|\psi(\varphi)\rangle$ in the presence of magnetic-field fluctuations is given by

$$\hat{\rho} = \frac{1}{2}\begin{pmatrix} 0 & 0 & 0 & 0 \\ 0 & 1 & Ce^{-\mathrm{i}\varphi} & 0 \\ 0 & Ce^{\mathrm{i}\varphi} & 1 & 0 \\ 0 & 0 & 0 & 0 \end{pmatrix} \tag{7.2}$$

in the logical basis $\{|\uparrow\uparrow\rangle, |\uparrow\downarrow\rangle, |\downarrow\uparrow\rangle, |\downarrow\downarrow\rangle\}$, with the contrast $C \in [0,1]$. Both the phase φ and the contrast C can be determined by measuring the *parity* of the two operators $\hat{\sigma}_x \otimes \hat{\sigma}_x$ and $\hat{\sigma}_x \otimes \hat{\sigma}_y$. Similar to the measurement scheme presented in Sec. 6.1, the expectation values of these operators are measured by applying $\pi/2$ analysis laser pulses to each ion prior to spin readout. The parity is determined by the probability of projecting the quantum state of the ions to $|\uparrow\uparrow\rangle$ *or* $|\downarrow\downarrow\rangle$ during spin readout. The results of the $\hat{\sigma}_x \otimes \hat{\sigma}_x$ and $\hat{\sigma}_x \otimes \hat{\sigma}_y$ measurements are

$$p_{xx}^{(\mathrm{E})} = \mathrm{Tr}\left(\left(\hat{R}_{\frac{\pi}{2}}\left(\tfrac{\pi}{2}\right) \otimes \hat{R}_{\frac{\pi}{2}}\left(\tfrac{\pi}{2}\right)\right)\hat{\rho}\left(\hat{R}_{\frac{\pi}{2}}\left(\tfrac{\pi}{2}\right) \otimes \hat{R}_{\frac{\pi}{2}}\left(\tfrac{\pi}{2}\right)\right)^{\dagger}\hat{P}_{\mathrm{E}}\right) = \frac{1}{2}\left(1 + C\cos\left(\varphi\right)\right) \tag{7.3}$$

$$p_{xy}^{(\mathrm{E})} = \mathrm{Tr}\left(\left(\hat{R}_{\frac{\pi}{2}}\left(\tfrac{\pi}{2}\right) \otimes \hat{R}_{0}\left(-\tfrac{\pi}{2}\right)\right)\hat{\rho}\left(\hat{R}_{\frac{\pi}{2}}\left(\tfrac{\pi}{2}\right) \otimes \hat{R}_{0}\left(-\tfrac{\pi}{2}\right)\right)^{\dagger}\hat{P}_{\mathrm{E}}\right) = \frac{1}{2}\left(1 - C\sin\left(\varphi\right)\right), \tag{7.4}$$

where $\hat{P}_{\mathrm{E}} = |\uparrow\uparrow\rangle\langle\uparrow\uparrow| + |\downarrow\downarrow\rangle\langle\downarrow\downarrow|$ is the projector onto the subspace of even spin configurations $|\uparrow\uparrow\rangle$ and $|\downarrow\downarrow\rangle$. The operator $\hat{R}_{\pi/2}\left(\frac{\pi}{2}\right) \otimes \hat{R}_0\left(-\frac{\pi}{2}\right)$ is experimentally realized by shifting the phase of the analysis pulse by $\pi/2$ for only one ion, and thus requires laser-addressing of individual ions. Similar to the single-ion case, we determine φ and C via maximum-likelihood estimation.

The phase-estimation scheme is robust to population decay and imperfect state preparation: Inserting the more general density matrix

$$\hat{\rho}' = \begin{pmatrix} P_1 & c_2 & c_3 & 0 \\ c_2^* & P_2 & \frac{C}{2}e^{-\mathrm{i}\varphi} & c_4 \\ c_3^* & \frac{C}{2}e^{\mathrm{i}\varphi} & P_3 & c_5 \\ 0 & c_4^* & c_5^* & P_4 \end{pmatrix} \tag{7.5}$$

into Eqs. 7.3 and 7.4 yields the same result. Nonzero components in the matrix elements $\langle\uparrow\uparrow|\hat{\rho}'|\downarrow\downarrow\rangle$ and $\langle\downarrow\downarrow|\hat{\rho}'|\uparrow\uparrow\rangle$ would lead to additional oscillatory terms in the results of Eqs. 7.3 and 7.4. But as the states $|\uparrow\uparrow\rangle$ and $|\downarrow\downarrow\rangle$ do not reject common-mode magnetic-field fluctuations, these matrix elements decay significantly faster than the contrast C.

Let us now consider errors in spin readout *after* the basis rotations. We model imperfect shelving from the $|\uparrow\rangle$ state to the $\mathrm{D}_{5/2}$ manifold by modifying the projection operator on the even spin states to

$$\hat{P}_{\mathrm{E}} = \mathrm{diag}\left(p(\mathrm{E}\,|\uparrow\uparrow), p(\mathrm{E}\,|\uparrow\downarrow), p(\mathrm{E}\,|\downarrow\uparrow), p(\mathrm{E}\,|\downarrow\downarrow)\right) \tag{7.6}$$

where E now denotes the event that both ions have been projected to either the dark or bright state. In an ideal case, it is $\hat{P}_E = \mathrm{diag}\,(1,0,0,1)$, but for long interrogation times, residual heating of the motional state hampers the population transfer to the $\mathrm{D}_{5/2}$ state. If the loss of readout efficiency can be described by a single parameter $\delta \gtrsim 0$ such that

$$p(\mathrm{E}\,|\uparrow\uparrow) = p(\mathrm{E}\,|\downarrow\downarrow) = 1-\delta \tag{7.7}$$

$$p(\mathrm{E}\,|\uparrow\downarrow) = p(\mathrm{E}\,|\downarrow\uparrow) = \delta, \tag{7.8}$$

the probabilities to detect even parity become

$$p_{xx}^{(\mathrm{E})} = \frac{1}{2}\left(1 + C_{\mathrm{eff}}\cos\left(\varphi\right)\right) \tag{7.9}$$

$$p_{xy}^{(\mathrm{E})} = \frac{1}{2}\left(1 - C_{\mathrm{eff}}\sin\left(\varphi\right)\right) \tag{7.10}$$

with $C_{\mathrm{eff}} = C\,(1-2\delta)$. In this case, no systematic error is introduced, but the effective contrast is lowered.

The assumption that a single parameter δ fully describes the readout imperfection is well fulfilled if the laser power of the population-transfer pulses to the $\mathrm{D}_{5/2}$ state is adjusted correctly. At optimal conditions, deviations from Eqs. 7.7 and 7.8 in the experiment are less than 0.02, and therefore do not affect magnetic-field measurements on the present level of precision.

7.2. Experimental procedure

An experimental cycle starts with Doppler cooling a two-ion crystal at the laser interaction zone (LIZ) of the ion trap (Fig. 7.1). Then, all collective transverse modes of vibration are cooled close to the motional ground state via resolved sideband cooling, followed by spin initialization to the $|\uparrow\uparrow\rangle$ state. A $\pi/2$ pulse on both ions creates the superposition state $|\uparrow\uparrow\rangle + \mathrm{i}\,|\uparrow\downarrow\rangle + \mathrm{i}\,|\downarrow\uparrow\rangle - |\downarrow\downarrow\rangle$. Then, an entangling geometric phase gate is carried out (see Sec. 3.4), during which the parallel spin configurations $|\uparrow\uparrow\rangle$ and $|\downarrow\downarrow\rangle$ acquire a phase of $\pi/2$. After the phase gate, two additional $\pi/2$ pulses are applied to both ion spins, with respective phase shifts of 0° and −45° with regard to the initial $\pi/2$ pulse. These pulses lead to the sensor state $\left(|\uparrow\downarrow\rangle + |\downarrow\uparrow\rangle\right)/\sqrt{2}$.

For the subsequent operations, the two-ion crystal is separated. The ions are shuttled to the desired locations x_1 and x_2 with a maximum distance of 6.2 mm, and kept there for an interrogation time T. Any inhomogeneity of the magnetic field leads to the accumulation of a phase $\varphi(x_1, x_2, T)$, resulting in the state $|\psi(\varphi)\rangle = \left(|\uparrow\downarrow\rangle + \mathrm{e}^{\mathrm{i}\varphi}\,|\downarrow\uparrow\rangle\right)/\sqrt{2}$.

After the interrogation time T, both ions are consecutively moved back to the laser interaction zone for spin readout. There, local spin rotations are driven in order to measure the spins along the $\hat{\sigma}_x \otimes \hat{\sigma}_x$ or $\hat{\sigma}_x \otimes \hat{\sigma}_y$ basis. Population in the state $|\uparrow\rangle$ is then transferred for each ion to the metastable $\mathrm{D}_{5/2}$ state, followed by fluorescence readout on the $\mathrm{S}_{1/2} \leftrightarrow \mathrm{P}_{1/2}$ transition on each ion.

In order to confirm the validity of the sensor state generation, we reconstruct the density matrix of the state via complete state tomography [Jam01]. For this purpose, the entangled ions are separated and individually shuttled to the laser interaction zone, where

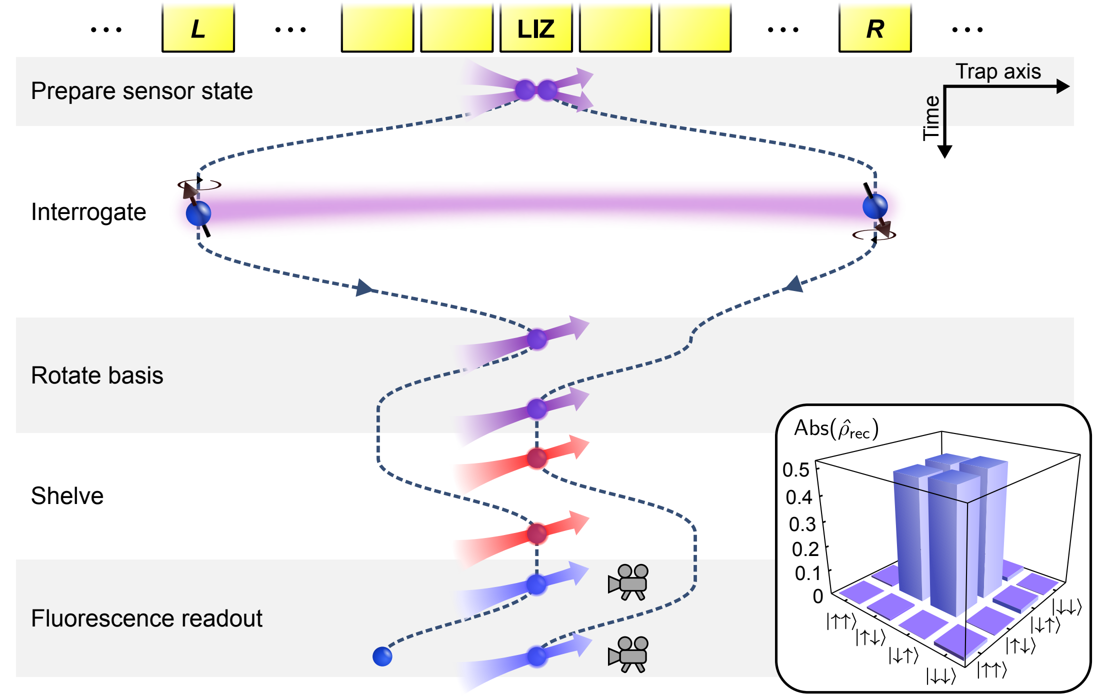

Figure 7.1.: Experimental procedure for measuring inhomogeneous magnetic fields. After creating the sensor state at the laser interaction zone (LIZ), the constituent ions are separated and shuttled to the desired trap segments L and R. In order to measure the accumulated phase during the interrogation time T, the ions are individually shuttled to the LIZ to perform basis rotations that allow for state readout via electron shelving and fluorescence detection in either the $\hat{\sigma}_x \otimes \hat{\sigma}_x$ or $\hat{\sigma}_x \otimes \hat{\sigma}_y$ basis. The inset depicts the absolute values of the reconstructed density matrix $\hat{\rho}_{\mathrm{rec}}$ of the sensor state. The data has been measured via complete state tomography (see text).

one of the rotation operations $\{\hat{I}, \hat{R}_0(-\frac{\pi}{2}), \hat{R}_{\pi/2}(\frac{\pi}{2})\}$ is carried out. Each of the resulting nine operators is measured 2000 times, and the density matrix $\hat{\rho}_{\mathrm{rec}}$ is reconstructed via linear inversion (Fig. 7.1 inset). The state fidelity $\mathcal{F} = \max_{\varphi} \mathrm{Tr}\left(\hat{\rho}_{\mathrm{rec}} \left|\psi(\varphi)\right\rangle \left\langle\psi(\varphi)\right|\right)$ with respect to a sensor state with arbitrary phase is computed to be 99.3(5)%[1]. Ignoring the relative phase in the fidelity calculation is justified as this parameter is taken into account in the frequency-estimation measurement. The sum of the undesired residual populations in the even states $|\uparrow\uparrow\rangle$ and $|\downarrow\downarrow\rangle$ is 0.47(14)%, which is sufficiently low to not cause significant systematic errors in the following measurements.

---

[1] Standard errors are deduced by parametric bootstrapping [Sch15], starting from an estimate given by a diluted maximum likelihood algorithm [Řeh07].

7.3. Phase accumulation measurements

In order to determine the phase accumulation rate $\Delta\omega(x_1, x_2)$ of the sensor state with both high sensitivity and high dynamic range, a measurement scheme is necessary that takes the 2π-ambiguity of phase measurements into account. Recently, measurement schemes [Nus12, Wal12a, Bon16] have been demonstrated where phase measurements at a few fixed interrogation times are performed to resolve this ambiguity. In these schemes, interrogation times and weight factors are carefully chosen to find an optimal balance between sensitivity and dynamic range. Better performance for high-dynamic range sensors is potentially offered by measurement schemes that adapt the interrogation time based on prior knowledge [Mac14]. Since these typically require a more complex implementation, the choice of a measurement scheme depends on the desired dynamic range of the sensor.

In order to estimate the required dynamic range of our sensor, we first perform an example measurement using a straightforward incremental approach, where phase measurements are consecutively carried out at slowly increasing, predefined interrogation times. A linear fit

$$\varphi(T; x_1, x_2) = \varphi_0(x_1, x_2) + \Delta\omega(x_1, x_2) \cdot T \tag{7.11}$$

then reveals the phase accumulation rate $\Delta\omega(x_1, x_2)$ and a phase offset $\varphi_0(x_1, x_2)$. The constant phase offset is accumulated during the ion movement in the inhomogeneous magnetic field. For each phase measurement at interrogation time T, the resulting phase $\varphi_{\text{meas}}(T; x_1, x_2)$ is incremented or decremented by multiples of 2π until it falls within a range of $\pm\pi$ to the fit function resulting from previous phase measurements, i.e. until $|\varphi(T; x_1, x_2) - \varphi_{\text{meas}}(T; x_1, x_2)| < \pi$. In order to check if the phase has been incremented or decremented properly, we verify that the residuals of all points are well below π. Figure 7.2 shows the example measurement at maximum ion distance $d = 6.2$ mm and the residuals $\delta\varphi$ for each point. Phases of over 40 000 rad have been accumulated during interrogation times of up to $T_{\text{max}} = 1.5$ s, but the residuals $|\delta\varphi|$ of all measurement points are well below π.

The maximum interrogation time T_{max} is ultimately limited by the coherence time T_{coh} of the sensor state. The coherence time is therefore analyzed in the following section.

7.4. Coherence times

We characterize the coherence time T_{coh} of the sensor state for two settings: The ions are kept (i) in a common harmonic potential well at a distance of about 4.2 µm, and (ii) in separate harmonic wells at the maximum possible distance of 6.2 mm. The coherence time is inferred from measurements of the contrast C for varying interrogation times T. For each interrogation time, the experimental procedure is repeated 400 times for each of the two measurement operators.

For case (i), a coherence time $T_{\text{coh}} > 12.5$ s is observed (Fig. 7.3(a)). The contrast loss is entirely caused by residual heating of the radial modes of motion, which compromises the fidelity of electron shelving and therefore the spin readout. This has been confirmed

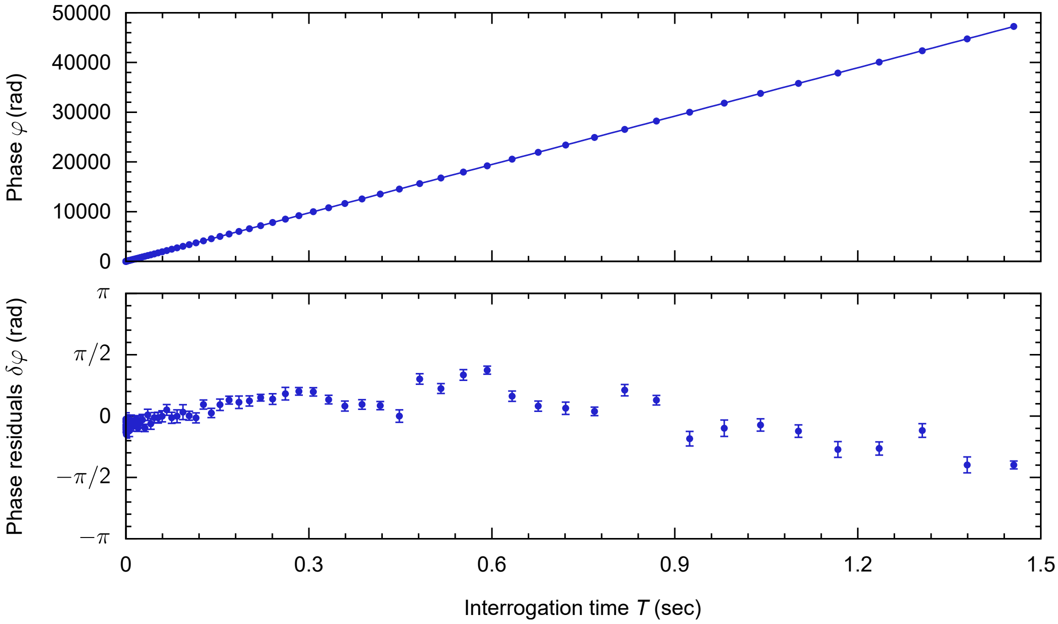

Figure 7.2.: Incremental measurement of the phase accumulation rate $\Delta\omega$ at an ion distance of $d = 6.2$ mm. A linear fit to measurements of the accumulated phase φ at predefined interrogation times (top part), and the fit residuals $\delta\varphi$ for each phase measurement are shown (bottom part). For each point, measurements of both operators $\hat{\sigma}_x \otimes \hat{\sigma}_x$ and $\hat{\sigma}_x \otimes \hat{\sigma}_y$ have been repeated 50 times.

by repeating the experimental procedure for the input states $|\uparrow\uparrow\rangle$ and $|\downarrow\downarrow\rangle$, and measuring the probabilities to detect each ion as "dark" or "bright".

For the maximum possible ion distance, a Gaussian contrast decay is observed, with a coherence time in the $1 - 2$ s range. For Gaussian contrast decay, the best sensitivity for magnetic-field measurements is achieved at an interrogation time corresponding to a contrast of 0.85 (see Appendix D).

The contrast decay at maximum ion distance is presumably caused by a slow drift of the magnetic-field minimum position along the trap axis. In order to verify this presumption, the drift rate of $\Delta\omega$ has been simultaneously measured for two different ion separation distances of $d = 6.2$ mm and $d = 3.2$ mm over the course of 6 hours (Fig. 7.3(b)). For the former case, a typical drift rate of $2\pi \cdot 1$ Hz/h is observed. This corresponds to contrast decay within 2 s (calculated via Eq. 6.19). For an ion distance of $d = 3.2$ mm, the drift rate is suppressed by a factor of about 1.6 as compared to the maximum ion distance. The spatial dependence of the observed drift rates is consistent with movement of the ion trap relative to the magnetic field in the 200 nm range, equivalent to thermal expansion of the vacuum chamber due to a temperature change of roughly 0.1°C.

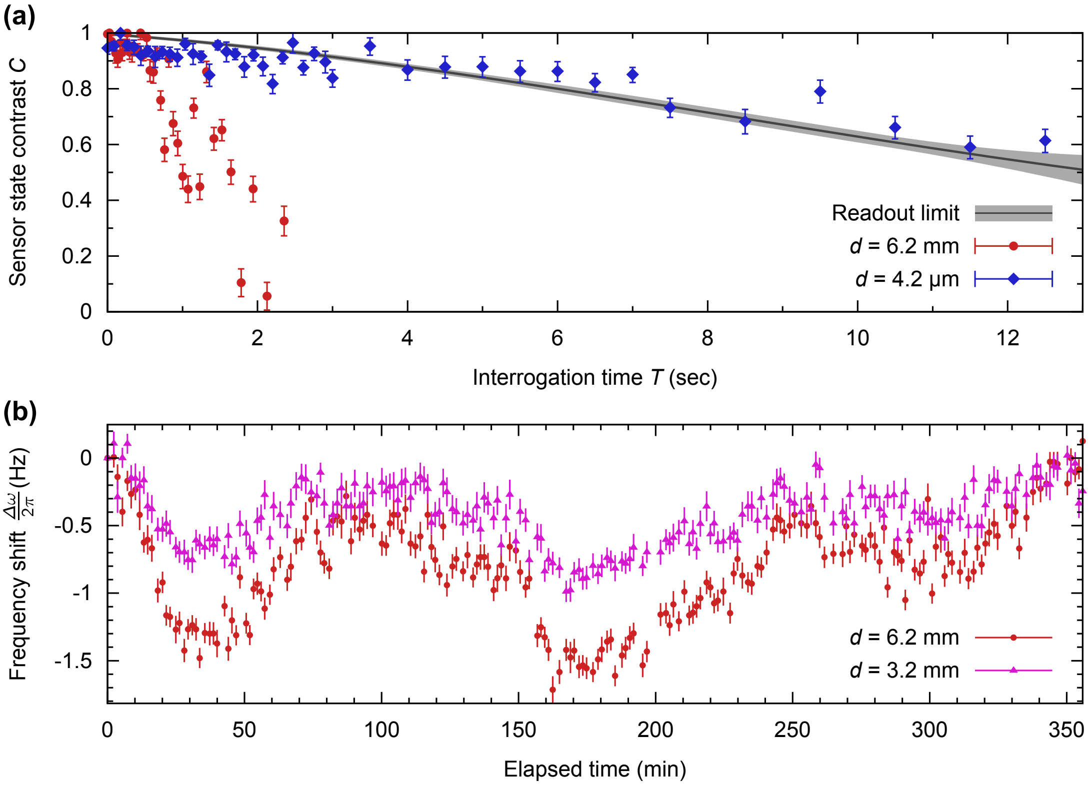

Figure 7.3.: (a) Sensor state contrast C versus interrogation time T at the maximum ion distance of $d = 6.2$ mm (red dots) and at an ion distance of $d = 4.2$ µm (blue squares). For illustration, the black curve and gray region indicate a third order polynomial fit to a separate readout-fidelity measurement and its confidence bands. **(b)** Simultaneous drift of the measured frequency difference for ion distances $d = 6.2$ mm (blue circles) and $d = 3.2$ mm (purple triangles) over a duration of about 6 hours with an interrogation time of $T = 150$ ms. For $d = 3.2$ mm, the measured drift is suppressed by a factor of about 1.6 as compared to the maximum ion distance.

7.5. Bayesian frequency estimation

In order to speed up the incremental measurement scheme for determining $\Delta\omega(x_1, x_2)$ described in Sec. 7.3, we implement an adaptive scheme for frequency estimation based on a *Bayesian experiment design* algorithm [Mac14, Wie16].

In general, such algorithms control the choice of a measurement parameter, in our particular case the interrogation time, which in each measurement run guarantees the optimum gain of information on the parameter to be determined. These algorithms are beneficial in situations where only a few parameters are to be determined, an accurate model relating the design parameters to the measurement outcome holds, and the measurement is 'expensive' in terms of resources such as time.

In Bayesian statistics, for a given phase measurement to be carried out, the combined result of all previous measurements is expressed with the *prior* probability distribution function (PDF) $p\left(\Delta\omega, \varphi_0\right)$. We initially assume a uniformly distributed prior PDF, limited to a reasonable parameter range $\Delta\omega \in \{\Delta\omega_{\min}, \Delta\omega_{\max}\}$ and $\varphi_0 \in \{-\pi, \pi\}$. The acquired information of a phase measurement combined with all previous knowledge is described by the *posterior* PDF

$$\tilde{p}\left(\Delta\omega, \varphi_0 | n, m; T\right) = \frac{p\left(n, m; T | \Delta\omega, \varphi_0\right) p\left(\Delta\omega, \varphi_0\right)}{p\left(n, m; T\right)} \tag{7.12}$$

Here, n and m describe the outcome of the phase measurement at an interrogation time T, i.e. the number of events where the state has been projected to either $|\uparrow\uparrow\rangle$ or $|\downarrow\downarrow\rangle$ during N and M measurements of the respective operators $\hat{\sigma}_x \otimes \hat{\sigma}_x$ and $\hat{\sigma}_x \otimes \hat{\sigma}_y$. The *update function* $p\left(n, m; T | \Delta\omega, \varphi_0\right)$ is given by the likelihood function of the phase measurement, and the *marginal* PDF $p\left(n, m; T\right)$ ensures normalization of the posterior. A complete theoretical description is given in Appendix B.

The interrogation time T for each phase measurement is calculated such that the expected increase of the Shannon information in the posterior PDF is maximized. With this approach, we observe that the automated measurement operates in two distinct measurement regimes: The measurement starts in the *capture regime*, where T is consecutively increased from $T = 0$ to the desired maximum time $T_{\max}$ in order to unambiguously identify $\Delta\omega$ without any previous information on its value. Then, in the *tracking regime*, the algorithm alternates T between $T_{\max}$ and $T = 0$ for best sensitivity. In order to efficiently track drifts of $\Delta\omega$, we intentionally introduce a 'memory loss' by broadening the prior PDF by about 5% of its width for phase measurements at $T_{\max}$. This facilitates the determination of frequencies that deviate from the previous mean value.

Figure 7.4 visualizes an example measurement. In Fig. 7.4(a), the update functions of the first phase measurements in the capture regime are shown. It can be seen that a single phase measurement alone is not sufficient to estimate $\Delta\omega$. But the combined result of multiple phase measurements yields an approximate Gaussian marginal distribution for $\Delta\omega$, from which the mean value $\langle\Delta\omega\rangle$ and the standard error $\Delta\omega_{\text{err}}$ are inferred.

Figure 7.4(b) depicts the interrogation time T for each experimental cycle and the standard errors of the results versus the total elapsed time of the measurement. In the capture regime, the measurement error scales as $\Delta\omega_{\text{err}} \propto 1/t^{1.8(2)}$, with the elapsed measurement time t. This is a significant improvement over recent high-dynamic-range measurement schemes with fixed interrogation times, in which error scalings close to $1/t$ have been demonstrated [Nus12, Wal12a, Bon16]. The maximum interrogation time is reached after about $t = 12$ min, which is about 10 times faster than in the incremental measurement scheme.

In the tracking regime, the error scaling is reduced to $\Delta\omega_{\text{err}} \propto 1/\sqrt{t}$ and the precision limit given by the magnetic-field inhomogeneity drift rates and the coherence time is approached. A minimum error of $\Delta\omega_{\text{err}} = 2\pi\cdot 2.5$ mHz is obtained. Now, the uncertainty after each measurement is no longer reduced, but the parameter estimates are corrected for drifts, see Fig. 7.4(c).

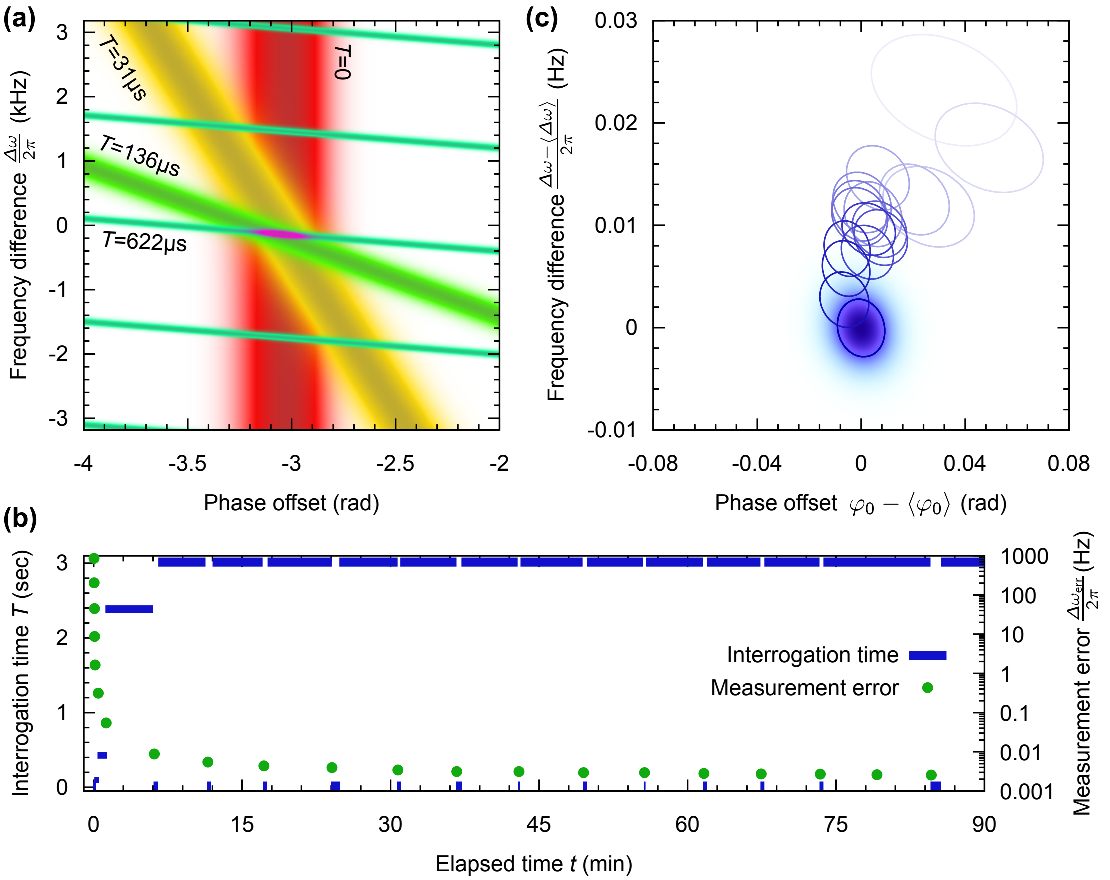

Figure 7.4.: Bayesian evaluation of a measurement at an ion distance of $d = 800$ µm. **(a)** Update functions (colored bars) in $(\Delta\omega, \varphi_0)$-parameter space of the first four phase measurements with $N = M = 50$ repetitions of the experimental procedure, and the posterior PDF (purple ellipse) after these iterations. **(b)** Interrogation times (blue bars) and error of the frequency determination (green points) for each phase measurement versus elapsed measurement time. **(c)** The posterior PDFs at maximum interrogation time for subsequent phase measurements are visualized by open ellipses, corresponding to the 39.4%-credible regions. One can see that in this regime, the measurement is tracking the drift of the magnetic-field difference (see text). The posterior PDF pertaining to the last measurements is indicated as a density plot.

The shot-noise limited sensitivity describes the minimal frequency change that can be discriminated within unit time:

$$S_\omega = \Delta\omega_{\mathrm{err}}\sqrt{T_{\mathrm{tot}}} \tag{7.13}$$

with the standard error of the frequency measurement $\Delta\omega_{\mathrm{err}}$, which has been achieved during a total experimental time of T_{tot} [Tay08]. As the sensitivity depends on the chosen interrogation time, we calculate S_ω separately for each phase measurement, only taking prior knowledge of the phase offset φ_0 into account. At an ion distance of $d = 800$ µm,

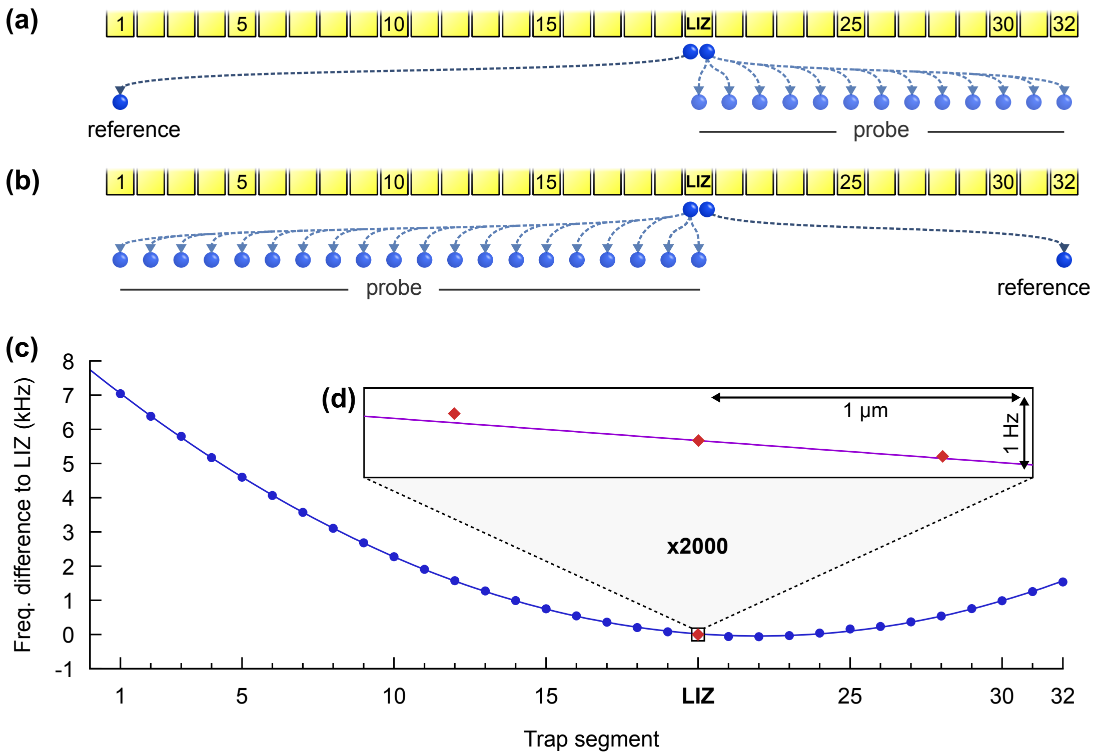

Figure 7.5.: Frequency differences to the laser interaction zone (LIZ). A sensor state is prepared, and the *probe ion* is moved to an arbitrary desired position. At the same time, the *reference ion* is either moved to **(a)** segment 1 or **(b)** segment 32 to maximize the ion distance. The results for each segment are shown in **(c)**. In **(d)**, high precision measurements close to the LIZ yield standard errors for the ion position and frequency difference of about 10 nm and $2\pi \cdot 10$ mHz, respectively.

a best sensitivity of $S_\omega = 2\pi \cdot 116\ \text{mHz}/\sqrt{\text{Hz}}$ is obtained for an interrogation time of $T_{\text{max}} = 3.0$ s. At this interrogation time, a mean contrast C of about 0.94 has been obtained at an average duration of 3.3 s for a single experimental cycle, i.e. about 91% of the measurement time has been utilized for phase accumulation. Thus, our sensitivity is only about 26% higher than the theoretical standard quantum limit of $1/\sqrt{T_{\text{max}}} = 2\pi \cdot 92\ \text{mHz}/\sqrt{\text{Hz}}$ (see Appendix C). The results are on par with recent measurements of AC magnetic fields with single ions [Bau16], only surpassed by sensors with larger dimensions [Was10, Wol15].

We utilize the measurement scheme for mapping the frequency difference $\Delta\omega$ to the laser interaction zone (segment 20) along the trap axis. A frequency measurement is performed for each trap segment, where one ion, the *probe* ion, is moved to the desired segment, and the second *reference* ion is moved to either segment 1, if the probe ion is being moved to segments $20-32$, or to segment 32, if the probe ion is being moved to segments $1-20$ (Figs. 7.5(a) and 7.5(b)). This way, the ion distance is sufficiently large so that the trapping potential of the reference ion does not affect the probe ion position at the given level of accuracy and vice versa. The results are depicted in Fig. 7.5(c). In Fig. 7.5(d), additional measurements close to the laser interaction zone are shown, allowing us to infer frequency gradients with high precision. For reaching spatial accuracies of about 10 nm, the probe-ion position has been calibrated via an EMCCD camera (see Appendix A).

7.6. Separation of DC and AC Zeeman shifts

In addition to the DC Zeeman effect, the energy levels of the sensor state are also shifted by the AC Zeeman effect due to oscillating magnetic fields. This shift is caused by off-resonant driving of the magnetic dipole transition between neighboring magnetic sublevels of a given electronic state [Bud08]. In the present experimental setting, such oscillating magnetic fields are generated by the charging and discharging currents of the RF electrodes of the Paul trap. In an ideal symmetric trap, the equilibrium positions of the ions are located on the nodal line of the RF field, where also the magnetic fields cancel out. However, residual displacement from the RF node due to stray electric fields and trap fabrication imperfections give rise to a position-dependent frequency shift between the populated magnetic sublevels (see Sec. 2.1):

$$\omega^{(\mathrm{ac})}(x) = \Delta m_j \left(g \frac{\mu_\mathrm{B}}{2\hbar} B_{\mathrm{rf},\perp}(x) \right)^2 \frac{\nu(x)}{\nu(x)^2 - \Omega_\mathrm{rf}^2}. \tag{7.14}$$

Here, x is the ion position along the trap axis, $B_{\mathrm{rf},\perp}(x)$ is the component of the oscillating magnetic field perpendicular to the static quantizing magnetic field, $\Omega_\mathrm{rf} = 2\pi \cdot 33$ MHz is the trap drive frequency, and $\nu(x)$ denotes the total (angular) frequency splitting between neighboring ($|\Delta m_j| = 1$) Zeeman sublevels.

For sensor states encoded in different electronic state manifolds, the respective Landé factors lead to different contributions to the total phase accumulation rates from DC and AC fields. Hence, by encoding entangled sensor states within *different* electronic states of $^{40}\mathrm{Ca}^+$, the sensing scheme is extended to distinguish between AC and DC magnetic fields. We utilize the $m_j = \pm 5/2$ sublevels of the metastable $\mathrm{D}_{5/2}$ state in addition to the $\mathrm{S}_{1/2}$ ground state for frequency-difference measurements. The sensor state $|+5/2, -5/2\rangle + |-5/2, +5/2\rangle$ is prepared by first creating the state $|\uparrow\downarrow\rangle + |\downarrow\uparrow\rangle$ and then transferring the populations of both ions to the respective sublevels of the $\mathrm{D}_{5/2}$ metastable state, i.e. $|\uparrow\rangle \rightarrow |+5/2\rangle$ and $|\downarrow\rangle \rightarrow |-5/2\rangle$ (Fig. 7.6(a)). The population transfer is carried out via composite-inversion laser pulses near 729 nm [Fre80]. Considering the Landé factors of both states $g_\mathrm{S} = 2.00225664(9)$ [Tom03] and $g_\mathrm{D} = 1.2003340(3)$ [Chw09], the $\mathrm{D}_{5/2}$ sensor state features phase accumulation rates that are increased by a factor of 3. However, spontaneous decay at a rate of $1/\tau$ *per ion* leads to a reduction of valid measurement cycles, with $\tau = 1.168(7)$ s [Kre05]. An additional fluorescence-detection step before state readout serves to reject measurements where at least one ion has decayed from the $\mathrm{D}_{5/2}$ state. Beyond wait times of $\tau/2$, this postselection reduces the sensitivity of the measurement (Fig. 7.6(b)).

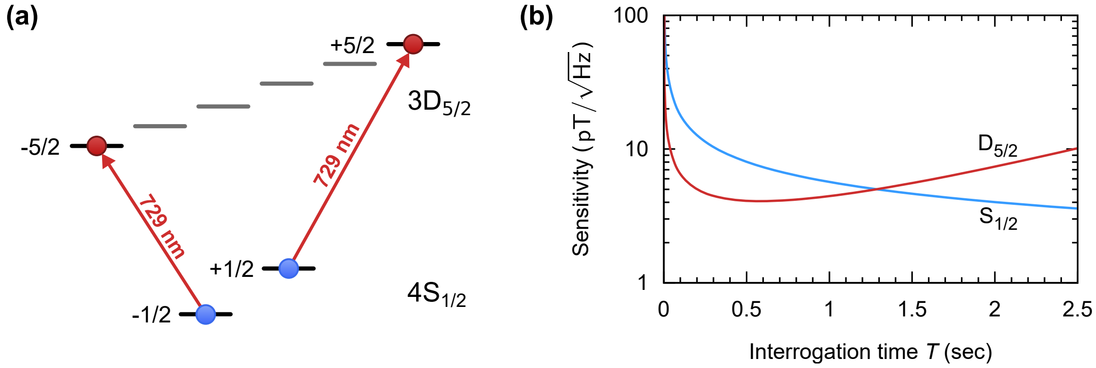

Figure 7.6.: **(a)** Relevant transitions for creating the $D_{5/2}$ sensor state. **(b)** Theoretical shot-noise limited sensitivity of magnetic-field measurements versus interrogation time T for both $S_{1/2}$ and $D_{5/2}$ sensor states, showing how spontaneous decay limits the sensitivity of the $D_{5/2}$ sensor state for long interrogation times (see text).

Measurement of both differential[2] phase accumulation rates $\Delta\omega_S$ and $\Delta\omega_D$ for the respective $S_{1/2}$ and $D_{5/2}$ sensor states allow for disambiguating the static magnetic-field difference and the differential AC Zeeman shift. As the sensor states are affected differently by the static DC Zeeman effect and the AC Zeeman shift, we can infer the magnetic-field difference via (see Appendix E)

$$\Delta B = \frac{\hbar}{\mu_B} \frac{\Delta\omega_D - \chi\Delta\omega_S}{5g_D - \chi g_S}. \tag{7.15}$$

Here, $\chi = \Delta\omega_D^{(ac)}/\Delta\omega_S^{(ac)}$ denotes the ratio of the differential AC Zeeman shifts pertaining to the $D_{5/2}$ and $S_{1/2}$ sensor states. The differential AC Zeeman shift between the constituent ions of the $S_{1/2}$ sensor state is given by

$$\Delta\omega_S^{(ac)} = \Delta\omega_S - g_S \frac{\mu_B}{\hbar}\Delta B. \tag{7.16}$$

Under the approximation that the magnetic-field inhomogeneity is small compared to the absolute magnetic field, i.e. the energy splittings $\nu_S(x)$ and $\nu_D(x)$ of the respective electronic states are constant along the trap axis, χ is calculated via

$$\chi \approx 5\left(\frac{g_D}{g_S}\right)^2 \frac{\nu_D}{\nu_S} \cdot \frac{\nu_S^2 - \Omega_{rf}^2}{\nu_D^2 - \Omega_{rf}^2}. \tag{7.17}$$

This approximation is well fulfilled in our experimental setup.

Experimentally, the phase accumulation rates $\Delta\omega_S$ and $\Delta\omega_D$ are measured by performing alternating experimental cycles on the $S_{1/2}$ and $D_{5/2}$ sensor states. The respective interrogation times T_S and T_D are independently determined by the Bayesian algorithm.

---

[2] All quantities with a 'Δ' denote differences with respect to sensing positions x_1 and x_2, we consistently omit these arguments.

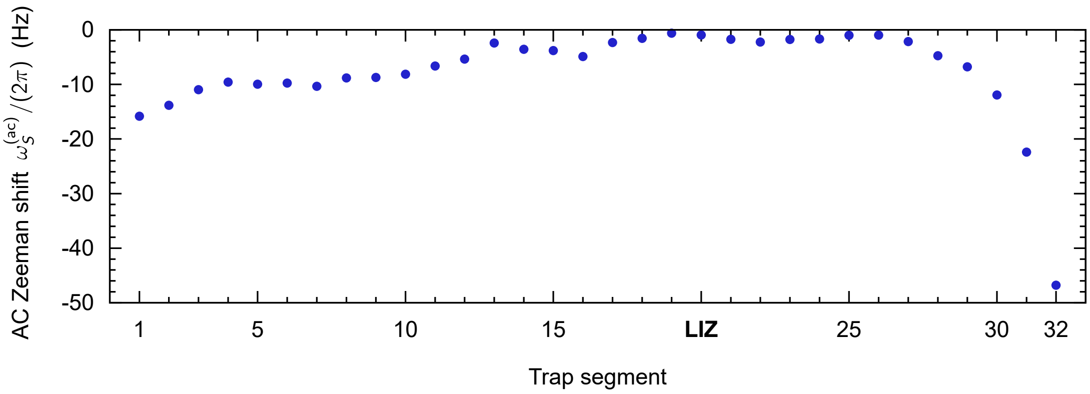

Figure 7.7.: Frequency shift of the $S_{1/2}$ sensor state due to the AC Zeeman effect along the trap axis. Error bars are about $2\pi \cdot 0.2$ Hz for each measurement point. For the parameters in this experimental setup, the AC Zeeman shift is similar for both $S_{1/2}$ and $D_{5/2}$ sensor states.

Additional measurements on a single ion at the laser interaction zone are employed to determine the transition frequencies $\nu_{\mathrm{S}}(x_{\mathrm{LIZ}})$, $\nu_{\mathrm{D}}(x_{\mathrm{LIZ}})$, and the absolute AC Zeeman shift $\omega_{\mathrm{S}}^{(\mathrm{ac})}(x_{\mathrm{LIZ}})$ (see Appendix E). The transition frequencies $\nu_{\mathrm{S}}(x_{\mathrm{LIZ}})$ and $\nu_{\mathrm{D}}(x_{\mathrm{LIZ}})$ are plugged into the AC Zeeman ratio χ (Eq. 7.17), which is used to infer ΔB (Eq. 7.15) and $\Delta\omega_S^{(\mathrm{ac})}$ (Eq. 7.16).

Figure 7.7 depicts the absolute AC Zeeman shift along the trap axis. At the laser interaction zone, an AC Zeeman shift of $\omega_{\mathrm{S}}^{(\mathrm{ac})}(x_{\mathrm{LIZ}}) = -2\pi \cdot 0.93(12)$ Hz is revealed. For remote segments, the magnitude of the frequency shift increases by up to $2\pi \cdot 50$ Hz. This behavior is presumably caused by a displacement of the ions' equilibrium positions from to the nodal line of the RF field, which are minimized only at the laser interaction zone to compensate excess micromotion. For all ion positions, standard errors of about $\omega_{\mathrm{S,err}}^{(\mathrm{ac})} = 2\pi \cdot 0.2$ Hz are reached. Compared to recent measurements of the AC Zeeman shift arising from microwave fields [War13], this is an improvement by three orders of magnitude. Thus, the presented measurement technique may be used to improve the fidelity of microwave-driven quantum gates, where precise mapping of the AC Zeeman shift is important.

For DC magnetic-field differences, precisions as good as $\Delta B_{\mathrm{err}} = 310$ fT are reached at an ion distance of $d = 800$ µm. Here, ΔB_{err} has been determined by applying Gaussian error propagation to Eq. 7.15. Sensitivities down to $S_B = \Delta B_{\mathrm{err}}\sqrt{T_{\mathrm{tot}}} = 12\ \mathrm{pT}/\sqrt{\mathrm{Hz}}$ are attained at interrogation times of $T_{\mathrm{S}} = 1.50$ s and $T_{\mathrm{D}} = 0.48$ s.

7.7. Future applications

We have demonstrated a novel magnetometry scheme harnessing entangled ions, which are freely positioned in a segmented Paul trap. The long coherence time of the entangled states enable precise measurement of DC magnetic-field differences. Combined with the high spatial resolution offered by trapped ions, the accessed parameter regime is so far unique among magnetic-field sensors.

The measurement scheme additionally characterizes the position-dependent AC Zeeman effect due to the RF trap drive in Paul traps, which is a hard-to-characterize source of errors for precision measurements in frequency standards. For recent optical clocks, the AC Zeeman shift contributes to the fractional error in the 10^{-20}-10^{-17} range [Her12, Cho10, Ita07].

Precise knowledge of the magnetic field along the trap axis is essential for a shuttling-based approach towards scalable quantum information experiments in Paul traps. In this approach, quantum algorithms are carried out with multiple ions residing at different trap segments, where different phases are accumulated. These phases have to be taken into account within computational sequences [Kau17b].

The benefits of the presented measurement technique could be harnessed to characterize the magnetic properties of samples that are small compared to the size of the ion trap. In this case, the *absolute* magnetic field of the sample is accessible if the reference ion is placed sufficiently far away. The presented gradiometer could be extended to a full-fledged DC vector magnetometer: By changing the direction of the quantizing magnetic field, the absolute magnetic field of the sample along all directions can be measured. Suitable samples to be probed include additional trapped ions, neutral atoms trapped by optical dipole forces [Sch12], or more complex samples such as single-molecule magnets [Tho96]. In the case of single neutral atoms or cold quantum gases, the absence of coulomb repulsion allows the probe ion to be placed in a nm distance to or within the sample.

For sensing of sample surfaces, the achievable accuracy of our method is limited by increased heating via fluctuating electric fields in the proximity to the surface, which can deteriorate the readout fidelity. This effect however strongly depends on the characteristics of the sample, such as temperature, surface structure, and contamination, where the underlying mechanisms are not yet entirely understood [Bro15].

8 Outlook

This work demonstrates how the fields of quantum sensing and quantum information can massively profit from each other: Fundamental concepts of quantum information, such as deterministic entanglement and quantum phase estimation, have been utilized to realize a highly sensitive magnetic-field probe. Vice versa, quantum sensing is an important tool for characterizing noise sources and systematic errors in quantum computers.

The Ramsey coherence time could be improved in future experiments by either actively stabilizing the temperature of the aluminum rings bearing the magnets or by lowering the temperature dependence of the magnetic field. The latter could be achieved by using materials optimized towards a low temperature coefficient [Cam96, Tak09], or by combining $\mathrm{Sm_2Co_{17}}$ and NdFeB magnets. Since both materials feature different temperature coefficients (about $-0.03\%/^\circ\mathrm{C}$ for $\mathrm{Sm_2Co_{17}}$ and $-0.10\%/^\circ\mathrm{C}$ for NdFeB), magnets of both types can be arranged in such a way that temperature drifts are canceled at the trap location. Such a magnet configuration has already been successfully tested by Nicodemus [Nic17].

The future goal for the presented experimental apparatus is the realization of scalable experiments for quantum information, i.e. algorithms using an increasing number of qubits. All basic operations for controlling few-qubit registers have already been realized: Single and two-qubit gates, ion transport [Wal12b], ion-crystal separation and rotation [Kau17b]. The $1/\sqrt{\mathrm{e}}$ spin-echo coherence time of 2.12(7) s for a single ion enables a large number ($\approx 10^5$) of gate operations [Gae16, Bal16].

The operation of more qubits will enhance the sensitivity of quantum-sensing applications, at the cost of a reduced spatial resolution. This is because the spatial resolution would be limited by the inter-ion distance in an ion crystal instead of the size of the ion's wave function, i.e. about 4 µm instead of about 10 nm. The benefit in using many-qubit states for quantum sensing therefore depends strongly on the application. For measuring the magnetic-field inhomogeneity along the trap axis, Heisenberg-limited scaling of the sensitivity $S \propto 1/N$ can be obtained by using the $2N$-qubit entangled state $\left(|{\downarrow}\rangle^{\otimes N} |{\uparrow}\rangle^{\otimes N} + |{\uparrow}\rangle^{\otimes N} |{\downarrow}\rangle^{\otimes N}\right)/\sqrt{2}$ [Alt17].

Adding more qubits to the system will lead to an increased number of shuttling operations during computational sequences. Currently, multi-segment transports are realized by simply concatenating precalculated single-segment transports, with an acceleration and deceleration phase for each segment. This behavior slows down the overall process, and leads to enhanced motional excitation. When combining ion-crystal separation and transport operations, voltage ramps have to be manually programmed to avoid discontinuities in the trajectories of each ion. Using this approach, the scalable creation of a long-lived four-ion GHZ state $\left(|0000\rangle + |1111\rangle\right)/\sqrt{2}$ has been demonstrated by Kaufmann et al. [Kau17c]. For future experiments, an automated optimization algorithm is under development that will simplify the process of creating voltage ramps, and will speed up multi-segment transports [Nic17]. This is a first step towards a *quantum compiler* [Mar16]. The purpose of a quantum compiler is to find an optimal decomposition of a given quantum algorithm or unitary operation into available gates, taking into account the capabilities of the experimental hardware.

An essential prerequisite for realizing fault-tolerant quantum computing is the implementation of quantum error correction [Ter15], where logical qubits are encoded in entangled states of multiple physical qubits. This way, certain experimental errors can be detected and corrected without affecting the information stored in the logical qubit. In ion traps, a *7-qubit topological color code*, where a logical qubit is encoded in a 7-ion crystal, has already been experimentally realized [Nig14]. Using this code, phase and/or bit flip errors on any of the physical qubits can be detected and corrected. Since the encoding, detection, and correction of existing errors rely on imperfect operations that might introduce new errors, it is experimentally challenging to create a logical qubit that actually outperforms an unprotected single physical qubit. Bermudez et al. [Ber17] give a road-map on how to surpass this break-even point for a 7-qubit color code in segmented ion traps. The experimental requirements may be realizable within the next few years. For certain applications, quantum error correction can also enhance the performance of quantum sensors [Her15, Kes14].

A Ion-position calibration

Here, we describe how to calibrate ion positions along the trap axis with about 10 nm accuracy close to the laser interaction zone. The precise measurement of ion positions is an important step for calibrating the β-coefficients in Sec. 5.1, and for reaching high spatial resolutions in the magnetometry scheme presented in chapter 7.

The ions are imaged to the sensor of an EMCCD camera with a magnification of about 15.6. The sensor of the camera features 128 × 128 pixels, with a size of 24µm × 24µm each. In the first step, we determine the ion displacement (in µm) that corresponds to the size of a single camera pixel. For this purpose, we take advantage of the fact that the inter-ion distance of two $^{40}\mathrm{Ca}^+$ ions in an harmonic potential can be calculated from the oscillation frequency of the axial COM mode: $d = \mathrm{e}^{2/3}\left(2\pi\,\varepsilon_0\,m\,\omega_x^2\right)^{-1/3}$ [Jam98]. The squared oscillation frequency ω_x^2 is experimentally determined by the α-calibration procedure presented in Sec. 5.1. It depends linearly on the DC voltage at the laser interaction zone (Fig. A.1(a)), and is measured via resolved sideband spectroscopy.

Then, the ion distance of a two-ion crystal is varied by changing the DC electrode voltage at the laser interaction zone, and the ion distance (in pixels) is measured on the EMCCD camera. By performing Gaussian fits to the camera images, the ion positions can be determined with sub-pixel resolution (Fig. A.1(b)). A linear fit yields the number of camera pixels per unit length (Fig. A.1(c)), and can be used to infer the ion distance (in µm) near the laser interaction zone for arbitrary camera images.

For measuring inhomogeneous magnetic field with high spatial resolution, the ion positions have to be varied with high spatial resolution as well. Similar to the tilt adjustment presented in Sec. 5.1, a differential DC voltage ΔU_S is applied between the segments adjacent to the laser interaction zone, while a voltage of $U_\mathrm{C} = -6$ V is applied to the laser interaction zone. Close to this zone, the ion position of a single trapped ion depends linearly on the differential voltage (Fig. A.1(d)).

We combine these calibrations and determine the ion displacement in µm versus differential voltage ΔU_S:

$$\frac{\delta x}{\delta(\Delta U_\mathrm{S})} = 15.40(20)\ \frac{\mu\mathrm{m}}{\mathrm{V}} \tag{A.1}$$

When calculating the ion position relative to the laser interaction zone at given ΔU_S, the statistical error of the calibration procedure determines the accuracy of the ion position. For example, at a displacement voltage of $\Delta U_\mathrm{S} = 60$ mV, the ion is displaced by $\delta x = 924(12)$ nm. The displacement is also dependent on the voltage U_C at the laser

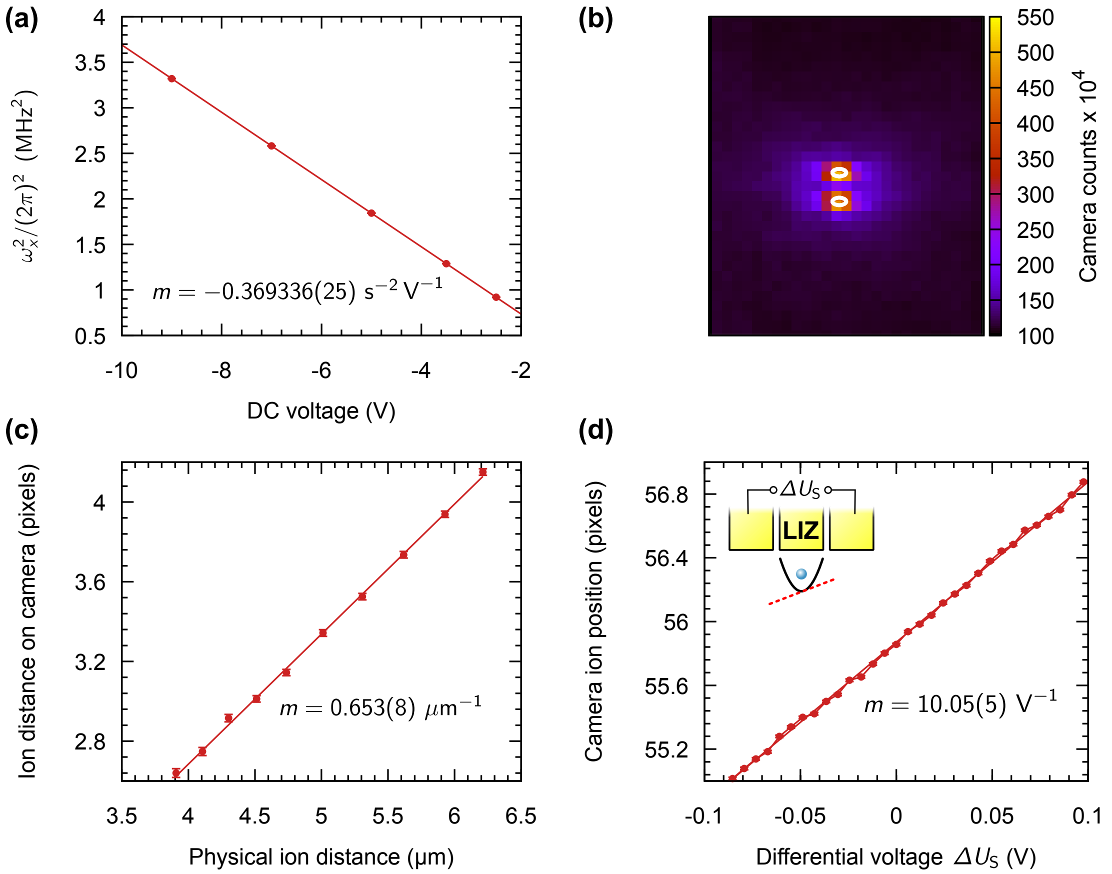

Figure A.1.: Steps towards ion position calibration. The slopes m are inferred from linear fits to the data. **(a)** Squared axial COM oscillation frequency versus DC voltage at the laser interaction zone. **(b)** Example camera image used for distance measurement. White ellipses indicate the σ regions of the Gaussian fit. **(c)** Ion distance measured on the camera versus ion distance determined via the axial trap frequency for varying DC voltages. **(d)** Ion distance on the camera versus differential voltage ΔU_S, with a voltage of -6V applied to the laser interaction zone.

interaction zone: The trap potential is given by $V(x) \approx \alpha_\mathrm{C} U_\mathrm{C} x^2 + \gamma_\mathrm{S} \Delta U_\mathrm{S} x$, and a single ion resides at the minimum position $x_\mathrm{min} = \frac{\gamma_\mathrm{S} \Delta U_\mathrm{S}}{2\alpha_\mathrm{C} U_\mathrm{C}}$.

In addition to the spatial accuracy given by the calibration, the spatial resolution for magnetic-field sensing is limited by the size of the ion's wave packet. For a typical axial trap frequency of 1.5 MHz, the σ-width of the ground state wave function is 13 nm.

B Bayesian frequency estimation

A phase measurement with the sensor state $|\psi(\varphi)\rangle = \left(|{\uparrow\downarrow}\rangle + \mathrm{e}^{\mathrm{i}\varphi}\,|{\downarrow\uparrow}\rangle\right)/\sqrt{2}$ consists of $\{N, M\}$ measurements of the respective operators $\hat{\sigma}_x \otimes \hat{\sigma}_x$ and $\hat{\sigma}_x \otimes \hat{\sigma}_y$. The outcome of the measurement is described by the parity of the projected state, i.e. the number of events $\{n, m\}$ in which the state has been projected to either $|{\uparrow\uparrow}\rangle$ or $|{\downarrow\downarrow}\rangle$.

In Bayesian statistics, the result of a phase measurement, combined with all previous knowledge, is described by the *posterior* PDF

$$\tilde{p}\left(\Delta\omega, \varphi_0 | n, m; T\right) = \frac{p\left(n, m; T | \Delta\omega, \varphi_0\right) p\left(\Delta\omega, \varphi_0\right)}{p\left(n, m; T\right)} \tag{B.1}$$

with the *update function*

$$p\left(n, m; T | \Delta\omega, \varphi_0\right) = \int_0^1 L\left(n, m; \varphi(\Delta\omega, \varphi_0, T), C\right) \, \mathrm{d}C. \tag{B.2}$$

The *marginal* PDF

$$p\left(n, m; T\right) = \int\int p\left(n, m; T | \Delta\omega, \varphi_0\right) p\left(\Delta\omega, \varphi_0\right) \mathrm{d}\Delta\omega \, \mathrm{d}\varphi_0. \tag{B.3}$$

ensures normalization of the posterior. Equation B.1 is known as *Bayes' rule.* The likelihood function describing the phase measurement is given by

$$L\left(n, m; \varphi, C\right) = p_{xx}^{(\mathrm{E})n}(1 - p_{xx}^{(\mathrm{E})})^{N-n} p_{xy}^{(\mathrm{E})m}(1 - p_{xy}^{(\mathrm{E})})^{M-m} \tag{B.4}$$

with the expectation values of the projective measurements

$$p_{xx}^{(\mathrm{E})} = \frac{1}{2}\left(1 + C\cos\left(\varphi\right)\right) \tag{B.5}$$

$$p_{xy}^{(\mathrm{E})} = \frac{1}{2}\left(1 - C\sin\left(\varphi\right)\right). \tag{B.6}$$

For each parameter set $(\Delta\omega, \varphi_0)$, the accumulated phase after the interrogation time T is given by

$$\varphi(\Delta\omega, \varphi_0, T) = \Delta\omega \cdot T + \varphi_0 \tag{B.7}$$

Because of the phase periodicity, the update function features a $2\pi/T$ periodicity in $\Delta\omega$. But if the width of the prior PDF is smaller than the periodicity of the update function, the periodicity is not inherited by the posterior PDF. After at least two phase measurements at different interrogation times, the posterior PDF is well described by a two-dimensional normal distribution. We obtain estimates for $\Delta\omega$ and φ_0 by calculating expectation values from the marginalized PDF:

$$\langle \Delta\omega \rangle = \int\int \Delta\omega \cdot \tilde{p}\left(\Delta\omega, \varphi_0 | n, m; T\right) \mathrm{d}\Delta\omega \, \mathrm{d}\varphi_0 \tag{B.8}$$

$$\langle \varphi_0 \rangle = \int\int \varphi_0 \cdot \tilde{p}\left(\Delta\omega, \varphi_0 | n, m; T\right) \mathrm{d}\Delta\omega \, \mathrm{d}\varphi_0 \tag{B.9}$$

Standard errors are obtained in a similar fashion by calculating the corresponding standard deviations.

In order to calculate the interrogation time T for the next measurement to be performed, we employ Bayes' rule (Eq. B.1) to calculate the posterior PDF for a *hypothetical* measurement result $\{n, m\}$ at interrogation time T with fixed contrast $C = C_0$, i.e. with the simplified update function $p\left(n, m; T | \Delta\omega, \varphi_0\right) = L\left(n, m; \varphi(\Delta\omega, \varphi_0, T), C_0\right)$. Here, it is sufficient to consider the case of $N = M = 1$ to save computational effort. Because we are interested in minimizing the error in $\Delta\omega$, we marginalize

$$\tilde{p}\left(\Delta\omega\right) := \int \tilde{p}\left(\Delta\omega, \varphi_0 | n, m; T\right) \mathrm{d}\varphi_0. \tag{B.10}$$

Utility is defined as the expected gain in Shannon information of the posterior with respect to the prior after a hypothetical measurement

$$U\left(n, m; T\right) = \int \tilde{p}\left(\Delta\omega\right) \log \tilde{p}\left(\Delta\omega\right) \mathrm{d}\Delta\omega - U_0, \tag{B.11}$$

with the Shannon information of the marginalized prior PDF

$$U_0 = \int p\left(\Delta\omega\right) \log p\left(\Delta\omega\right) \mathrm{d}\Delta\omega. \tag{B.12}$$

Then, we average the utility function over all possible measurement results, weighted with the respective marginal probability:

$$U(T) = \sum_{n=0}^{N} \sum_{m=0}^{M} w(T) \cdot U\left(n, m; T\right) \; p(n, m; T) \tag{B.13}$$

Here, a penalty factor $w(T) = D(0)/D(T)$ takes the increased measurement duration for longer interrogation times into account, where $D(T)$ is the duration of a single experimental run with a given T. The ideal interrogation time for an upcoming measurement is $T_0 = \max_T U(T)$, i.e. T_0 maximizes the expected gain in Shannon information. Via the known results from the prior PDF $\langle \Delta\omega \rangle$ and $\langle \varphi_0 \rangle$, we add a phase offset to the second $\hat{\sigma}_x$ or $\hat{\sigma}_y$ analysis pulse, so that the measured phase is always close to $\pi/4$. Near $\pi/4$, the error bar of a single phase measurement is minimized (at the expense of an increased contrast uncertainty).

C Standard quantum limit

In this chapter, we derive the theoretical sensitivity for frequency measurements that can be achieved if quantum projection noise is the only experimental limitation. This sensitivity is known as the standard quantum limit.

C.1. Single-operator scheme

We first consider the case of a single-ion Ramsey-type measurement, where only measurements of the $\hat{\sigma}_x$-operator are performed. This *single-operator scheme* is suited for frequency measurement if the phase contrast C is known and constant.

The probability p to detect an ion as 'bright' depends on the accumulated phase φ via

$$p = \frac{C}{2}\cos(\varphi) + \frac{1}{2} \tag{C.1}$$

with the contrast C (Fig. C.1(a)). This expression is similar to $p_{xx}^{(\mathrm{E})}$ for the entangled sensor state, and therefore the following derivation is valid for Ramsey-type measurements on a single ion *and* the entangled sensor state.

Best sensitivity is achieved at the maximum slope, i.e. in the case of $p = 0.5$. The standard error for a population measurement at the maximum slope is given by binomial

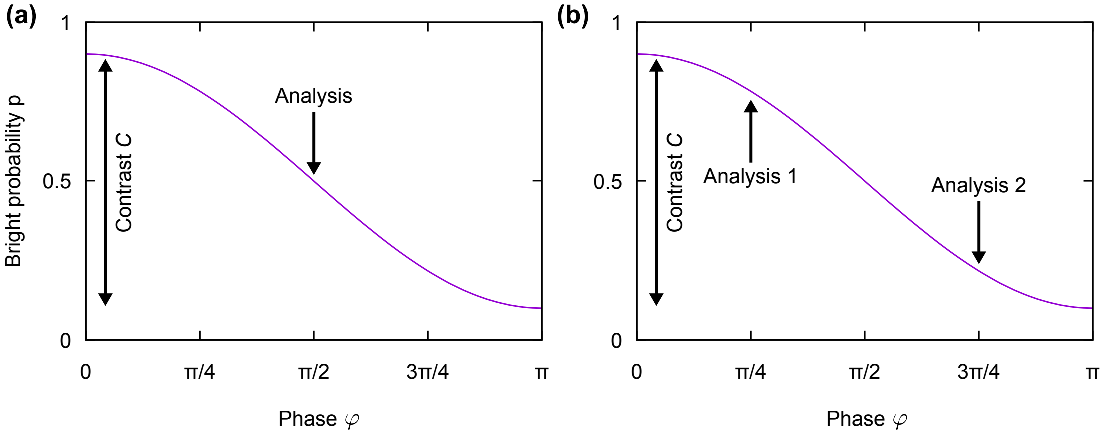

Figure C.1.: Optimal measurement phases for **(a)** the single-operator scheme, and **(b)** the double-operator scheme.

statistics: $\Delta p = \frac{1}{2}\frac{1}{\sqrt{N}}$, with N the number of experimental cycles. The slope is calculated by $\frac{\mathrm{d}p}{\mathrm{d}\varphi}|_{p=0.5} = \frac{C}{2}$. Gaussian error propagation yields the phase error

$$\Delta\varphi = \frac{2}{C}\Delta p = \frac{1}{C\sqrt{N}}. \tag{C.2}$$

The phase is transformed to a frequency via $\omega = \varphi/T$. The sensitivity of a frequency measurement is given by

$$S_\omega = \Delta\omega\sqrt{T_\text{tot}} \tag{C.3}$$

with $\Delta\omega$ the error of the frequency determination and $\sqrt{T_\text{tot}}$ the total measurement time for attaining this frequency error. In an ideal measurement, the total measurement time is fully consumed by the interrogation time T, i.e. $T_\text{tot} = N \cdot T$. The sensitivity is therefore written as

$$S_\omega = \Delta\omega\sqrt{N \cdot T} = \frac{\Delta\varphi}{T}\sqrt{N \cdot T} = \frac{1}{C\sqrt{T}}. \tag{C.4}$$

For $C = 1$, we obtain the standard quantum limit $S_\omega = 1/\sqrt{T}$.

C.2. Double-operator scheme

In this thesis, phase measurements are performed by probing both $\hat{\sigma}_x$ and $\hat{\sigma}_y$ operators. Rotations to the $\hat{\sigma}_y$ basis are performed by adding a phase offset of $\pi/2$ to the respective analysis pulse (Fig. C.1(b)). This scheme is better suited if the phase contrast C is unknown or drifts over time.

Best sensitivity is achieved at the respective populations of $p_1 = \frac{C}{2}\cos(\frac{\pi}{4}) + \frac{1}{2} = \frac{C}{2\sqrt{2}} + \frac{1}{2}$ and $p_2 = \frac{C}{2}\cos(\frac{\pi}{4} + \frac{\pi}{2}) + \frac{1}{2} = -\frac{C}{2\sqrt{2}} + \frac{1}{2}$. Binomial statistics yield a population error of $\Delta p = \sqrt{(\frac{1}{4} - \frac{C^2}{8})/N}$ for both measurements. The phase is inferred via

$$\varphi = \arctan\left(\frac{p_1 - \frac{1}{2}}{p_2 - \frac{1}{2}}\right), \tag{C.5}$$

with the standard error given by Gaussian error propagation:

$$\Delta\varphi = \sqrt{\left(\frac{\partial\varphi}{\partial p_1}\Delta p\right)^2 + \left(\frac{\partial\varphi}{\partial p_2}\Delta p\right)^2} = \frac{2}{C}\Delta p = \frac{2}{C}\sqrt{\left(\frac{1}{4} - \frac{C^2}{8}\right)/N} = \sqrt{\left(\frac{1}{C^2} - \frac{1}{2}\right)/N} \tag{C.6}$$

Next, we calculate the sensitivity of a frequency measurement. Since measurements in the $\hat{\sigma}_x$ *and* $\hat{\sigma}_y$ bases are performed, the measurement duration T_tot is doubled. We obtain

$$S_\omega = \Delta\omega\sqrt{2N \cdot T} = \frac{\Delta\varphi}{T}\sqrt{2N \cdot T} = \sqrt{\left(\frac{2}{C^2} - 1\right)/T} \tag{C.7}$$

For $C = 1$, the standard quantum limit of $S_\omega = \frac{1}{\sqrt{T}}$ is reached as well. However, the sensitivity of the double-operator scheme suffers more from contrast loss than the single-operator scheme.

D Optimal interrogation time

The Bayesian algorithm presented in Sec. 7.5 does not take contrast decay during the interrogation time T into account and therefore relies on a predefined maximum interrogation time. Here, we calculate the optimal T for best sensitivity of a frequency measurement in the case of a Gaussian contrast decay $C(T) = \exp\left(-\frac{T^2}{2\tau^2}\right)$. The result can then be plugged into the maximum interrogation time T_{max} of the Bayesian algorithm.

We first discuss the case of a single-operator measurement (see Appendix C). The sensitivity is given by

$$S_\omega(T) = \frac{1}{C(T)\sqrt{T}}. \tag{D.1}$$

We insert a Gaussian contrast decay into this expression and obtain

$$S_\omega(T) = \frac{\exp\left(\frac{T^2}{2\tau^2}\right)}{\sqrt{T}}. \tag{D.2}$$

The sensitivity is minimized for $T = \frac{\tau}{\sqrt{2}}$, equivalent to a contrast decay to $C \approx 0.78$. This result differs significantly from the case of exponential contrast decay, where the contrast corresponding to the optimal interrogation time is $C_{\text{exp}} \approx 0.61$.

For the double-operator measurement scheme, the sensitivity is

$$S_\omega(T) = \sqrt{\left(\frac{2}{C(T)^2} - 1\right) / T}. \tag{D.3}$$

Inserting a Gaussian contrast decay yields

$$S_\omega(T) = \sqrt{\left(2 \cdot \exp\left(\frac{T^2}{\tau^2}\right) - 1\right) / T}. \tag{D.4}$$

The optimal interrogation time $T \approx 0.57\,\tau$ pertains to a contrast loss of about 85%. Since Gaussian contrast decay is observed in the experiment, the maximum interrogation time for the frequency estimation scheme is chosen accordingly. For an ion distance of $d = 800$ µm, the optimal interrogation time is about 3 s.

E Separation of DC and AC magnetic fields

E.1. Calculation from experimental quantities

In the experiment, both DC and AC Zeeman shifts depend on the ion positions. We measure *differences* of atomic frequency splittings between two locations x_1 and x_2 along the trap axis of a linear segmented ion trap. In order to distinguish the DC and AC Zeeman frequency shifts, we measure the differential phase accumulation rates in the $\mathrm{S}_{1/2}$ ground state with $\Delta m = 1$ and in the $\mathrm{D}_{5/2}$ metastable state with $\Delta m = 5$, given by

$$\Delta\omega_{\mathrm{S}}(x_1, x_2) = \frac{g_{\mathrm{S}}\mu_{\mathrm{B}}}{\hbar}\Delta B(x_1, x_2) + \Delta\omega_{\mathrm{S}}^{(\mathrm{ac})}(x_1, x_2) \tag{E.1}$$

$$\Delta\omega_{\mathrm{D}}(x_1, x_2) = \frac{5g_{\mathrm{D}}\mu_{\mathrm{B}}}{\hbar}\Delta B(x_1, x_2) + \Delta\omega_{\mathrm{D}}^{(\mathrm{ac})}(x_1, x_2) \tag{E.2}$$

with $\Delta B(x_1, x_2) = B(x_1) - B(x_2)$ and $\Delta\omega_J^{(\mathrm{ac})}(x_1, x_2) = \omega_J^{(\mathrm{ac})}(x_1) - \omega_J^{(\mathrm{ac})}(x_2)$. Here, J denotes the electronic state ($J \equiv \mathrm{S}$ for the $\mathrm{S}_{1/2}$ state, and $J \equiv \mathrm{D}$ for the $\mathrm{D}_{5/2}$ state). To obtain the static magnetic-field difference, we write Eq. E.2 as

$$\Delta\omega_{\mathrm{D}}(x_1, x_2) = \frac{5g_{\mathrm{D}}\mu_{\mathrm{B}}}{\hbar}\Delta B(x_1, x_2) + \chi\Delta\omega_{\mathrm{S}}^{(\mathrm{ac})}(x_1, x_2) \tag{E.3}$$

with the AC Zeeman difference ratio

$$\chi \equiv \Delta\omega_{\mathrm{D}}^{(\mathrm{ac})}(x_1, x_2)/\Delta\omega_{\mathrm{S}}^{(\mathrm{ac})}(x_1, x_2). \tag{E.4}$$

We insert Eq. E.1 into Eq. E.3 and solve for the static magnetic-field difference

$$\Delta B(x_1, x_2) = \frac{\hbar}{\mu_{\mathrm{B}}}\frac{\Delta\omega_{\mathrm{D}}(x_1, x_2) - \chi\Delta\omega_{\mathrm{S}}(x_1, x_2)}{5g_{\mathrm{D}} - \chi g_{\mathrm{S}}}. \tag{E.5}$$

To extract $\Delta\omega_J^{(\mathrm{ac})}(x_1, x_2)$ from measurements, we insert Eq. E.5 into Eq. E.1 or E.2 and obtain

$$\Delta\omega_J^{(\mathrm{ac})}(x_1, x_2) = \Delta\omega_J(x_1, x_2) - \Delta m\, g_J\frac{\Delta\omega_{\mathrm{D}}(x_1, x_2) - \chi\Delta\omega_{\mathrm{S}}(x_1, x_2)}{5g_{\mathrm{D}} - \chi g_{\mathrm{S}}}. \tag{E.6}$$

Using Eq. 2.27, the AC Zeeman difference ratio is given by

$$\chi(x_1, x_2) = \frac{\Delta\omega_{\mathrm{D}}^{(\mathrm{ac})}(x_1, x_2)}{\Delta\omega_{\mathrm{S}}^{(\mathrm{ac})}(x_1, x_2)} = 5\left(\frac{g_{\mathrm{D}}}{g_{\mathrm{S}}}\right)^2 \frac{B_{\mathrm{rf},\perp}(x_1)^2\frac{\nu_{\mathrm{D}}(x_1)}{\nu_{\mathrm{D}}(x_1)^2-\Omega_{\mathrm{rf}}^2} - B_{\mathrm{rf},\perp}(x_2)^2\frac{\nu_{\mathrm{D}}(x_2)}{\nu_{\mathrm{D}}(x_2)^2-\Omega_{\mathrm{rf}}^2}}{B_{\mathrm{rf},\perp}(x_1)^2\frac{\nu_{\mathrm{S}}(x_1)}{\nu_{\mathrm{S}}(x_1)^2-\Omega_{\mathrm{rf}}^2} - B_{\mathrm{rf},\perp}(x_2)^2\frac{\nu_{\mathrm{S}}(x_2)}{\nu_{\mathrm{S}}(x_2)^2-\Omega_{\mathrm{rf}}^2}}. \tag{E.7}$$

Here, both the total absolute frequency splittings $\nu_J(x)$ and oscillating magnetic fields $B_{\mathrm{rf},\perp}(x)^2$ are position-dependent. As an approximation, we discard the dependence on the position:

$$\nu_J(x) \approx \nu_J(x_{\mathrm{LIZ}}), \tag{E.8}$$

where $\nu_J(x_{\mathrm{LIZ}})$ denotes the *absolute* frequency splitting at the laser interaction zone (LIZ). Now, Eq. E.7 simplifies to

$$\chi \approx 5\left(\frac{g_{\mathrm{D}}}{g_{\mathrm{S}}}\right)^2 \frac{\nu_{\mathrm{D}}(x_{\mathrm{LIZ}})}{\nu_{\mathrm{S}}(x_{\mathrm{LIZ}})} \cdot \frac{\nu_{\mathrm{S}}(x_{\mathrm{LIZ}})^2 - \Omega_{\mathrm{rf}}^2}{\nu_{\mathrm{D}}(x_{\mathrm{LIZ}})^2 - \Omega_{\mathrm{rf}}^2}. \tag{E.9}$$

With values for $\nu_{\mathrm{S,D}}(x_{\mathrm{LIZ}})$ available, we can determine a value for χ, which can be inserted into Eqs. E.5 and E.6 to obtain the desired quantities.

E.2. Error characterization

To compute a value for χ according to Eq. E.9, the required values for the total frequency splittings at the laser interaction zone $\nu_{\mathrm{S,D}}(x_{\mathrm{LIZ}})$ are obtained from direct laser spectroscopy on a single ion. For $J = \mathrm{S}$, spectroscopy is carried out on the stimulated Raman transition, while for $J = \mathrm{D}$, the $\mathrm{S}_{1/2} \leftrightarrow \mathrm{D}_{5/2}$ quadrupole transition is utilized. In both cases, an interrogation time of 200 μs yields an accuracy of better than $2\pi \cdot 1$ kHz. We therefore obtain $\nu_{\mathrm{S}}(x_{\mathrm{LIZ}}) = 2\pi \cdot 10.2136(10)$ MHz, $\nu_{\mathrm{D}}(x_{\mathrm{LIZ}}) = 2\pi \cdot 6.1231(6)$ MHz, and hence $\chi = 1.00946(16)$. Since the absolute frequency splittings exceed their inhomogeneities along the trap axis by more than 3 orders of magnitude, it is justified to discard the position dependence in Eq. E.8.

The relative accuracy of the magnetic-field difference is reduced with respect to the bare measurements of differential phase accumulation rates, as ΔB according to Eq. E.5 is affected by statistical uncertainties of $\Delta\omega_{\mathrm{S}}, \Delta\omega_{\mathrm{D}}$ and χ. Gaussian error propagation yields relative uncertainties which are increased by a factor of about 2 as compared to the differential frequency measurements.

In the following, we further analyze the validity of the approximation Eq. E.8. To this end, we compare the AC Zeeman ratio from the approximation Eq. E.9 to a self-consistent estimate from the exact expression Eq. E.7. For the latter, we obtain the local frequency splittings $\nu_J(x)$ via

$$\nu_J(x) = \Delta\omega_J(x, x_{\mathrm{LIZ}})/\Delta m_J + \nu_J(x_{\mathrm{LIZ}}) \tag{E.10}$$

In order to obtain estimates for $B_{\mathrm{rf},\perp}(x)^2$, we first compute the absolute AC Zeeman splittings at the laser interaction zone $\omega_J^{(\mathrm{ac})}(x_{\mathrm{LIZ}})$ from the single-ion version of Eq. E.6:

$$\omega_J^{(\mathrm{ac})}(x_{\mathrm{LIZ}}) = \omega_J(x_{\mathrm{LIZ}}) - \Delta m\, g_J \frac{\omega_{\mathrm{D}}(x_{\mathrm{LIZ}}) - \chi\omega_{\mathrm{S}}(x_{\mathrm{LIZ}})}{5g_{\mathrm{D}} - \chi g_{\mathrm{S}}}. \tag{E.11}$$

Here, we employ χ from expression Eq. E.9, which is *exact* for the single-ion case. Now, using

$$\omega_J^{(ac)}(x) = \Delta\omega_J^{(\mathrm{ac})}(x, x_{\mathrm{LIZ}}) + \omega_J^{(\mathrm{ac})}(x_{\mathrm{LIZ}}), \tag{E.12}$$

we obtain the inhomogeneous AC magnetic field according to Eq. 2.27:

$$B_{\mathrm{rf},\perp}(x)^2 = \frac{\omega_J^{(\mathrm{ac})}(x)}{\Delta m}\left(\frac{2\hbar}{g\mu_{\mathrm{B}}}\right)^2 \frac{\nu_J(x)^2 - \Omega_{\mathrm{rf}}^2}{\nu_J(x)}. \tag{E.13}$$

Inserting the results from Eqs. E.10,E.13 into Eq. E.7, we obtain position dependent values for $\chi(x_1, x_2)$. Comparing resulting values of $\Delta B(x_1, x_2)$ and $\Delta\omega_J^{(\mathrm{ac})}(x_1, x_2)$, we find deviations of less than 1% of the statistical uncertainty across the entire region of interest. We therefore conclude that Eq. E.9 is an excellent approximation.

F List of publications

Publications presented in this thesis

Entanglement-Based dc Magnetometry with Separated Ions
T. Ruster, H. Kaufmann, M. A. Luda, V. Kaushal, C. T. Schmiegelow, F. Schmidt-Kaler, and U. G. Poschinger
Physical Review X **7**, 031050 (2017)

A long-lived Zeeman trapped-ion qubit
T. Ruster, C. T. Schmiegelow, H. Kaufmann, C. Warschburger, F. Schmidt-Kaler, and U. G. Poschinger
Applied Physics B **122**, 254 (2016)

Experimental realization of fast ion separation in segmented Paul traps
T. Ruster, C. Warschburger, H. Kaufmann, C. T. Schmiegelow, A. Walther, M. Hettrich, A. Pfister, V. Kaushal, F. Schmidt-Kaler, and U. G. Poschinger
Physical Review A **90**, 033410 (2014)

Other publications

Scalable creation of long-lived multipartite entanglement
H. Kaufmann, T. Ruster, C. Schmiegelow, M. Luda, V. Kaushal, J. Schulz, D. von Lindenfels, F. Schmidt-Kaler, and U. Poschinger
Physical Review Letters **119**, 150503 (2017)

Fast ion swapping for quantum-information processing
H. Kaufmann, T. Ruster, C. T. Schmiegelow, M. A. Luda, V. Kaushal, J. Schulz, D. von Lindenfels, F. Schmidt-Kaler, and U. G. Poschinger
Physical Review A **95**, 052319 (2017)

Transfer of optical orbital angular momentum to a bound electron
C. T. Schmiegelow, J. Schulz, H. Kaufmann, T. Ruster, U. G. Poschinger and F. Schmidt-Kaler
Nature Communications **7**, 12998 (2016)

Cryogenic setup for trapped ion quantum computing
M. F. Brandl, M. W. van Mourik, L. Postler, A. Nolf, K. Lakhmanskiy, R. R. Paiva, S. Möller, N. Daniilidis, H. Häffner, V. Kaushal, T. Ruster, C. Warschburger, H. Kaufmann, U. G. Poschinger, F. Schmidt-Kaler, P. Schindler, T. Monz, R. Blatt
Review of Scientific Instruments **87**, 113103 (2016)

Phase-Stable Free-Space Optical Lattices for Trapped Ions
C. T. Schmiegelow, H. Kaufmann, T. Ruster, J. Schulz, V. Kaushal, M. Hettrich, F. Schmidt-Kaler, and U. G. Poschinger
Physical Review Letters **116**, 033002 (2016)

Measurement of Dipole Matrix Elements with a Single Trapped Ion
M. Hettrich, T. Ruster, H. Kaufmann, C. F. Roos, C. T. Schmiegelow, F. Schmidt-Kaler, and U. G. Poschinger
Physical Review Letters **115**, 143003 (2015)

Dynamics and control of fast ion crystal splitting in segmented Paul traps
H. Kaufmann, T. Ruster, C. T. Schmiegelow, F. Schmidt-Kaler, and U. G. Poschinger
New Journal of Physics **16**, 073012 (2014)

G Bibliography

[Alt17] S. Altenburg, M. Oszmaniec, S. Wölk, and O. Gühne. *Estimation of gradients in quantum metrology*. Phys. Rev. A **96**, 042319 (2017) (cit. on p. 95).

[Ang15] A. Angerer, T. Nöbauer, G. Wachter, M. Markham, A. Stacey, J. Majer, J. Schmiedmayer, and M. Trupke. *Subnanotesla quantum-interference magnetometry with a single spin in diamond* (2015). arXiv: `1509.01637 [quant-ph]` (cit. on p. 18).

[Bai13] M. T. Baig, M. Johanning, A. Wiese, S. Heidbrink, M. Ziolkowski, and C. Wunderlich. *A scalable, fast, and multichannel arbitrary waveform generator*. Rev. Sci. Instrum. **84**, 124701 (2013) (cit. on p. 70).

[Bal08] G. Balasubramanian, I. Y. Chan, R. Kolesov, M. Al-Hmoud, J. Tisler, C. Shin, C. Kim, A. Wojcik, P. R. Hemmer, A. Krueger, T. Hanke, A. Leitenstorfer, R. Bratschitsch, F. Jelezko, and J. Wrachtrup. *Nanoscale imaging magnetometry with diamond spins under ambient conditions*. Nature **455**, 648–651 (2008) (cit. on p. 18).

[Bal12] M. Bal, C. Deng, J.-L. Orgiazzi, F. R. Ong, and A. Lupascu. *Ultrasensitive magnetic field detection using a single artificial atom*. Nat. Commun. **3**, 1324 (2012) (cit. on p. 17).

[Bal14] C. J. Ballance. *High-Fidelity Quantum Logic in Ca^+*. dissertation. University of Oxford, 2014 (cit. on p. 37).

[Bal16] C. J. Ballance, T. P. Harty, N. M. Linke, M. A. Sepiol, and D. M. Lucas. *High-Fidelity Quantum Logic Gates Using Trapped-Ion Hyperfine Qubits*. Phys. Rev. Lett. **117**, 060504 (2016) (cit. on p. 95).

[Bar04] M. D. Barrett, J. Chiaverini, T. Schaetz, J. Britton, W. M. Itano, J. D. Jost, E. Knill, C. Langer, R. Ozeri, and D. J. Wineland. *Deterministic quantum teleportation of atomic qubits*. Nature **429**, 737 (2004) (cit. on p. 15).

[Bar13] N. Bar-Gill, L. M. Pham, A. Jarmola, D. Budker, and R. L. Walsworth. *Solid-state electronic spin coherence time approaching one second*. Nat. Commun. **4**, 1743 (2013) (cit. on p. 16).

[Bar96] P. J. Bardroff, C. Leichtle, G. Schrade, and W. P. Schleich. *Endoscopy in the Paul Trap: Measurement of the Vibratory Quantum State of a Single Ion*. Phys. Rev. Lett. **77**, 2198–2201 (1996) (cit. on p. 26).

[Bau16] I. Baumgart, J.-M. Cai, A. Retzker, M. B. Plenio, and C. Wunderlich. *Ultrasensitive Magnetometer using a Single Atom*. Phys. Rev. Lett. **116**, 240801 (2016) (cit. on pp. 17, 18, 90).

[Ben08] J. Benhelm, G. Kirchmair, C. F. Roos, and R. Blatt. *Experimental quantum-information processing with $^{43}Ca^+$ ions*. Phys. Rev. A **77**, 062306 (2008) (cit. on p. 15).

[Ber17] A. Bermudez, X. Xu, R. Nigmatullin, J. O'Gorman, V. Negnevitsky, P. Schindler, T. Monz, U. G. Poschinger, C. Hempel, J. Home, F. Schmidt-Kaler, M. Biercuk, R. Blatt, S. Benjamin, and M. Müller. *Assessing the progress of trapped-ion processors towards fault-tolerant quantum computation* (2017). arXiv: `1705.02771 [quant-ph]` (cit. on p. 96).

[Bie09] M. J. Biercuk, H. Uys, A. P. VanDevender, N. Shiga, W. M. Itano, and J. J. Bollinger. *Optimized dynamical decoupling in a model quantum memory*. Nature **458**, 996–1000 (2009) (cit. on p. 16).

[Bie11] M. J. Biercuk, A. C. Doherty, and H. Uys. *Dynamical decoupling sequence construction as a filter-design problem*. J. Phys B: At. Mol. Opt. Phys. **44**, 154002 (2011) (cit. on p. 16).

[Bjö07] M. T. Björk, O. Hayden, H. Schmid, H. Riel, and W. Riess. *Vertical surround-gated silicon nanowire impact ionization field-effect transistors*. Appl. Phys. Lett. **90**, 142110 (2007) (cit. on p. 10).

[Bla01] E. D. Black. *An introduction to Pound–Drever–Hall laser frequency stabilization*. Am. J. Phys. **69**, 79–87 (2001) (cit. on p. 50).

[Bla15] S. M. Blakley, I. V. Fedotov, S. Y. Kilin, and A. M. Zheltikov. *Room-temperature magnetic gradiometry with fiber-coupled nitrogen-vacancy centers in diamond*. Opt. Lett. **40**, 3727–3730 (2015) (cit. on p. 18).

[Bol85] J. J. Bollinger, J. D. Prestage, W. M. Itano, and D. J. Wineland. *Laser-Cooled-Atomic Frequency Standard*. Phys. Rev. Lett. **54**, 1000–1003 (1985) (cit. on p. 15).

[Bon16] C. Bonato, M. S. Blok, H. T. Dinani, D. W. Berry, M. L. Markham, D. J. Twitchen, and R. Hanson. *Optimized quantum sensing with a single electron spin using real-time adaptive measurements*. Nat. Nanotechnol. **11**, 247–252 (2016) (cit. on pp. 85, 88).

[Bor00] J. Bork, H. D. Hahlbohm, R. Klein, and A. Schnabel. *The 8-layered magnetically shielded room of the PTB: Design and construction*. Biomag. (2000) (cit. on p. 80).

[Bou97] D. Bouwmeester, J.-W. Pan, K. Mattle, M. Eibl, H. Weinfurter, and A. Zeilinger. *Experimental quantum teleportation*. Nature **390**, 575–579 (1997) (cit. on p. 11).

[Bow12] R. Bowler, J. Gaebler, Y. Lin, T. R. Tan, D. Hanneke, J. D. Jost, J. P. Home, D. Leibfried, and D. J. Wineland. *Coherent Diabatic Ion Transport and Separation in a Multizone Trap Array*. Phys. Rev. Lett. **109**, 080502 (2012) (cit. on pp. 14, 15, 29, 66, 70).

[Bow13] R. Bowler, U. Warring, J. W. Britton, B. C. Sawyer, and J. Amini. *Arbitrary waveform generator for quantum information processing with trapped ions*. Rev. Sci. Instrum. **84**, 033108 (2013) (cit. on p. 70).

[Bri16] J. W. Britton, J. G. Bohnet, B. C. Sawyer, H. Uys, M. J. Biercuk, and J. J. Bollinger. *Vibration-induced field fluctuations in a superconducting magnet*. Phys. Rev. A **93**, 062511 (2016) (cit. on p. 80).

[Bro15] M. Brownnutt, M. Kumph, P. Rabl, and R. Blatt. *Ion-trap measurements of electric-field noise near surfaces*. Rev. Mod. Phys. **87**, 1419–1482 (2015) (cit. on pp. 14, 43, 94).

[Bru17] D. Bruß and G. Leuchs. *Lectures on quantum information* (2017) (cit. on p. 38).

[Bud07] D. Budker and M. Romalis. *Optical magnetometry*. Nat. Phys. **3**, 227–234 (2007) (cit. on p. 18).

[Bud08] D. Budker, D. F. Kimball, and D. P. DeMille. *Atomic physics : an exploration through problems and solutions*. Second edition. Oxford: Oxford University Press, 2008, 98–100 (cit. on pp. 22, 23, 91).

[Cai15] X.-D. Cai, D. Wu, Z.-E. Su, M.-C. Chen, X.-L. Wang, L. Li, N.-L. Liu, C.-Y. Lu, and J.-W. Pan. *Entanglement-Based Machine Learning on a Quantum Computer*. Phys. Rev. Lett. **114**, 110504 (2015) (cit. on p. 11).

[Cam96] P. Campbell. *Permanent magnet materials and their application*. Cambridge University Press, 1996 (cit. on p. 95).

[Che10] X. Chen, A. Ruschhaupt, S. Schmidt, A. del Campo, D. Guéry-Odelin, and J. G. Muga. *Fast Optimal Frictionless Atom Cooling in Harmonic Traps: Shortcut to Adiabaticity*. Phys. Rev. Lett. **104**, 063002 (2010) (cit. on p. 66).

[Che11] X. Chen, E. Torrontegui, D. Stefanatos, J.-S. Li, and J. G. Muga. *Optimal trajectories for efficient atomic transport without final excitation*. Phys. Rev. A **84**, 043415 (2011) (cit. on p. 70).

[Che17] H. Che, K. Deng, Z. T. Xu, W. H. Yuan, J. Zhang, and Z. H. Lu. *Efficient Raman sideband cooling of trapped ions to their motional ground state*. Phys. Rev. A **96**, 013417 (2017) (cit. on p. 35).

[Cho10] C. W. Chou, D. B. Hume, J. C. J. Koelemeij, D. J. Wineland, and T. Rosenband. *Frequency Comparison of Two High-Accuracy* Al^+ *Optical Clocks*. Phys. Rev. Lett. **104**, 070802 (2010) (cit. on p. 94).

[Chw09] M. Chwalla, J. Benhelm, K. Kim, G. Kirchmair, T. Monz, M. Riebe, P. Schindler, A. S. Villar, W. Hänsel, C. F. Roos, R. Blatt, M. Abgrall, G. Santarelli, G. D. Rovera, and P. Laurent. *Absolute Frequency Measurement of the* $^{40}\mathrm{Ca}^+$ $4s\ {}^2S_{1/2} - 3d\ {}^2D_{5/2}$ *Clock Transition*. Phys. Rev. Lett. **102**, 023002 (2009) (cit. on p. 91).

[Cir94] J. I. Cirac, L. J. Garay, R. Blatt, A. S. Parkins, and P. Zoller. *Laser cooling of trapped ions: The influence of micromotion*. Phys. Rev. A **49**, 421–432 (1994) (cit. on pp. 25, 34).

[Cir95] J. I. Cirac and P. Zoller. *Quantum Computations with Cold Trapped Ions*. Phys. Rev. Lett. **74**, 4091–4094 (1995) (cit. on p. 11).

[Dan10] H. B. Dang, A. C. Maloof, and M. V. Romalis. *Ultrahigh sensitivity magnetic field and magnetization measurements with an atomic magnetometer*. Appl. Phys. Lett. **97**, 151110 (2010) (cit. on p. 17).

[Deb16] S. Debnath, N. M. Linke, C. Figgatt, K. A. Landsman, K. Wright, and C. Monroe. *Demonstration of a small programmable quantum computer with atomic qubits*. Nature **536**, 63–66 (2016) (cit. on p. 13).

[Deg17] C. L. Degen, F. Reinhard, and P. Cappellaro. *Quantum sensing*. Rev. Mod. Phys. **89**, 035002 (2017) (cit. on pp. 74, 81).

[Don05] E. A. Donley, T. P. Heavner, F. Levi, M. O. Tataw, and S. R. Jefferts. *Double-pass acousto-optic modulator system*. Rev. Sci. Instrum. **76**, 063112 (2005) (cit. on p. 46).

[Dru02] D. Drung. *High-performance DC SQUID read-out electronics*. Physica C: Superconductivity **368**, 134–140 (2002) (cit. on p. 17).

[Ebl10] J. F. Eble, S. Ulm, P. Zahariev, F. Schmidt-Kaler, and K. Singer. *Feedback-optimized operations with linear ion crystals*. J. Opt. Soc. Am. B **27**, A99–A104 (2010) (cit. on p. 61).

[Fey86] R. P. Feynman. *Quantum mechanical computers*. Foundations of Physics **16**, 507–531 (1986) (cit. on p. 10).

[Fon05] L. E. Fong, J. R. Holzer, K. K. McBride, E. A. Lima, F. Baudenbacher, and M. Radparvar. *High-resolution room-temperature sample scanning superconducting quantum interference device microscope configurable for geological and biomagnetic applications*. Rev. Sci. Instrum. **76**, 053703 (2005) (cit. on p. 17).

[Fre80] R. Freeman, S. P. Kempsell, and M. H. Levitt. *Radiofrequency pulse sequences which compensate their own imperfections*. J. Magn. Reson. **38**, 453–479 (1980) (cit. on p. 91).

[Für14] H. Fürst, M. Goerz, U. Poschinger, M. Murphy, S. Montangero, T. Calarco, F. Schmidt-Kaler, K. Singer, and C. Koch. *Controlling the transport of an ion: Classical and quantum mechanical solutions*. New J. Phys. **16**, 075007 (2014) (cit. on p. 70).

[Gab88] G. Gabrielse and J. Tan. *Self-shielding superconducting solenoid systems*. J. Appl. Phys. **63**, 5143–5148 (1988) (cit. on p. 80).

[Gae16] J. P. Gaebler, T. R. Tan, Y. Lin, Y. Wan, R. Bowler, A. C. Keith, S. Glancy, K. Coakley, E. Knill, D. Leibfried, and D. J. Wineland. *High-Fidelity Universal Gate Set for* $^9\mathrm{Be}^+$ *Ion Qubits*. Phys. Rev. Lett. **117**, 060505 (2016) (cit. on p. 95).

[Gra09] C. Granata, A. Vettoliere, C. Nappi, M. Lisitskiy, and M. Russo. *Long baseline planar superconducting gradiometer for biomagnetic imaging*. Appl. Phys. Lett. **95**, 042502 (2009) (cit. on p. 18).

[Gri10] W. C. Griffith, S. Knappe, and J. Kitching. *Femtotesla atomic magnetometry in a microfabricated vapor cell*. Opt. Express **18**, 27167–27172 (2010) (cit. on p. 17).

[Gri13] M. S. Grinolds, S. Hong, P. Maletinsky, L. Luan, M. D. Lukin, R. L. Walsworth, and A. Yacoby. *Nanoscale magnetic imaging of a single electron spin under ambient conditions*. Nat. Phys. **9**, 215–219 (2013) (cit. on pp. 17, 18).

[Gro97] L. K. Grover. *Quantum Mechanics Helps in Searching for a Needle in a Haystack*. Phys. Rev. Lett. **79**, 325–328 (1997) (cit. on p. 11).

[Gul01] S. Gulde, D. Rotter, P. Barton, F. Schmidt-Kaler, R. Blatt, and W. Hogervorst. *Simple and efficient photo-ionization loading of ions for precision ion-trapping experiments*. Appl. Phys. B **73**, 861–863 (2001) (cit. on p. 34).

[Häf05] H. Häffner, F. Schmidt-Kaler, W. Hänsel, C. F. Roos, T. Körber, M. Chwalla, M. Riebe, J. Benhelm, U. D. Rapol, C. Becher, and R. Blatt. *Robust entanglement*. Appl. Phys. B **81**, 151–153 (2005) (cit. on p. 16).

[Han10] D. Hanneke, J. P. Home, J. D. Jost, J. M. Amini, D. Leibfried, and D. J. Wineland. *Realization of a programmable two-qubit quantum processor*. Nat. Phys. **6**, 2010 (2010) (cit. on p. 15).

[Har10] M. Harlander, M. Brownnutt, W. Hänsel, and R. Blatt. *Trapped-ion probing of light-induced charging effects on dielectrics*. New J. Phys. **12**, 093035 (2010) (cit. on p. 61).

[Har14] T. P. Harty, D. T. C. Allcock, C. J. Ballance, L. Guidoni, H. A. Janacek, N. M. Linke, D. N. Stacey, and D. M. Lucas. *High-Fidelity Preparation, Gates, Memory, and Readout of a Trapped-Ion Quantum Bit*. Phys. Rev. Lett. **113**, 220501 (2014) (cit. on p. 15).

[Här14] A. Härter, A. Krükow, A. Brunner, and J. Hecker Denschlag. *Long-term drifts of stray electric fields in a Paul trap*. Appl. Phys. B **114**, 275–281 (2014) (cit. on p. 61).

[Haz11] S. Haze, T. Ohno, K. Toyoda, and S. Urabe. *Measurement of the coherence time of the ground-state Zeeman states in 40Ca+*. Appl. Phys. B **105**, 761–765 (2011) (cit. on p. 15).

[Her12] N. Herschbach, K. Pyka, J. Keller, and T. E. Mehlstäubler. *Linear Paul trap design for an optical clock with Coulomb crystals*. Appl. Phys. B **107**, 891–906 (2012) (cit. on p. 94).

[Her15] D. A. Herrera-Martí, T. Gefen, D. Aharonov, N. Katz, and A. Retzker. *Quantum Error-Correction-Enhanced Magnetometer Overcoming the Limit Imposed by Relaxation*. Phys. Rev. Lett. **115**, 200501 (2015) (cit. on p. 96).

[Het15] M. Hettrich, T. Ruster, H. Kaufmann, C. F. Roos, C. T. Schmiegelow, F. Schmidt-Kaler, and U. G. Poschinger. *Measurement of Dipole Matrix Elements with a Single Trapped Ion*. Phys. Rev. Lett. **115**, 143003 (2015) (cit. on pp. 33, 34).

[Hom06] J. P. Home and A. M. Steane. *Electrode Configurations for Fast Separation of Trapped Ions*. Quantum Inf. and Comput. **6**, 289–325 (2006) (cit. on pp. 58, 65).

[Hub08] M. E. Huber, N. C. Koshnick, H. Bluhm, L. J. Archuleta, T. Azua, P. G. Björnsson, B. W. Gardner, S. T. Halloran, E. A. Lucero, and K. A. Moler. *Gradiometric micro-SQUID susceptometer for scanning measurements of mesoscopic samples*. Rev. Sci. Instrum. **79**, 053704 (2008) (cit. on p. 17).

[Hue97] S. F. Huelga, C. Macchiavello, T. Pellizzari, A. K. Ekert, M. B. Plenio, and J. I. Cirac. *Improvement of Frequency Standards with Quantum Entanglement*. Phys. Rev. Lett. **79**, 3865–3868 (1997) (cit. on p. 18).

[Ita07] W. M. Itano, J. C. Bergquist, A. Brusch, S. A. Diddams, T. M. Fortier, T. P. Heavner, L. Hollberg, D. B. Hume, S. R. Jefferts, L. Lorini, T. E. Parker, T. Rosenband, and J. E. Stalnaker. *Optical frequency standards based on mercury and aluminum ions*. Proc. SPIE **6673**, 667303 (2007) (cit. on p. 94).

[Iva10] P. A. Ivanov, U. G. Poschinger, K. Singer, and F. Schmidt-Kaler. *Quantum gate in the decoherence-free subspace of trapped-ion qubits*. Europhys. Lett. **92**, 30006 (2010) (cit. on p. 16).

[Jak64] R. C. Jaklevic, J. Lambe, A. H. Silver, and J. E. Mercereau. *Quantum Interference Effects in Josephson Tunneling*. Phys. Rev. Lett. **12**, 159–160 (1964) (cit. on p. 17).

[Jam01] D. F. V. James, P. G. Kwiat, W. J. Munro, and A. G. White. *Measurement of qubits*. Phys. Rev. A **64**, 052312 (2001) (cit. on pp. 72, 83).

[Jam98] D. James. *Quantum dynamics of cold trapped ions with application to quantum computation*. Appl. Phys. B **66**, 181–190 (1998) (cit. on pp. 25, 97).

[Jin93] J. Jin and D. A. Church. *Precision lifetimes for the* Ca^+ $4p\ {}^2P$ *levels: Experiment challenges theory at the 1% level*. Phys. Rev. Lett. **70**, 3213–3216 (1993) (cit. on p. 33).

[Jon09] J. A. Jones, S. D. Karlen, J. Fitzsimons, A. Ardavan, S. C. Benjamin, G. A. D. Briggs, and J. J. L. Morton. *Magnetic Field Sensing Beyond the Standard Quantum Limit Using 10-Spin NOON States*. Science **324**, 1166–1168 (2009) (cit. on p. 18).

[Kau14] H. Kaufmann, T. Ruster, C. T. Schmiegelow, F. Schmidt-Kaler, and U. G. Poschinger. *Dynamics and control of fast ion crystal splitting in segmented Paul traps*. New J. Phys. **16**, 073012 (2014) (cit. on pp. 14, 57, 58, 60, 61, 63, 69).

[Kau17a] H. Kaufmann. *A Scalable Quantum Processor*. dissertation. Universität Mainz, 2017 (cit. on pp. 14, 36, 43, 45, 51).

[Kau17b] H. Kaufmann, T. Ruster, C. T. Schmiegelow, M. A. Luda, V. Kaushal, J. Schulz, D. von Lindenfels, F. Schmidt-Kaler, and U. G. Poschinger. *Fast ion swapping for quantum-information processing*. Phys. Rev. A **95**, 052319 (2017) (cit. on pp. 14, 80, 94, 95).

[Kau17c] H. Kaufmann, T. Ruster, C. T. Schmiegelow, M. A. Luda, V. Kaushal, J. Schulz, D. von Lindenfels, F. Schmidt-Kaler, and U. G. Poschinger. *Scalable Creation of Long-Lived Multipartite Entanglement*. Phys. Rev. Lett. **119**, 150503 (2017) (cit. on pp. 15, 41, 54, 96).

[Kem06] K. Kemp and S. Wurm. *EUV lithography*. Comptes Rendus Physique **7**, 875–886 (2006) (cit. on p. 10).

[Kes12] A. Kesser. *Aufbau einer Mikro-Ionenfalle mit langer Qubit-Kohärenzzeit*. Diploma thesis. Universität Mainz, 2012 (cit. on pp. 44, 79).

[Kes14] E. M. Kessler, I. Lovchinsky, A. O. Sushkov, and M. D. Lukin. *Quantum Error Correction for Metrology*. Phys. Rev. Lett. **112**, 150802 (2014) (cit. on p. 96).

[Kie01] D. Kielpinski, V. Meyer, M. A. Rowe, C. A. Sackett, W. M. Itano, C. Monroe, and D. J. Wineland. *A Decoherence-Free Quantum Memory Using Trapped Ions*. Science **291**, 1013–1015 (2001) (cit. on p. 16).

[Kie02] D. Kielpinski, C. Monroe, and D. J. Wineland. *Architecture for a large-scale ion-trap quantum computer*. Nature **417**, 709 (2002) (cit. on p. 13).

[Kom03] I. Kominis, T. Kornack, J. Allred, and M. Romalis. *A subfemtotesla multichannel atomic magnetometer*. Nature **422**, 596–599 (2003) (cit. on p. 17).

[Kos11] M. Koschorreck, M. Napolitano, B. Dubost, and M. W. Mitchell. *High resolution magnetic vector-field imaging with cold atomic ensembles*. Appl. Phys. Lett. **98**, 074101 (2011) (cit. on p. 18).

[Kot11] S. Kotler, N. Akerman, Y. Glickman, A. Keselman, and R. Ozeri. *Single-ion quantum lock-in amplifier*. Nature **473**, 61–65 (2011) (cit. on pp. 18, 78).

[Kot14] S. Kotler, N. Akerman, N. Navon, Y. Glickman, and R. Ozeri. *Measurement of the magnetic interaction between two bound electrons of two separate ions*. Nature **510**. Letter, 376–380 (2014) (cit. on p. 18).

[Kre05] A. Kreuter, C. Becher, G. P. T. Lancaster, A. B. Mundt, C. Russo, H. Häffner, C. Roos, W. Hänsel, F. Schmidt-Kaler, R. Blatt, and M. S. Safronova. *Experimental and theoretical study of the* $3d^2D$*-level lifetimes of* $^{40}\mathrm{Ca}^+$. Phys. Rev. A **71**, 032504 (2005) (cit. on pp. 33, 91).

[Lad10] T. D. Ladd, F. Jelezko, R. Laflamme, Y. Nakamura, C. Monroe, and J. L. O'Brien. *Quantum computers*. Nature **464**, 45–53 (2010) (cit. on p. 11).

[Lam97] S. K. Lamoreaux. *Thermalization of trapped ions: quantum perturbation approach*. Phys. Rev. A **56**, 4970–4975 (1997) (cit. on p. 30).

[Lan05] C. Langer, R. Ozeri, J. D. Jost, J. Chiaverini, B. DeMarco, A. Ben-Kish, R. B. Blakestad, J. Britton, D. B. Hume, W. M. Itano, D. Leibfried, R. Reichle, T. Rosenband, T. Schaetz, P. O. Schmidt, and D. J. Wineland. *Long-Lived Qubit Memory Using Atomic Ions*. Phys. Rev. Lett. **95**, 060502 (2005) (cit. on pp. 16, 18).

[Lau11] H.-K. Lau and D. F. V. James. *Decoherence and dephasing errors caused by the dc Stark effect in rapid ion transport*. Phys. Rev. A **83**, 062330 (2011) (cit. on p. 29).

[Lee05] P. J. Lee, K.-A. Brickman, L. Deslauriers, P. C. Haljan, L.-M. Duan, and C. Monroe. *Phase control of trapped ion quantum gates*. J. Opt. B Quantum Semiclassical Opt. **7**, S371 (2005) (cit. on p. 14).

[Lei03a] D. Leibfried, R. Blatt, C. Monroe, and D. Wineland. *Quantum dynamics of single trapped ions*. Rev. Mod. Phys. **75**, 281–324 (2003) (cit. on p. 25).

[Lei03b] D. Leibfried, B. DeMarco, V. Meyer, D. Lucas, M. Barrett, J. Britton, W. M. Itano, B. Jelenković, C. Langer, T. Rosenband, et al. *Experimental demonstration of a robust, high-fidelity geometric two ion-qubit phase gate*. Nature **422**, 412–415 (2003) (cit. on pp. 14, 37, 39).

[Lei04] D. Leibfried, M. D. Barrett, T. Schaetz, J. Britton, J. Chiaverini, W. M. Itano, J. D. Jost, C. Langer, and D. J. Wineland. *Toward Heisenberg-Limited Spectroscopy with Multiparticle Entangled States*. Science **304**, 1476–1478 (2004) (cit. on p. 18).

[Mac12] T. Macha. *Frequenzstabilisierung eines Titan-Saphir-Lasers und Verbesserung von Qubits mit Ca$^+$-Ionen*. Diploma thesis. Universität Mainz, 2012 (cit. on p. 50).

[Mac14] K. Macieszczak, M. Fraas, and R. Demkowicz-Dobrzanski. *Bayesian quantum frequency estimation in presence of collective dephasing*. New J. Phys. **16**, 113002 (2014) (cit. on pp. 85, 87).

[Mal01] V. Malinovsky and J. Krause. *General theory of population transfer by adiabatic rapid passage with intense, chirped laser pulses*. Eur. Phys. J. D **14**, 147–155 (2001) (cit. on p. 39).

[Mar15] J. Markoff. *Smaller, Faster, Cheaper, Over: The Future of Computer Chips*. The New York Times, BU1 (2015) (cit. on p. 9).

[Mar16] E. A. Martinez, T. Monz, D. Nigg, P. Schindler, and R. Blatt. *Compiling quantum algorithms for architectures with multi-qubit gates*. New J. Phys. **18**, 063029 (2016) (cit. on p. 96).

[Mon09] T. Monz, K. Kim, A. S. Villar, P. Schindler, M. Chwalla, M. Riebe, C. F. Roos, H. Häffner, W. Hänsel, M. Hennrich, and R. Blatt. *Realization of Universal Ion-Trap Quantum Computation with Decoherence-Free Qubits*. Phys. Rev. Lett. **103**, 200503 (2009) (cit. on p. 16).

[Mon11a] T. Monz. *Quantum information processing beyond ten ion-qubits*. dissertation. Leopold-Franzens Universität Innsbruck, 2011 (cit. on pp. 52, 74).

[Mon11b] T. Monz, P. Schindler, J. T. Barreiro, M. Chwalla, D. Nigg, W. A. Coish, M. Harlander, W. Hänsel, M. Hennrich, and R. Blatt. *14-Qubit Entanglement: Creation and Coherence*. Phys. Rev. Lett. **106**, 130506 (2011) (cit. on pp. 13, 15, 18, 74).

[Mon16] T. Monz, D. Nigg, E. A. Martinez, M. F. Brandl, P. Schindler, R. Rines, S. X. Wang, I. L. Chuang, and R. Blatt. *Realization of a scalable Shor algorithm*. Science **351**, 1068–1070 (2016) (cit. on p. 13).

[Mon95] C. Monroe, D. M. Meekhof, B. E. King, S. R. Jefferts, W. M. Itano, D. J. Wineland, and P. Gould. *Resolved-Sideband Raman Cooling of a Bound Atom to the 3D Zero-Point Energy*. Phys. Rev. Lett. **75**, 4011–4014 (1995) (cit. on pp. 25, 35).

[Moo65] G. Moore. *Cramming more components onto integrated circuits*. Electronics **38** (1965) (cit. on p. 9).

[Moo75] G. Moore. *Progress in digital integrated electronics*. *Electron Devices Meeting, 1975 International*. **21**. IEEE. 1975, 11–13 (cit. on p. 9).

[Nag86] W. Nagourney, J. Sandberg, and H. Dehmelt. *Shelved optical electron amplifier: Observation of quantum jumps*. Phys. Rev. Lett. **56**, 2797–2799 (1986) (cit. on p. 39).

[Nic17] J. Nicodemus. *Automated Positioning Control for Trapped-Ion Quantum Registers*. Master's thesis. Universität Mainz, 2017 (cit. on pp. 76, 95, 96).

[Nig14] D. Nigg, M. Müller, E. A. Martinez, P. Schindler, M. Hennrich, T. Monz, M. A. Martin-Delgado, and R. Blatt. *Quantum computations on a topologically encoded qubit*. Science **345**, 302–305 (2014) (cit. on p. 96).

[Niz12] A. H. Nizamani and W. K. Hensinger. *Optimum electrode configurations for fast ion separation in microfabricated surface ion traps*. Appl. Phys. B **106**, 337–338 (2012) (cit. on p. 65).

[Not17] J. Nothhelfer. *Optikaufbau zum Treiben stimulierter Ramanübergänge*. Bachelor thesis. Universität Mainz, 2017 (cit. on p. 51).

[Nus12] N. M. Nusran, M. U. Momeen, and M. V. G. Dutt. *High-dynamic-range magnetometry with a single electronic spin in diamond*. Nat. Nanotechnol. **7**, 109 (2012) (cit. on pp. 85, 88).

[Oli90] F. A. M. de Oliveira, M. S. Kim, P. L. Knight, and V. Buek. *Properties of displaced number states*. Phys. Rev. A **41**, 2645–2652 (1990) (cit. on p. 30).

[Olm07] S. Olmschenk, K. C. Younge, D. L. Moehring, D. N. Matsukevich, P. Maunz, and C. Monroe. *Manipulation and detection of a trapped* Yb^+ *hyperfine qubit*. Phys. Rev. A **76**, 052314 (2007) (cit. on p. 15).

[Pal13] M. Palmero, E. Torrontegui, D. Guéry-Odelin, and J. G. Muga. *Fast transport of two ions in an anharmonic trap*. Phys. Rev. A **88**, 053423 (2013) (cit. on p. 70).

[Pau53] W. Paul and H. Steinwedel. *Notizen: Ein neues Massenspektrometer ohne Magnetfeld*. Zeitschrift für Naturforschung A **8**, 448–450 (1953) (cit. on p. 12).

[Pau90] W. Paul. *Electromagnetic traps for charged and neutral particles*. Rev. Mod. Phys. **62**, 531–540 (1990) (cit. on p. 25).

[Pel16] M. Pelliccione, A. Jenkins, P. Ovartchaiyapong, C. Reetz, E. Emmanouilidou, N. Ni, and A. C. B. Jayich. *Scanned probe imaging of nanoscale magnetism at cryogenic temperatures with a single-spin quantum sensor*. Nat. Nanotechnol. **11**, 700–705 (2016) (cit. on pp. 17, 18).

[Pos09] U. G. Poschinger, G. Huber, F. Ziesel, M. D. M. Hettrich, S. A. Schulz, K. Singer, G. Poulsen, M. Drewsen, R. J. Hendricks, and F. Schmidt-Kaler. *Coherent manipulation of a $^{40}Ca^{+}$ spin qubit in a micro ion trap*. J. Phys. B **42**, 154013 (2009) (cit. on pp. 33, 59).

[Pos10] U. G. Poschinger. *Quantum Optics Experiments in a Microstructured Ion Trap*. dissertation. Universität Mainz, 2010 (cit. on pp. 25, 34, 36, 52).

[Pou12] G. Poulsen, Y. Miroshnychenko, and M. Drewsen. *Efficient ground-state cooling of an ion in a large room-temperature linear Paul trap with a sub-Hertz heating rate*. Phys. Rev. A **86**, 051402 (2012) (cit. on p. 64).

[Řeh07] J. Řeháček, Z. Hradil, E. Knill, and A. I. Lvovsky. *Diluted maximum-likelihood algorithm for quantum tomography*. Phys. Rev. A **75**, 042108 (2007) (cit. on p. 84).

[Rei06] R. Reichle, D. Leibfried, E. Knill, J. Britton, R. B. Blakestad, J. D. Jost, C. Langer, R. Ozeri, S. Seidelin, and D. J. Wineland. *Experimental purification of two-atom entanglement*. Nature **443**, 838–841 (2006) (cit. on p. 15).

[Ron14] L. Rondin, J.-P. Tetienne, T. Hingant, J.-F. Roch, P. Maletinsky, and V. Jacques. *Magnetometry with nitrogen-vacancy defects in diamond*. Rep. Prog. Phys. **77**, 056503 (2014) (cit. on p. 18).

[Roo00] C. F. Roos. *Controlling the quantum state of trapped ions*. dissertation. Leopold-Franzens Universität Innsbruck, 2000 (cit. on p. 50).

[Roo04] C. F. Roos, G. P. T. Lancaster, M. Riebe, H. Häffner, W. Hänsel, S. Gulde, C. Becher, J. Eschner, F. Schmidt-Kaler, and R. Blatt. *Bell States of Atoms with Ultralong Lifetimes and Their Tomographic State Analysis*. Phys. Rev. Lett. **92**, 220402 (2004) (cit. on pp. 16, 18).

[Roo06] C. F. Roos, M. Chwalla, K. Kim, M. Riebe, and R. Blatt. *Designer atoms for quantum metrology*. Nature **443**, 316–319 (2006) (cit. on p. 18).

[Row02] M. A. Rowe, A. Ben-Kish, B. DeMarco, D. Leibfried, V. Meyer, J. Beall, J. Britton, J. Hughes, W. M. Itano, B. Jelenkovic, C. Langer, T. Rosenband, and D. J. Wineland. *Transport of quantum states and seperation of ions in a dual rf ion trap*. Quantum Inf. and Comput. **2**, 257 (2002) (cit. on p. 15).

[Rus16] T. Ruster, C. T. Schmiegelow, H. Kaufmann, C. Warschburger, F. Schmidt-Kaler, and U. G. Poschinger. *A long-lived Zeeman trapped-ion qubit*. Appl. Phys. B **122**, 254 (2016) (cit. on p. 45).

[Sch09] S. A. Schulz. *Scalable Microchip Ion Traps for Quantum Computation*. dissertation. Universität Ulm, 2009 (cit. on pp. 14, 43).

[Sch12] F. Schmidt-Kaler and R. Gerritsma. *Entangled states of trapped ions allow measuring the magnetic field gradient produced by a single atomic spin*. Europhys. Lett. **99**, 53001 (2012) (cit. on p. 94).

[Sch13] P. Schindler, D. Nigg, T. Monz, J. T. Barreiro, E. Martinez, S. X. Wang, S. Quint, M. F. Brandl, V. Nebendahl, C. F. Roos, M. Chwalla, M. Hennrich, and R. Blatt. *A quantum information processor with trapped ions*. New J. Phys. **15**, 123012 (2013) (cit. on pp. 13, 15, 37).

[Sch15] C. Schwemmer, L. Knips, D. Richart, H. Weinfurter, T. Moroder, M. Kleinmann, and O. Gühne. *Systematic Errors in Current Quantum State Tomography Tools*. Phys. Rev. Lett. **114**, 080403 (2015) (cit. on pp. 73, 84).

[Sch16a] C. T. Schmiegelow, H. Kaufmann, T. Ruster, J. Schulz, V. Kaushal, M. Hettrich, F. Schmidt-Kaler, and U. G. Poschinger. *Phase-Stable Free-Space Optical Lattices for Trapped Ions*. Phys. Rev. Lett. **116**, 033002 (2016) (cit. on p. 80).

[Sch16b] C. T. Schmiegelow, J. Schulz, H. Kaufmann, T. Ruster, U. G. Poschinger, and F. Schmidt-Kaler. *Transfer of optical orbital angular momentum to a bound electron*. Nat. Commun. **7**, 12998 (2016) (cit. on p. 47).

[Sea10] A. C. Seabaugh and Q. Zhang. *Low-Voltage Tunnel Transistors for Beyond CMOS Logic*. Proceedings of the IEEE **98**, 2095–2110 (2010) (cit. on p. 10).

[She17] D. Sheng, A. R. Perry, S. P. Krzyzewski, S. Geller, J. Kitching, and S. Knappe. *A microfabricated optically-pumped magnetic gradiometer*. Appl. Phys. Lett. **110**, 031106 (2017) (cit. on p. 18).

[Sho97] P. W. Shor. *Polynomial-Time Algorithms for Prime Factorization and Discrete Logarithms on a Quantum Computer*. SIAM Journal on Computing **26**, 1484–1509 (1997) (cit. on p. 11).

[Sim16] D. Simin, V. A. Soltamov, A. V. Poshakinskiy, A. N. Anisimov, R. A. Babunts, D. O. Tolmachev, E. N. Mokhov, M. Trupke, S. A. Tarasenko, A. Sperlich, P. G. Baranov, V. Dyakonov, and G. V. Astakhov. *All-Optical dc Nanotesla Magnetometry Using Silicon Vacancy Fine Structure in Isotopically Purified Silicon Carbide*. Phys. Rev. X **6**, 031014 (2016) (cit. on p. 17).

[Sin10] K. Singer, U. Poschinger, M. Murphy, P. Ivanov, F. Ziesel, T. Calarco, and F. Schmidt-Kaler. *Colloquium : Trapped ions as quantum bits: Essential numerical tools*. Rev. Mod. Phys. **82**, 2609–2632 (2010) (cit. on pp. 58, 59).

[Tak09] K. Takasumi, P. Dent, J. Liu, M. Marinescu, and M. Walmer. *New grade of temperature compensated samarium cobalt permanent magnets and design considerations*. *Vacuum Electronics Conference, 2009. IVEC'09. IEEE International*. IEEE. 2009, 565–566 (cit. on p. 95).

[Tay08] J. M. Taylor, P. Cappellaro, L. Childress, L. Jiang, D. Budker, P. R. Hemmer, A. Yacoby, R. Walsworth, and M. D. Lukin. *High-sensitivity diamond magnetometer with nanoscale resolution*. Nat. Phys. **4**, 810–816 (2008) (cit. on pp. 16, 89).

[Ter15] B. M. Terhal. *Quantum error correction for quantum memories*. Rev. Mod. Phys. **87**, 307–346 (2015) (cit. on pp. 11, 96).

[Tho96] L. Thomas, F. Lionti, R. Ballou, D. Gatteschi, R. Sessoli, and B. Barbara. *Macroscopic quantum tunnelling of magnetization in a single crystal of nanomagnets*. Nature **383**, 145–147 (1996) (cit. on p. 94).

[Tim11] N. Timoney, I. Baumgart, M. Johanning, M. Varon, M. B. Plenio, A. Retzker, and C. Wunderlich. *Quantum gates and memory using microwave-dressed states*. Nature **476**, 185 (2011) (cit. on p. 15).

[Tom03] G. Tommaseo, T. Pfeil, G. Revalde, G. Werth, P. Indelicato, and J. P. Desclaux. *The g_J-factor in the ground state of Ca^+*. Eur. Phys. J. D **25**, 113–121 (2003) (cit. on p. 91).

[Und16] T. Unden, P. Balasubramanian, D. Louzon, Y. Vinkler, M. B. Plenio, M. Markham, D. Twitchen, A. Stacey, I. Lovchinsky, A. O. Sushkov, M. D. Lukin, A. Retzker, B. Naydenov, L. P. McGuinness, and F. Jelezko. *Quantum Metrology Enhanced by Repetitive Quantum Error Correction*. Phys. Rev. Lett. **116**, 230502 (2016) (cit. on p. 18).

[Vas13] D. Vasyukov, Y. Anahory, L. Embon, D. Halbertal, J. Cuppens, L. Neeman, A. Finkler, Y. Segev, Y. Myasoedov, M. L. Rappaport, et al. *A scanning superconducting quantum interference device with single electron spin sensitivity*. Nat. Nanotechnol. **8**, 639–644 (2013) (cit. on p. 17).

[Ven07] M. Vengalattore, J. M. Higbie, S. R. Leslie, J. Guzman, L. E. Sadler, and D. M. Stamper-Kurn. *High-Resolution Magnetometry with a Spinor Bose-Einstein Condensate*. Phys. Rev. Lett. **98**, 200801 (2007) (cit. on p. 17).

[Wag10] C. Wagner and N. Harned. *EUV lithography: Lithography gets extreme*. Nat. Photonics **4**, 24–26 (2010) (cit. on p. 10).

[Wal11] A. Walther, U. Poschinger, F. Ziesel, M. Hettrich, A. Wiens, J. Welzel, and F. Schmidt-Kaler. *Single ion as a shot-noise-limited magnetic-field-gradient probe*. Phys. Rev. A **83**, 062329 (2011) (cit. on p. 54).

[Wal12a] G. Waldherr, J. Beck, P. Neumann, R. S. Said, M. Nitsche, M. L. Markham, D. J. Twitchen, J. Twamley, F. Jelezko, and J. Wrachtrup. *High-dynamic-range magnetometry with a single nuclear spin in diamond*. Nat. Nanotechnol. **7**, 105–108 (2012) (cit. on pp. 85, 88).

[Wal12b] A. Walther, F. Ziesel, T. Ruster, S. T. Dawkins, K. Ott, M. Hettrich, K. Singer, F. Schmidt-Kaler, and U. Poschinger. *Controlling Fast Transport of Cold Trapped Ions*. Phys. Rev. Lett. **109**, 080501 (2012) (cit. on pp. 14, 29, 95).

[Wan06] L. Wang. *Quantum Mechanical Effects on MOSFET Scaling*. dissertation. Georgia Institute of Technology, 2006 (cit. on p. 10).

[Wan11] S. X. Wang, G. H. Low, N. S. Lachenmyer, Y. Ge, P. F. Herskind, and I. L. Chuang. *Laser-induced charging of microfabricated ion traps*. J. Appl. Phys. **110**, 104901 (2011) (cit. on p. 61).

[War13] U. Warring, C. Ospelkaus, Y. Colombe, K. R. Brown, J. M. Amini, M. Carsjens, D. Leibfried, and D. J. Wineland. *Techniques for microwave near-field quantum control of trapped ions*. Phys. Rev. A **87**, 013437 (2013) (cit. on pp. 18, 93).

[Was10] W. Wasilewski, K. Jensen, H. Krauter, J. J. Renema, M. V. Balabas, and E. S. Polzik. *Quantum Noise Limited and Entanglement-Assisted Magnetometry*. Phys. Rev. Lett. **104**, 133601 (2010) (cit. on p. 90).

[Wie16] N. Wiebe and C. Granade. *Efficient Bayesian Phase Estimation*. Phys. Rev. Lett. **117**, 010503 (2016) (cit. on p. 87).

[Win79] D. J. Wineland and W. M. Itano. *Laser cooling of atoms*. Phys. Rev. A **20**, 1521–1540 (1979) (cit. on p. 27).

[Wol15] T. Wolf, P. Neumann, K. Nakamura, H. Sumiya, T. Ohshima, J. Isoya, and J. Wrachtrup. *Subpicotesla Diamond Magnetometry*. Phys. Rev. X **5**, 041001 (2015) (cit. on pp. 17, 90).

[Woo82] W. K. Wootters and W. H. Zurek. *A single quantum cannot be cloned*. Nature **299**, 802–803 (1982) (cit. on p. 11).

[Xia06] J. Xiang, W. Lu, Y. Hu, Y. Wu, H. Yan, and C. M. Lieber. *Ge/Si nanowire heterostructures as high-performance field-effect transistors*. Nature **441**, 489–493 (2006) (cit. on p. 10).

[Yao17] X.-W. Yao, H. Wang, Z. Liao, M.-C. Chen, J. Pan, J. Li, K. Zhang, X. Lin, Z. Wang, Z. Luo, W. Zheng, J. Li, M. Zhao, X. Peng, and D. Suter. *Quantum Image Processing and Its Application to Edge Detection: Theory and Experiment*. Phys. Rev. X **7**, 031041 (2017) (cit. on p. 11).

[Zie13] F. Ziesel, T. Ruster, A. Walther, H. Kaufmann, S. Dawkins, K. Singer, F. Schmidt-Kaler, and U. G. Poschinger. *Experimental creation and analysis of displaced number states*. J. Phys. B **46**, 104008 (2013) (cit. on p. 29).